
Temporal Frequency Image Correlation Techniques: Development and Characterization

Laurent Potvin-Trottier

Department of Physics

McGill University

Montréal, Québec

Canada

A Thesis submitted to the
Faculty of Graduate Studies and Research
in partial fulfillment of the requirements for the degree of
Master's of Science

© Laurent Potvin-Trottier, 2012

Contents

List of figures and tables	v
Abstract	vii
Résumé	ix
Statement Of Originality	xi
Acknowledgments	xiii
List of Abbreviations	xv
List of Symbols	xvii
1 Introduction	1
1.1 Cell migration	2
1.1.1 Protein dynamics	5
1.2 Fluorescence	6
1.2.1 Fluorescent proteins	8
1.3 Fluorescence microscopy	9
1.3.1 Noise	11
1.4 Measurement techniques	12
1.4.1 Fluorescence correlation spectroscopy	12
1.4.2 Image analysis techniques	13
1.5 Thesis outline	14
2 Theory	15
2.1 Fluorescence microscopy image example	15
2.2 Random signals	16
2.2.1 Correlation function and power spectrum	18
2.2.2 Cross-correlation and cross-power spectrum	19
2.2.3 Time average	19
2.3 Discrete-time signal processing	21
2.3.1 Discrete-time Fourier transform	21
2.3.2 Discrete Fourier transform	22
2.3.3 Estimating the correlation function	24
2.3.4 Spectral estimation and windowing	26
2.4 Spatio-temporal image correlation spectroscopy	29
2.4.1 Image correlation spectroscopy	31
2.4.2 Flow	32
2.4.3 Diffusion	33

2.4.4	Diffusion + flow	33
2.4.5	Cross-correlation	33
2.5	Multiple populations	34
3	Frequency space techniques	37
3.1	k-space image correlation spectroscopy	37
3.1.1	kICS bias	39
3.2	k- ν -space image correlation spectroscopy	40
3.3	ν -space image correlation spectroscopy	41
3.4	Immobile filtering	42
3.4.1	Linear filtering	43
3.5	Symmetry filtering	50
3.6	Cross-correlation	50
4	Characterization <i>in silico</i>	51
4.1	Materials and methods	51
4.1.1	Computer simulations	51
4.1.2	Data analysis	52
4.1.3	Tolerances	54
4.1.4	Boxplots	54
4.2	Butterworth filter	54
4.2.1	Motivation	54
4.2.2	Influence of the R ratio	55
4.2.3	Distortion of the velocity recovered	58
4.3	nICS	60
4.3.1	Analysis example	60
4.3.2	Windowing bias	60
4.4	knICS	63
4.4.1	Analysis example	63
4.5	Comparison of new techniques	63
4.5.1	Immobile density	65
4.5.2	Signal-to-noise	66
4.5.3	Diffusing population	66
4.6	Biased diffusion	69
4.6.1	Bias coefficient	69
4.6.2	Limits	73
4.6.3	Photobleaching	75
4.7	Summary	75
4.8	Towards velocity distribution fitting	82
5	Conclusion	85
	References	89
A	BIOHAZARDOUS MATERIALS CERTIFICATE	95

FIGURES AND TABLES

FIGURES

1.1 Schematic representation of cell migration	4
1.2 Examples of protein dynamics	7
1.3 Schematic of a wide-field fluorescence microscope	10
2.1 Example of fluorescence confocal microscopy image	16
2.2 Periodic convolution as linear plus aliasing	25
3.1 The effects of frequency filtering a simple flow on the correlation function	47
3.2 Filtering is similar for flowing and diffusing population	49
4.1 Comparison of velocities obtained with STICS without filtering, with Fourier and IIR filter	56
4.2 Effects of IIR filtering a flow in simulations as a function of R	57
4.3 Effects of IIR filtering a diffusion in simulations as a function of S	58
4.4 Effects of the IIR filter on the velocity recovered	59
4.5 Example of nICS analysis	61
4.6 nICS bias for short window lengths	62
4.7 Example of knICS analysis	64
4.8 Typical simulation	65
4.9 Accuracy and precision comparison of new techniques for different den- sities of immobile particles	67
4.10 Accuracy and precision comparison of new techniques for different amounts of noise	68
4.11 Accuracy and precision comparison of new techniques for different den- sities of immobile and diffusing particles	70
4.12 Accuracy and precision comparison of new techniques for measuring biased diffusion	72
4.13 Accuracy and precision comparison of new techniques for measuring biased diffusion part 2	73

4.14	Accuracy and precision comparison of new techniques for different densities of immobile particles for a biased diffusion.	76
4.15	Accuracy and precision comparison of new techniques for different amounts of noise for a biased diffusion.	77
4.16	Accuracy and precision comparison of new techniques for different densities of immobile and diffusing particles for a biased diffusion.	78
4.17	Accuracy and precision comparison of new techniques for measuring the diffusion coefficient of a biased diffusion.	79
4.18	Accuracy and precision comparison of new techniques for measuring biased diffusion	80
4.19	Accuracy and precision comparison of new techniques for measuring biased diffusion part 2	81
4.20	Velocity-density curve of a distribution of flow	83

TABLES

4.1	List of variable parameters in the simulator	52
4.2	Summary of strengths and limitations of IIR filtering, asymmetric analysis and nICS while analyzing biased diffusion.	82

Abstract

PROTEIN transport and trafficking are essential processes in living cells and therefore, important to understand. Spatio-temporal image correlation spectroscopy (STICS) allows quantification of the magnitude and direction of flow of fluorescently tagged proteins inside living cells. This is done through computation of the space-time correlation function of the intensity recorded in image series acquired via standard fluorescence microscopy. However, this powerful technique is often hindered by a high concentration of immobile particles in cells. New methods overcoming this problem will be developed in this thesis.

We start by creating a theoretical framework for spatio-temporal correlation functions. This allows easy extension to more complex type of kinetics, but more importantly, it constitutes the basis for our new techniques. Most of these techniques share a common characteristic: they rely on the time frequency space to separate populations of particles with different transport properties from each other. Effectively, slow dynamics are concentrated in the low frequencies, allowing extraction of faster dynamics for a minority population.

The first approach we propose is based on the theory of discrete-time signal processing. We use a highpass first-order Butterworth infinite-impulse response (IIR) filter on a pixel-per-pixel basis to select the dynamics we are interested in from a particular data set. Via a dimensionless analysis, we show a first approximation on how this filter will affect measurements of flowing and diffusing populations of particles. This filter can be tuned to select particular dynamics and, in contrast to a previously developed filter, does not depend on the length of the time series to be analyzed. An alternative analysis is to look at only the asymmetric part of the correlation function, since flows are the only asymmetric component.

The second approach is to look directly in temporal frequency space, or ν -space. Two new spaces of analysis are introduced, ν -space image correlation spectroscopy (nICS) and k - ν -space image correlation spectroscopy (knICS) for its spatial reciprocal. We derive the form of the correlation function for simple dynamics in knICS. In nICS, due to analytic difficulties we simply derive the form for a simple flow.

Finally, we use numerical simulations to show the validity of our approaches and

explore the strengths and limits of the newly developed techniques. We show that they are only moderately affected by immobile concentration, noise and other background populations. However, the ratio of flow to the diffusion coefficient in biased diffusion is the major constraint. Two new parameters which were previously not accessible with image correlation analysis are extracted from simulations, the diffusion coefficient of a biased diffusion and flow density.

This thesis provides new image correlation tools, which complement existing ones, that promise to shed light on the complicated inner workings of the cell.

Résumé

LE transport et l'adressage de protéines sont des procédés essentiels pour la cellule; leur compréhension est donc primordiale. La spectroscopie de corrélation spatio-temporelle d'images (*spatio-temporal image correlation spectroscopy*, STICS) permet la quantification de l'amplitude et de la direction du débit de protéines fluorescentes à l'intérieur de cellules vivantes. Ceci est possible à l'aide du calcul de la fonction de corrélation spatio-temporelle d'une série d'images acquises à l'aide d'un microscope à fluorescence standard. Par contre, cette technique est souvent limitée par de hautes concentrations de particules immobiles. De nouvelles méthodes pour surmonter ce problème seront développées dans ce mémoire.

Nous commencerons par développer un cadre théorique pour les fonctions de corrélation spatio-temporelle. Ceci nous permet de généraliser facilement les méthodes pour prendre en compte des dynamiques plus complexes, mais, surtout, ceci constitue la base pour nos nouvelles techniques. La plupart de ces méthodes partagent une caractéristiques communes: elles utilisent les fréquences temporelles afin de séparer les populations possédant des propriétés de transport différentes. En effet, les dynamiques lentes sont situées dans la région des basses fréquences, permettant ainsi l'extraction de dynamiques rapides de populations minoritaires.

La première approche que nous proposons se base sur la théorie du traitement de signal à temps discret. Nous utilisons un filtre passe-haut de type Butterworth de premier ordre (réponse à une impulsion infinie, *infinite-impulse response*, IIR) appliqué sur chaque pixel afin de sélectionner les dynamiques recherchées dans nos données. À l'aide d'une analyse adimensionnelle, nous montrons une première approximation de l'effet de ce filtre sur des populations de flux et de diffusion. Une analyse alternative est d'isoler la partie asymétrique de la fonction de corrélation, puisque seulement les populations de flux s'y retrouvent.

La deuxième approche est d'inspecter directement l'espace des fréquences temporelles, ou l'espace ν . Deux nouveaux espaces d'analyse sont présentés, la spectroscopie de corrélation d'images dans l'espace ν (*ν -space image correlation spectroscopy*, nICS) et la spectroscopie de corrélation d'images dans l'espace k - ν (*k - ν -space image correlation spectroscopy*, knICS). Nous dérivons la forme de la fonction de corrélation

pour des dynamiques simples pour knICS mais, dues à des difficultés analytiques, nous présentons seulement la forme de la fonction d'un flux pour nICS.

Enfin, nous utilisons des simulations numériques afin de montrer la validité de nos approches en plus d'explorer les forces et les limites de chacune d'entre elles. Nous montrons qu'elles sont peu affectées par la concentration de particules immobiles, le bruit et les autres populations d'arrière-plan. Néanmoins, le ratio entre la vitesse et la diffusion pour une diffusion biaisée émerge comme une contrainte majeure. Deux nouveaux paramètres précédemment non accessibles aux techniques d'imagerie de corrélation sont extraits soit le coefficient de diffusion d'une diffusion biaisée ainsi que la densité de flux.

Ce mémoire fournit de nouveaux outils d'imagerie de corrélation, complétant ainsi les techniques pré-existantes, qui promettent de faire la lumière sur le fonctionnement complexe des cellules.

Statement Of Originality

THE author claims the following aspects of the thesis constitute original scholarship and an advancement of knowledge.

- Development of a general formalism for spatio-temporal correlation function of fluorescent labels. This allows easier consideration of more complicated dynamics and special shapes of the point spread function.
- Development and characterization of a tunable infinite impulse response (IIR) filter to isolate specific dynamics. This type of filter has not been previously used in this context. A dimensionless analysis was undertaken to understand the effects of filtering on measurement of flowing and diffusing populations.
- Development and characterization of an asymmetric analysis to isolate molecular transport from other symmetric dynamics, such as immobile and diffusing particles.
- Development and characterization of ν -space image correlation spectroscopy (nICS). This new technique allows extraction of flow density, velocity and magnitude even in the presence of a high concentration of immobile particles.
- Development of k - ν -space image correlation spectroscopy (knICS), which separates different populations in separate planes according to their dynamics. The author also derived the form of the correlation function for simple dynamics.
- Comparison of the IIR filter, the asymmetric analysis and nICS in numerical simulations. The author showed that the techniques were only moderately affected by immobile density, noise and other background populations. The major constraint was the ratio of the velocity to the diffusion coefficient in the case of biased diffusion. Fitting of two parameters, flow density and bias coefficient, that were previously not accessible to image correlation techniques is shown.

Acknowledgments

Many people helped me during my (short) passage at McGill whom I would like to thank here.

First, I would like to thank my supervisor and mentor, Dr. Paul Wiseman for his guidance and support through this thesis. He encouraged freedom in my research and allowed me to find my own path. He promoted an enjoyable lab environment which facilitated creativity. I enjoyed doing research with him and particularly to hear his craziest endless stories.

I would also like to thank Dr. Antoine G. Godin for continuous scientific advice, but also for the purposeless walks and for always making worst jokes than mines. I appreciated being your “official translator” during those years. Sincere thanks to Dr. Jody L. Swift for helping me becoming a “junior biologist”, for your genuine encouragements and for trying really hard to pronounce my name. I also appreciated meticulously prepared coffee breaks with Dominique Guillet and Dr. Benjamin Rapapaz. Thank you Haruka Yoshie for your hard work in the lab but foremost for being always so smiley even when making “disasters”.

There is also many group members which contributed into making a nice environment and “interesting” retreats: Dr. Asmahan Abu-Arish, Jean-François Desjardins, Nageswara Ghattamaneni, Angelical Gopal, Elvis Pandzic, Jeremy Schwartzentruber, Dr. Mikhail Sergeev, Timothy Toplak and Dr. Umakanta Tripathy.

I also wish to express my gratitude to people who have helped me on a project not included in this thesis. Thank you Dr. Rick Horwitz for always being so enthusiastic about research and for guidance and directions. I would especially like to thank Lingfeng Chen for her hard work in the paper with the demanding referee. Thanks Dr. Kristopher Kubow, who has been very patient with me while I was trying to do biology. I would also like to thank Dr. Alexia Bachir and Dr. Miguel Vicente-Manzanares. Thanks to all of you for being my “flashlight in the dark” in the world of biology.

Finally, I am sincerely grateful to my partner, Kathy Beaudette. Merci ma chérie de me supporter et de me comprendre beau temps, mauvais temps. Merci de faire tourner ma terre, je t'en suis infiniment reconnaissant. Je voudrais aussi remercier mes

parents qui m'ont toujours supporté et m'ont encouragé à suivre mon propre chemin. Merci.

I would also like to acknowledge fellowship support from the Fonds Québécois de la Recherche sur la Nature et les Technologies (FQRNT) and the National Science and Engineering Research Council of Canada (NSERC). I would also like to thank McGill University, the Groupe de recherche axée sur la structure des protéines (GRASP) and the Biophysical Society for travel awards.

List of Abbreviations

APD	avalanche photodiode
BA	beam area
CCD	charge-coupled device
CLSM	confocal laser scanning microscopy
DFT	discrete Fourier transform
DTFT	discrete-time Fourier transform
FFT	fast Fourier transform
ICS	image correlation spectroscopy
kICS	k-space image correlation spectroscopy
knICS	k-nu-space image correlation spectroscopy
LTI	linear time-invariant
MSD	mean-squared displacement
nICS	nu-space image correlation spectroscopy
PMT	photomultiplier tube
PSF	point-spread function
px	pixel
ROI	region of interest
SNR	signal-to-noise ratio
STICS	spatio-temporal image correlation spectroscopy
TICS	temporal image correlation spectroscopy

List of Symbols

$((\))_L$	modulo L operator
$\check{\phi}_I[m]$	circular correlation estimator of signal I
$\check{P}_I(\omega)$	power spectrum estimator obtained by windowing the correlation function estimate
Δt	time between two samples
$\hat{\phi}_I[m]$	linear correlation estimator of signal I
$\hat{P}_I(\omega)$	periodogram, power spectrum estimator of signal I
$\langle \rangle$	time averaging operator
$\mathcal{E}\{\}$	expectation value operator
\mathcal{F}	Fourier transform operator
\mathcal{F}^{-1}	inverse Fourier transform operator
$\mathcal{I}(\omega)$	discrete-time Fourier transform of $I[m]$
$\mathcal{I}[k]$	discrete Fourier transform of $I[m]$
$\mathcal{I}_L(\omega)$	discrete-time Fourier transform of the periodically extended (with period L) signal
\otimes	convolution operator
\otimes^L	circular/periodic convolution operator
ϕ_I	correlation function of random signal I
σ_I^2	variance of random variable I
$\mathbf{I}(t)$	a particular sequence of a random variable I_t
$P(A)$	probability that event A occurs
$\Theta(t, \tau)$	photophysics correlation function
$\tilde{\Theta}(\nu)$	Fourier transform of the photophysics function
\tilde{C}_{PP}	power spectrum of the PSF
$\tilde{I}(\nu)$	Fourier transform of a particular sequence of the random process I_t
$\vec{\xi}$	spatial lag vector
$\vec{r}_i(t)$	position of particle i at time t
B_0	brightness of the probe
$B_i(t)$	photophysics of particle i at time t
C_{ab}	cross-correlation of the PSF of two channels
$C_{PP}(\vec{r})$	autocorrelation of the PSF
C_{ww}	Fourier transform of the autocorrelation of a window, $w[m]$

f_k	fraction of molecules in population k
f_s	sampling frequency
$I(\vec{r}, t)$	image intensity as a function of space and time
$I(t)$	a particular value of a random variable I_t
$I[m]$	a discrete sampled sequence of I_t
$I_p(\vec{r})$	PSF of our imaging system
I_t	random process I depending on the variable t
L	number of points in the discrete Fourier transform
$L_{\vec{r}, t}$	total number of samples
m_I	mean of random variable I
N	number of particles
$P_I(i, t)$	probability density function of random process I_t
P_f	period in the discrete-time Fourier spectrum
P_I	power spectrum of random signal I
$R(\vec{\xi}, \tau)$	unnormalized correlation function
$r(\vec{\xi}, \tau)$	normalized correlation function
t	time index
T	length of a measured signal
U	normalization constant in the periodogram
$V(\omega)$	discrete-time Fourier transform of a windowed signal
$W(\omega)$	Fourier transform of the window function
$w[m]$	window function
w_r	e^{-2} radius of a gaussian PSF

Introduction

SCIENCE is based on making verifiable predictions about the universe. Building this knowledge is often limited by the measurements tools. Just as high-energy physicists are building bigger particle accelerators to verify their theories, biologists are in constant need of new methods to understand the organization of life. Biology has proven to be very difficult to understand, especially at the molecular level. “Nothing in Biology Makes Sense Except in the Light of Evolution” is the title of an essay by Theodosius Dobzhansky [1]. The title is self-explanatory. Life is the result of a billion years process. The only way to “explain” biology is through evolution. Furthermore, evolution is in general a stochastic process. Genetic mutations occur randomly and the best candidates are selected. Therefore, biology is inherently stochastic from the molecular level. Complex networks of proteins, cells and organisms were built on this randomness.

This thesis will explore and develop new techniques that exploit this inherent randomness in the sense that they measure noise or fluctuations. Optical microscopy enables us to study life at the cellular level, but it is limited in spatial resolution by the diffraction of light. Fluorescent labels and fluorescence microscopy enable us to observe where specific proteins are located. This is of limited use to understand dynamic networks of proteins. Correlation techniques have been developed to give us greater insight into biological processes. The techniques developed here will focus on quantitative measurements of protein transport. Protein transport and trafficking plays an important role in the organization of the cell, as proteins are transported

across cellular membranes like the plasma membrane, the endoplasmic reticulum and the nuclear envelope. Trafficking, on the other hand, occurs between membrane-bound organelles via vesicles. We will show a minimally invasive approach which allows measurement of protein transport, or more generally, protein flow, in living cells. Spatio-temporal image correlation spectroscopy (STICS) is, to the best of our knowledge, the only technique capable of creating vector maps of fluorescently-tagged protein transport inside a living cell that is not limited to cytoskeletal protein, as is fluorescence speckle microscopy [2]. In this thesis, we will develop a new filter that allows selection of particular dynamics, and develop variations of the technique that give us greater insight about protein dynamics. Those developments will then be characterized and tested in numerical simulations.

For the sake of brevity, this chapter was organized more as a primer than an exhaustive reference. The reader lacking knowledge in specific areas will be directed to more comprehensive references. We will start with a brief overview of a particular biological challenge, the molecular regulation of cell migration. We will then explore the basics of fluorescence to see how it can help us understand biology. Different optical techniques that allow the imaging of those probes will then be briefly described. Finally, we will provide a short overview of different measurement and analysis techniques.

1.1 *Cell migration*

Cell migration is a vital biological process in which cells undergo directed movements to specific locations (see [3–8] for reviews). It plays multiple important roles in biology. Cell migration orchestrates embryonic morphogenesis, where, for example, groups of cells migrate collectively to form the resulting three-layer embryo during gastrulation [9]. It is also a prominent component of immune surveillance, where leukocytes migrate to the site of infection. Migration also contributes to many pathological processes, including tumor formation and metastasis, mental retardation, osteoporosis

sis, vascular disease and chronic inflammatory diseases [9]. Consequently, there is a strong motivation to understand cell migration, but this biological process remains challenging. Cell migration is a complex phenomenon requiring the spatio-temporal regulation and integration of multiple processes inside the cell in a multistage manner.

It begins with the *polarization* of the cell, which normally occurs in response to an external signal or stimulus. This signal is propagated through multiple proteins inside the cell to create an asymmetric concentration of proteins. An important event is the local activation of Rac or Cdc42 (signaling proteins of the Rho family of GTPases [10]), which stimulates the polymerization of actin filaments. This polymerization will push the membrane forward in the direction of migration, to create a broad lamellipodium or spike-like filopodia, for Rac and Cdc42 respectively. This step is called the *protrusion*. This membrane extension then attaches to the extracellular matrix (ECM) through *adhesions*, which are large complexes composed of hundreds of different proteins. Integrins are transmembrane heterodimeric proteins that makes the link between the inside and the outside of the cell. Myosin contraction through actin filaments pulls on those adhesions to *move the cell body forward*. During this step, adhesions at the back of the cells disassemble and detach to allow translocation of the cell. Those steps are then repeated cyclically enabling the cell to migrate [11]. A schematic representation of cell migration is shown in figure 1.1.

Due to the intrinsic asymmetry of functions in this process, trafficking plays an important role in cell migration. Moreover, retrograde flows (or fluxes) of adhesion proteins have been observed [13–15]. Recently, we showed [16] that the interaction between integrins and its extracellular ligand played an important role in cell migration, possibly adding a player in the molecular clutch model [12] that describes protrusion. Quantification of retrograde flows played a great role in the description of the phenomenon. Cell migration is just one example across many particular domains in biology where measurements of molecular transport are important. New techniques allowing a better characterization of these flows will be introduced in chapter 3.

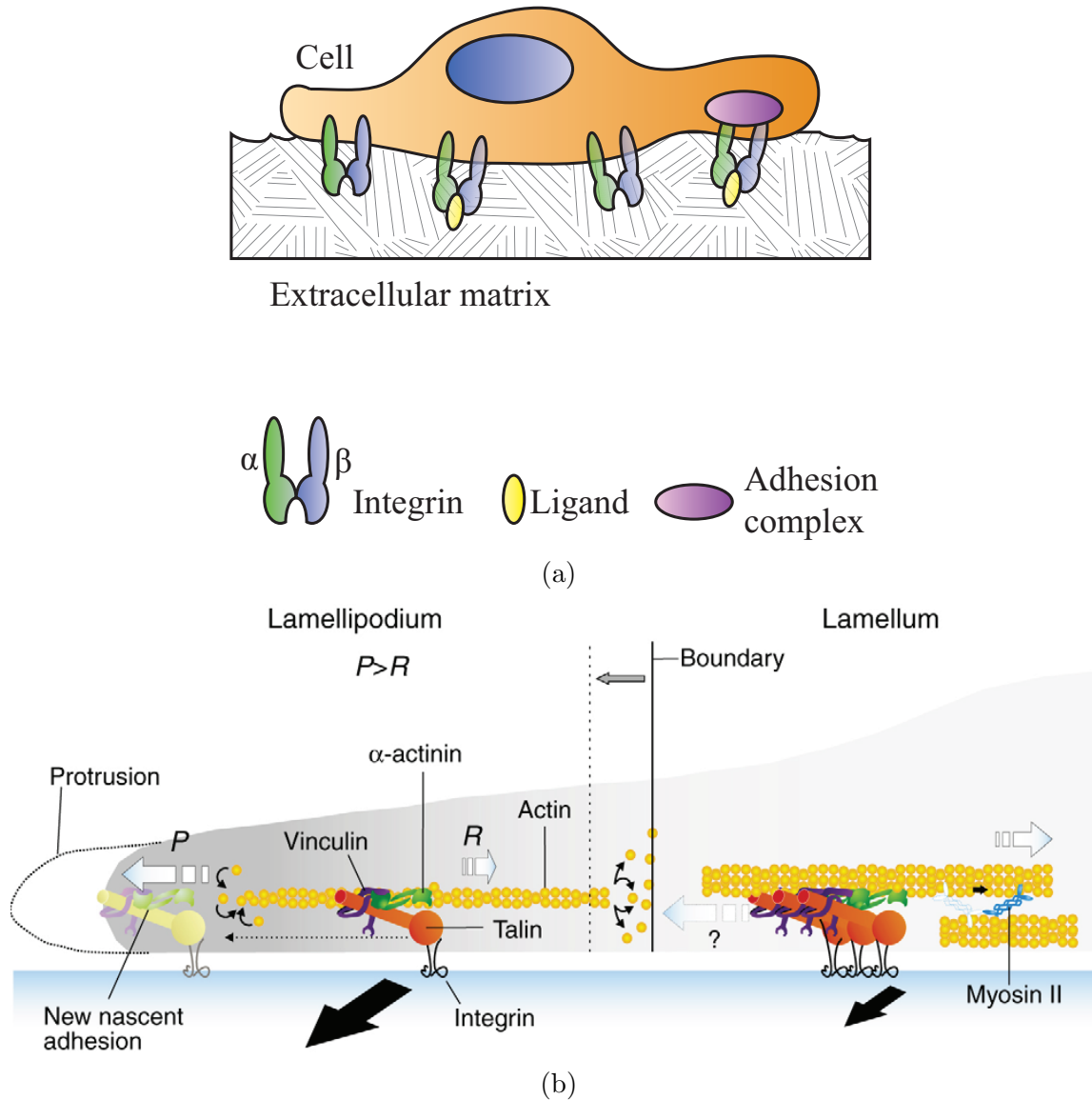


Figure 1.1: Schematic representation of cell migration. (a) A cell is attached to the extracellular matrix via integrins and adhesion complex. (b) Close-up of the edge of a migrating cell. Actin polymerization and anchoring to the extracellular matrix push the cell membrane forward to make a protrusion. Figure (b) was adapted from [12] with permission from *Journal of Cell Science*.

1.1.1 Protein dynamics

How can we characterize the motion of proteins? On their spatial scale (\sim nm), they can undergo many types of dynamics in liquids. The most basic one is *diffusion*, where the particle motion is purely random. Diffusion can be modeled either as phenomenological through Fick's laws or by considering the random walk of a single particle. The random walk model, where a particle has equal probability to move in either direction, was used to explain the Brownian motion of particles due to thermal fluctuations by Einstein [17]. Since the motion is random, the average displacement will vanish, but the *mean-squared displacement* (MSD) will be proportional to the time elapsed and a *diffusion coefficient*, D :

$$\langle \Delta r^2 \rangle = 2dDt \quad (1.1)$$

where Δr is the displacement and d the number of dimensions of the environment. The diffusion coefficient represents how fast the molecule moves and depends on its size and the viscosity of the liquid. For a spherical particle which is large relative to the solvent molecules, the Stoke-Einstein relationship yields:

$$D = \frac{RT}{6\pi\eta rN} \quad (1.2)$$

where R is the gas constant, T the temperature, η the solvent viscosity, r the particle radius and N Avogadro's number. Since proteins are generally small, they will diffuse very fast in 3D when they are present in the aqueous cytoplasm of the cell. Transmembrane proteins or proteins attached to the membrane will diffuse more slowly in 2D due to the viscosity of the lipid bilayer. A simple random walk is shown in figure 1.2a.

Proteins can also be transported with active transport or trafficking. A simple model for that would be a pure *flow*, where the movement is deterministic as shown in figure 1.2b. A more realistic model of molecular transport would be biased diffusion,

where proteins exhibit an average velocity but where individual displacements are random. This is a diffusion where the average displacement is non-zero, as shown in figure 1.2c.

Another trivial case for protein dynamics is immobilization. Proteins can be anchored, for example on the membrane or on the ECM, and diffuse too slowly on the timescale of analysis to be detected as moving. They will therefore appear *immobile*. Note that the definition of immobile depends on the timescale we are looking at and the spatial and temporal resolution of our instrument.

Finally, proteins can switch between dynamical states through biochemical reactions. For example, a protein can diffuse until it encounters a binding site on the membrane, where it attaches and stays immobile. It could afterwards be picked up by a motor to be transported to a particular location.

1.2 Fluorescence

The use of fluorescence techniques is now ubiquitous (see Lakowicz [18]), particularly in biology. Fluorescence is the process by which a molecule absorbs a photon and emits another, usually at a lower energy (higher wavelength). Upon absorption, the molecule is excited into a higher energy singlet electronic state. Non-radiative relaxation follows, usually among vibrational levels where energy is dissipated as heat. A photon is then emitted as the molecule relaxes to the ground singlet state. The difference between the absorption and emission wavelength is called the Stokes shift [19]. This apparently benign effect is precisely what makes fluorescence a very potent tool. Effectively, using filters to separate the excitation and emission wavelengths, it is possible to localize and obtain information about the fluorescent molecules.

Fluorescence is in general a much more complicated process. The different outcomes that can happen during fluorescence excited state lifetime are regrouped under the term *photophysics*. As the molecule is in the excited state, it can undergo a quantum mechanically “forbidden” transition to a triplet excited state, where relaxation

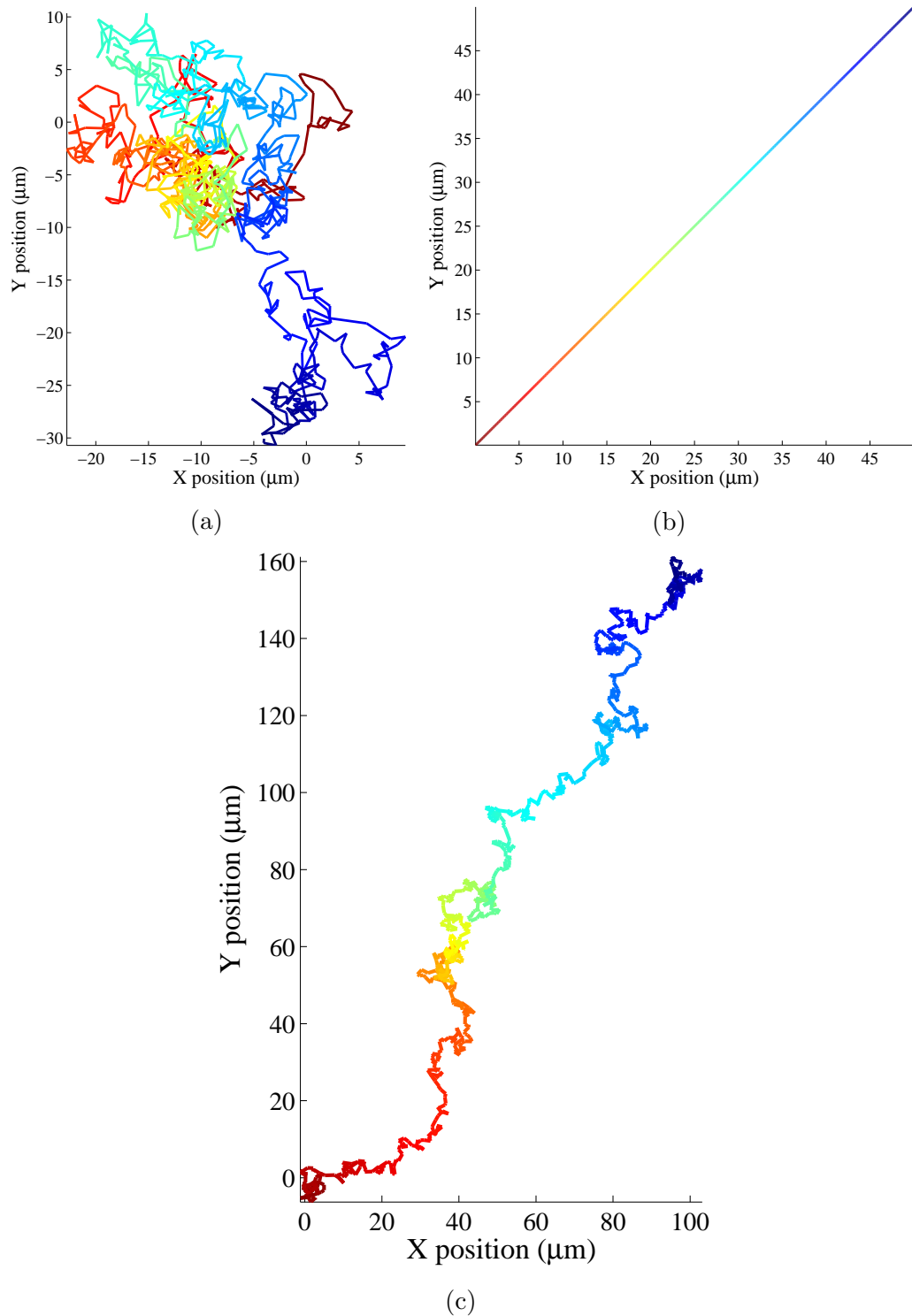


Figure 1.2: Simulated particle positions for 1000 steps in one second intervals for different dynamics. (a) Diffusion with $D = 0.5 \mu\text{m}^2/\text{s}$ (b) Pure flow with $v = 3 \mu\text{m}/\text{min}$ (c) Biased diffusion with $D = 0.5 \mu\text{m}^2/\text{s}$ and $v = 1.5 \mu\text{m}/\text{min}$. The colors represent the time evolution, going from dark red (0 s) to dark blue (1000 s).

occurs on a much slower time scale (phosphorescence). Since this process is much slower, the fluorophore will appear to “blink”. Another important effect is *photo-bleaching*, as excited molecules are more prone to redox chemical reactions such as oxidation. This renders the molecule non-fluorescent, and therefore the *photostability* of different fluorophores is an important characteristic for measurements. Finally, non-radiative decays to the ground state are possible through mechanisms such as energy transfer and quenching. The *quantum yield*, defined as the ratio of the number of photons emitted to the photons absorbed, is a property that represents the fluorophore brightness.

Multiple types of fluorescent probes that allow localization of proteins exist. The most common is immunofluorescent staining, where antibodies with attached fluorophores are used to bind specifically to the interested targets. This technique produces bright images due to the high number of fluorophores, but is often limited to fixed (non-live) samples and by imperfect binding specificity. Quantum dots are nanocrystals typically a few nanometers in diameter that are being increasingly used for single particle tracking. They are nearly an order of magnitude brighter [20] than conventional dyes and much more photostable [21]. However, they exhibit complex photophysics [22], they have to be conjugated to target specific proteins and this can induce clustering [23], affect the protein dynamics and complicate incorporation inside cells [24]. For all these reasons, the correlation techniques presented in this thesis have concentrated on the study of fluorescent proteins.

1.2.1 *Fluorescent proteins*

A key advance for experimental biology was the discovery of the green fluorescent protein (GFP), isolated from the jellyfish *Aequoria victoria* [25]. Dr. Roger Tsien shared the 2008 Nobel prize for his work on the enhanced version with better brightness and more rapid folding, enhanced-GFP (EGFP) [26]. At first, a fluorescent protein might not seem such a powerful tool. However, cloning of its DNA sequence allows creation

of chimeric (fusion) proteins which combine both a protein of interest and GFP. This gene can be inserted (transfected see [27] for methods overview) inside cells. This expression of fluorescent fusion proteins allows their localization inside living cells by microscopy. Multiple variants of GFP have been created with emission wavelengths from blue to red [28, 29]. However, fluorescent proteins are of rather large size ($\sim 3 \times 4 \text{ nm}^2$), and can therefore alter the functionality of the protein of interest. Moreover, overexpression of particular proteins (i.e. expression of fusion proteins along with the natural endogenous ones) can affect the cell behavior and has to be carefully considered. Promising novel technologies such as zinc finger nuclease [30, 31] allows insertion of DNA at specific locations in the genome, allowing the creation of chimeric proteins to replace the endogenous ones, and could overcome this limitation.

1.3 Fluorescence microscopy

In the previous section, we saw multiple methods of tagging proteins so that they would emit light at particular wavelengths. But how can we localize them? Multiple imaging modalities exist (see [32–34] for reviews), but most share the characteristics of light diffraction as established by Ernst Abbe. The resolution of light microscopy is limited by the diffraction of light through the microscope objective. The Rayleigh criterion gives a approximation to the distance at which two objects can be spatially resolved:

$$r = \frac{0.61\lambda_{em}}{\text{NA}} \quad (1.3)$$

where λ_{em} is wavelength of emission and NA the numerical aperture of the objective. This distance is generally around 200 nm for the blue end of the visible spectrum, much larger than the size of proteins. The concept of light diffraction means that imaging a single point (or something much smaller than 200 nm like a fluorescent protein) will result in a diffuse spot. This spot is characteristic of the imaging modality and is named the *point spread function* (PSF). Due to linearity, imaging an ensemble

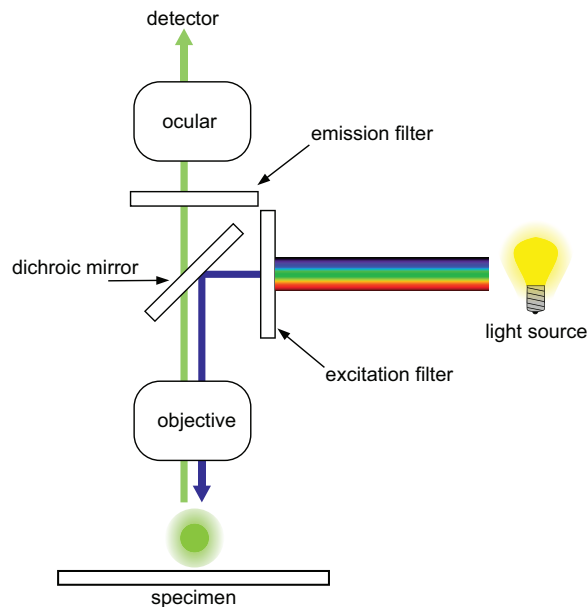


Figure 1.3: Schematic of a wide-field fluorescence microscope describing the general principles of fluorescence microscopy. Reproduced from the Wikipedia article on fluorescence microscope under the Creative Commons Attribution-Share Alike license 3.0.

of points or particles will result in a convolution of the particles position with the PSF, a blurring or spreading of the image.

The general principles of fluorescence microscopy are simply illustrated in the schematic of a wide-field microscope in figure 1.3. The sample is illuminated with an excitation light, which excites the fluorophores present. Emission light is then collected through the objective and separated from the excitation with a dichroic mirror and an emission filter. Wide-field fluorescence microscopy is one of the most simple and frequently used imaging modalities in biology.

One disadvantage of wide-field microscopy is the poor axial (z) resolution. A solution was patented by M. Minsky in 1961 [35]. The idea is to insert a small hole (pinhole) in a plane conjugate with the focal plane, thus rejecting out-of-focus light. In confocal laser scanning microscopy (CLSM), a laser beam is rastered across the sample using oscillating mirrors. The image is constructed point by point (pixel) by using photomultiplier tubes (PMT) or avalanche photodiode (APD) to amplify

the collected light. This technique allows thin sectioning (resolution $\sim 1 \mu\text{m}$) and therefore reconstruction of 3D images is possible. Two-photon microscopy is an alternative technique which uses a nonlinear effect to confine the excitation to a very small volume [36–38]. Two photons of half the excitation energy are used to excite the fluorophores. Since this nonlinear process is highly dependent on the light intensity, excitation is confined to a small focal volume ($\sim 1\mu\text{m}^3$). Finally, total internal reflection microscopy (TIRFm, [39, 40]) uses an evanescent wave to excite the specimen, which gives an optical sectioning of $\sim 200 \text{ nm}$ directly above the glass surface. Thus, it is a useful technique to study processes at the membrane. The excited light is typically collected using a charge-coupled device (CCD) camera.

1.3.1 Noise

All of these imaging methods create images, or time-series of images, which can be represented as a discrete intensity function, $I[x, y, t]$. The techniques developed in this thesis analyze this function to extract the dynamics of fluorescently labeled particles. However, this intensity is contaminated with noise intrinsic to the detectors. An unavoidable source is photon *shot noise*, which describes the uncertainty related with discrete photon counting. The probability distribution recording those independent events is the Poisson distribution, where the mean number of events is equal to the variance. Therefore, the signal-to-noise ratio (SNR), defined as the mean of the signal over the standard deviation of the noise, is:

$$\text{SNR} = n/\sqrt{n} = \sqrt{n} \quad (1.4)$$

where n is the number of photons. This sets the fundamental limit on the SNR, when other electronic noises are low (e.g. with photon counting devices). However, analog amplitude devices such as PMT and CCD generally introduce a similar type of noise which can be approximated as Gaussian distribution, where the standard deviation of the signal is equal to a multiple, the width factor (WF) of the mean. Thus,

$$\text{SNR} = \sqrt{I}/\text{WF} \quad (1.5)$$

Finally, there is a *background noise*, which encompasses noises fluctuating uniformly over the image. This can include detector dark currents, autofluorescence and non-specific signals. A description of how different sources of noise were included in simulations is found in section 4.1.1. For a more complete review of noise sources in imaging, the interested reader is referred to the following: [41, 42].

1.4 Measurement techniques

1.4.1 Fluorescence correlation spectroscopy

Fluorescence correlation spectroscopy (FCS, [43, 44]) was the first technique to exploit random fluctuations in the recorded intensity of a fluorescent label. In a nutshell, a laser beam is focused in the sample so that only a small volume of fluorophores is excited. As the fluorophores move in and out of the volume, fluctuations in the recorded intensity will occur. Giving sufficient sampling, the autocorrelation function of the signal intensity will give information about the number of fluorophores in the excited volume, their dynamics, chemical reactions occurring and conformational changes. If the concentration of molecules is low, the amplitude of fluctuations will be higher (relative to the mean). As the fluorophores move faster, the intensity will fluctuate more rapidly and the correlation function will decay more quickly. FCS is a powerful tool that enables measurements of a variety of biophysical parameters. However, the analysis requires calibration due to dependence on the size and shape of the excitation volume. It is also limited to single point measurements in the cell. Newer developments such as two-focus FCS [45], z-scan FCS [46] and scanning FCS [47] try to address these shortcomings.

1.4.2 Image analysis techniques

We present a variety of techniques in this section that can be used on widely available commercial imaging instruments. This idea is emphasized here, as the potential usefulness of measurement tools is greatly dependent on their accessibility to researchers. The most intuitive method to measure molecular motility is single particle tracking [48]. Building the MSD curve (mean-squared displacement as a function of time lag, see equation 1.1) allow quantification of diffusion, flow and diffusion with drift. However, it is limited to very low labeling densities due to resolution requirements of the tracking procedure.

Image correlation spectroscopy (ICS, [49, 50]) can be thought as the spatial variant of FCS. The spatial correlation function of an imaged region in a fluorescently labeled cell is computed, and information about the density and degree of aggregation can be extracted. Just as FCS exploits the temporal fluctuations at a fixed point in space, ICS uses the spatial fluctuations in an image acquired at a single time. Since its introduction, multiple variations and generalizations have been developed to analyze time series of images (see [51] for a review). Temporal image correlation spectroscopy (TICS) uses the temporal correlation of the intensity in pixels, averaged over a region. It is similar to FCS, but on a much slower timescale due to imaging frame sampling constraints. It has been used to measure the diffusion of cystic fibrosis transmembrane conductance regulators [52] and the velocity of cell adhesion proteins [53]. It can, however, be strongly affected by photophysics [54]. Spatio-temporal image correlation spectroscopy (STICS, [55]) is the generalization to the space-time domain. The complete correlation function is computed for multiple subregions in a series of images. It can create vector maps of protein transport inside living cells and extension of this technique will be the subject of this thesis. The general theory about this technique will be developed in chapter 2. This technique was used in multiple systems to measure flow of adhesion proteins [16, 55], movement of actin during cytokinesis [56], transport of vesicles in growing pollen tubes [57] and cell migration after injury

[58].

Another technique worth mentioning is fluorescence speckle microscopy (FSM,[2, 59]). To the best of our knowledge, this is the only other technique capable of mapping molecular transport of proteins inside living cells. However, it is limited to the study of speckle producing cytoskeleton and cytoskeleton-bound proteins since it requires high-resolution imaging of diffraction-limited regions containing 1-10 fluorophores [2]. Moreover, it necessitates suppression of photobleaching with illumination shutters and/or oxygen scavengers [60–62].

1.5 Thesis outline

STICS is a powerful tool to study protein transport and trafficking, but it is often hindered by high concentrations of immobile particles [55]. Dealing with this problem will be the central point of this thesis and will lead us to development of new analysis techniques. Chapter 2 will provide an overview of the theory of random signals and discrete-time signal processing. A generalized theory of STICS will then be developed. Based on these foundations, chapter 3 will provide the theoretical basis of four new analysis techniques. These developments will then be fully characterized *in silico* in chapter 4.

2

Theory

DU^E to the stochastic nature of biology at the molecular level, it can be useful to refer to fluorescence measurement as a random signal. By measuring particular properties of such fluctuations, different techniques can reveal a plethora of information about biological systems. This chapter will start with an example of real biophysical microscopy data. After, a brief review of the important properties of random variables will be provided. A basic knowledge of probability theory is assumed. This will be followed by an overview of discrete-time signal processing, since the measurements are commonly done digitally. Based on these foundations, we will provide a new approach to spatio-temporal correlation techniques. This chapter will provide the foundations for the new analysis techniques developed in chapter 3.

2.1 Fluorescence microscopy image example

It is important to understand why measurements will be treated as random variables. Figure 2.1 shows an example of a confocal fluorescence microscopy time series. The cells imaged are CHO-K1 cells transfected with a protein that marks focal adhesions, speckle-paxillin-GFP. This particular plasmid has a truncated promoter to keep a low expression level that aids in the visual tracking of adhesions. Paxillin is a protein commonly found in the cellular adhesion complex. An inverted color scale (darker pixels have higher intensities) was used to facilitate locating adhesions (dark ellipses). Small regions of interest (ROI) are chosen so that we can assume that protein dy-

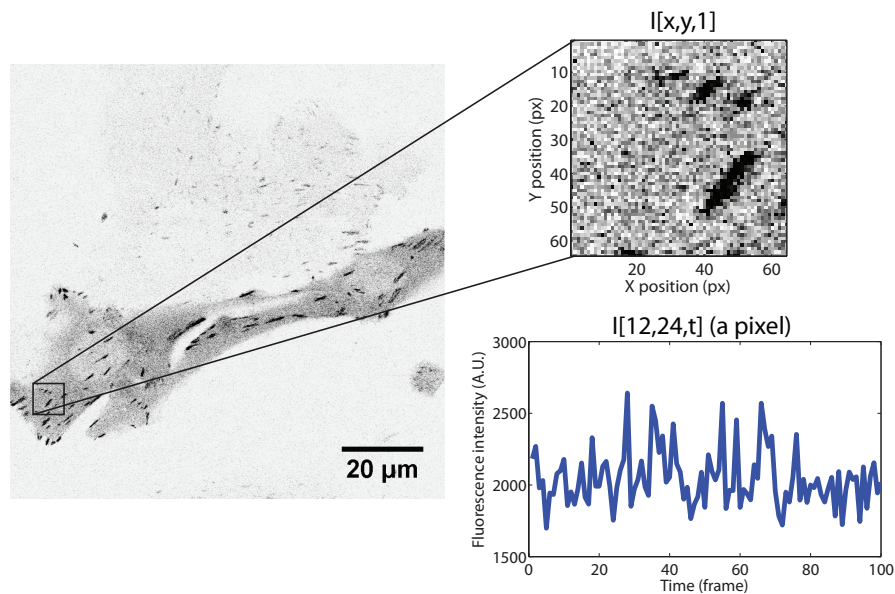


Figure 2.1: CHO-K1 cells expressing speckle-paxillin-GFP imaged with a CLSM. Multiple cells with different background intensities are visible on the first frame of the time series (left). A specific region of interest has been chosen (top right). The time intensity of a particular pixel shows no obvious trend (bottom right). An inverted intensity as been chosen to enhance contrast (darker pixels represent higher intensities).

namics are locally uniform. The dynamics of interest are not obvious by inspection of the time evolution of the image series, as noise, random particle distributions, diffusion and a dominant background intensity can overshadow other dynamics which may be present. This digitized image series, which can be modeled as measurements of random processes in the cell, represent the analysis starting point. The rest of the chapter will show what measurements can be performed and what information can be extracted by modeling the data using random variables.

2.2 Random signals

What is a random signal? One could think of a random signal as a value, or sequence of values, sampled from an underlying *random process*. Let I_t be our random process and $I(t)$ be a particular value of that process at time t . In this section, we won't need

to distinguish between the two, so we will use the simpler representation to lighten the notation. The classic example of a random variable is the coin toss. If we flip a coin a few times and measure the outcome, we will obtain a sequence of values, or vector, out of the random process. For example, using 1 for tail and 0 for head, we could obtain: $I(1) = 0$, $I(2) = 1$, $I(3) = 1$, $I(4) = 0$ and $I(5) = 1$. Written more concisely, our sampled sequence would be:

$$\mathbf{I}(t) = [0 \quad 1 \quad 1 \quad 0 \quad 1] \quad (2.1)$$

A random process may depend on other variables than time, like space for example. Those variables may be *continuous* or *discrete*. Some processes depend on more than one variable, such as spatial coordinates and time. For simplicity, the following discussion will assume processes producing continuous real values that depend on one variable, continuous time, but it can easily be extended to more variables.

Random processes are entirely characterized by their *probability distribution function*, $P_I(i, t)$, which describes the probability of obtaining a value around i at time t :

$$P(a \leq I(t) \leq b) = \int_a^b P_I(i, t) di \quad (2.2)$$

In practice, it can be difficult or not even desirable to obtain this function. Some other properties are useful to characterize a random process, such as the *average*, or *mean*:

$$m_I = \mathcal{E}\{I_t\} = \int i P_I(i, t) di \quad (2.3)$$

where $\mathcal{E}\{\}$ is the expectation operator. In general, the mean can depend on time. However, we will restrict our discussion to *stationary* processes, where measures presented in this section are constant in time. A random signal fluctuates around the mean (otherwise it would not be a random signal!). The amplitude of these fluctua-

tions can be quantified with the *variance*, σ_I^2 :

$$\sigma_I^2 = \mathcal{E}\{(I_t - m_I)^2\} = \mathcal{E}\{I_t^2\} - m_I^2 \quad (2.4)$$

where we used the linear properties of the expectation operator.

2.2.1 Correlation function and power spectrum

Suppose you measure your process at time t , then what will it be at later time? Because of the randomness, you cannot *know* the exact evolution, but you can still characterize it. A particularly useful description of the time evolution of a random process is its *correlation function*, ϕ_I :

$$\phi_I(\tau) = \mathcal{E}\{I_t I_{t+\tau}\} = \int \int i_t i_{t+\tau} P_{I_t I_{t+\tau}} di_t di_{t+\tau} \quad (2.5)$$

where $P_{I_t I_{t+\tau}}$ is the joint probability distribution for random variables I_t and $I_{t+\tau}$. For stationary processes, ϕ_I is only a function of τ . By straightforward manipulations:

$$\phi_I(0) = \sigma_I^2 + m_I^2 \quad (2.6)$$

$$\phi_I(\tau) = \phi_I(-\tau) \quad (2.7)$$

$$\phi_I(0) \geq |\phi_I(\tau)| \quad (2.8)$$

Furthermore, for processes that decorrelate over time, we have:

$$\lim_{\tau \rightarrow \infty} \phi_I(\tau) = m_I^2 \quad (2.9)$$

The Fourier transform of the correlation function is:

$$P_I(\nu) = \int \phi_I(\tau) e^{2\pi i \nu \tau} d\tau \quad (2.10)$$

where $P_I(\nu)$ is the *power spectrum*. This frequency domain function conveys information about the frequency content of a random signal. For example, a random signal with a constant power spectrum is commonly referred to as a *white-noise* process. Its correlation function would be a Dirac delta, as there is no correlation in time. It is interesting to see the correlation function and the power spectrum as two different *spaces* characterizing our random signals. They provide the same information, albeit presented in different domains.

2.2.2 Cross-correlation and cross-power spectrum

It is sometimes useful to see how two random signals, say I_a and I_b , are related. The previous measures are readily generalizable to two signals. The cross-correlation function and cross-power spectrum are respectively defined as:

$$\phi_{ab}(\tau) = \mathcal{E}\{I_a(t)I_b(t + \tau)\} \quad (2.11)$$

$$P_{ab}(\nu) = \int \phi_{ab}(\tau)e^{2\pi i\nu\tau} d\tau \quad (2.12)$$

where we dropped the I to simplify the notation. Properties of those functions are generally similar to the autocorrelation case, but it is important to note that the cross-correlation is *not* necessarily symmetric. The symmetry property of the cross-correlation can be written as:

$$\phi_{ab}(\tau) = \phi_{ba}(-\tau) \quad (2.13)$$

2.2.3 Time average

The previous definitions are useful mathematically. They provide different measures by *ensemble averaging*, or integrating over all possible values weighted by their probabilities. However, in practice, we will try to estimate these measures by *time averaging*. Under the condition known as *ergodicity*, the time and ensemble averages

are equal. An example might be useful to understand this concept. Suppose you measure a random process I_t for a long time. You could build an histogram of all the values obtained, and by normalizing it with the number of values you have measured, you would expect this histogram to converge to the probability density function of I_t . Such a process would then be ergodic. This property also explains why we do not need to distinguish the random variable I_t from a particular value of that variable $I(t)$, as the latter is itself a random variable.

We can therefore write:

$$\langle I_t \rangle = \lim_{T \rightarrow \infty} \frac{1}{T} \int_{-T/2}^{T/2} I(t) dt = \mathcal{E}\{I_t\} = m_I \quad (2.14)$$

where $\langle \rangle$ is the time average operator and T the length of the signal. We can rewrite the correlation function:

$$\phi_I(\tau) = \lim_{T \rightarrow \infty} \frac{1}{T} \langle I(t)I(t+\tau) \rangle = \lim_{T \rightarrow \infty} \frac{1}{T} \int_{-T/2}^{T/2} I(t)I(t+\tau) dt = \lim_{T \rightarrow \infty} \frac{1}{T} I(t) \otimes I(-t) \quad (2.15)$$

where \otimes is the convolution operator. Using the convolution theorem and Fourier transforming each side of (2.15), we obtain:

$$P_I(\nu) = \lim_{T \rightarrow \infty} \frac{1}{T} \tilde{I}(\nu) \tilde{I}(\nu)^* = \lim_{T \rightarrow \infty} \frac{1}{T} |\tilde{I}(\nu)|^2 \quad (2.16)$$

where $\tilde{I}(\nu)$ represents the Fourier transform¹ of $I(t)$ and $*$ the complex conjugate. Equation (2.16) provides us valuable insight about the measures that were described in this section. First, it tells us why the power spectrum represents the frequency content of our random signal. Second, it suggests to us at an efficient way of computing the correlation function and the power spectrum.

Generally, intensity fluctuations from live cell measurement can be considered er-

¹Although not all processes have a convergent Fourier transform in the strict sense (i.e. square summable), it is often possible to interpret them in terms of generalized functions [63].

godic and stationary. One notable exception is the fluorophore's photophysics (e.g. photobleaching), which can be neither ergodic nor stationary (i.e. the mean changes over time). However, as it is independent from the particle's dynamics, it can be treated separately. Moreover, methods for correcting for photobleaching will be discussed later in the thesis (see sections 3.2 and 4.1.2). Therefore, the discussion will be restricted to the study of stationary and ergodic random processes; ensemble averaging and time averaging will be used interchangeably. Before we see what those measures tell us about biological systems, we will briefly discuss the effects of *discrete sampling*.

2.3 Discrete-time signal processing

Many measurements are now done digitally; that is we sample a discrete number of points out of the continuous underlying process. Following convention, $I[m]$ will denote the discrete sampled $I(t)$. The brackets emphasize that we restrict $t = m\Delta t = m/f_s$, where m is any integer, Δt the time between two samples and f_s the sampling frequency.

The subject of discrete-time signal processing, or digital signal processing, is a field on its own. This section is by no means a comprehensive review of the field; important results will merely be cited and their impact on our analysis discussed. The interested reader is referred to a dedicated reference such as [64].

2.3.1 Discrete-time Fourier transform

How can we extract frequency information out of an infinite, discrete sequence $I[m]$? Many signals can be represented by an integral of the form:

$$I[m] = \frac{1}{2\pi} \int_{-\pi}^{\pi} \mathcal{I}(\omega) e^{i\omega m} d\omega \quad (2.17)$$

where

$$\mathcal{I}(\omega) = \sum_{m=-\infty}^{\infty} I[m]e^{i\omega m} \quad (2.18)$$

Functions represented by equations (2.17) and (2.18) are referred to as a discrete-time Fourier transform (DTFT) pair. Note that we have taken care of using a different notation to distinguish the Fourier transform of a continuous function and the DTFT of a sampled function. It is also interesting to see that this representation is just a clever use of the concept of Fourier series. Indeed, $I[m]$ can be seen as the Fourier series coefficients of the 2π periodic function $\mathcal{I}(\omega)$. This periodicity is inherent to DTFT and is of crucial importance. In this view, $I[m]$ are the Fourier coefficients separated by the natural frequency $1/P_f$, where P_f is the period in $\mathcal{I}(\nu)$. From our definition of section 2.3:

$$P_f = \frac{1}{\Delta t} = f_s \quad (2.19)$$

In other words, our spectrum $\mathcal{I}(\nu)$ is periodic with period f_s . A thorough development [e.g. 64, section 4.1-4.2] would show that $\mathcal{I}(\nu)$ is equivalent to the infinite sum of the continuous-time Fourier transform $\tilde{I}(\nu)$ shifted by nf_s , where n is an integer. This process is commonly known as *frequency aliasing*. Therefore, it is only possible to correctly identify frequency between $-f_s/2$ and $f_s/2$.

One could note that if the spectrum of the continuous signal is zero outside $-f_s/2$ and $f_s/2$ (a *bandlimited signal*), it is possible to obtain an exact representation of the Fourier transform (and therefore, of the signal) from the sampled sequence. This important result is known as the Nyquist-Shannon [65, 66] theorem.

2.3.2 Discrete Fourier transform

In practice, we are interested in the Fourier spectrum of finite-length sequences. This problem is addressed using the discrete Fourier transform (DFT). The development of particularly efficient algorithms for this task, known collectively as the *fast-Fourier transform* (FFT, [67, 68]), has made this approach ubiquitous. While there is no

room for a thorough development of DFT in this thesis, it is important to know how they are developed to understand their implications in signal analysis.

Having a T length signal, it is possible to extend that signal to infinity by periodic extension. Let's take a period of $L \geq T$, where we padded our signal with $L - T$ zeros. The following equations represent the analysis/synthesis equation for the DFT:

$$\mathcal{I}[k] = \sum_{m=0}^{L-1} I[m] W_L^{km} \quad (2.20)$$

$$I[m] = \frac{1}{L} \sum_{k=0}^{L-1} \mathcal{I}[k] W_L^{-km} \quad (2.21)$$

where $W_L^{km} = e^{-i(km)(2\pi/L)}$. It can be shown that $\mathcal{I}[k]$ samples the Fourier transform of the periodic extension of the signal, samples which are equally spaced by $2\pi/L$. That is:

$$\mathcal{I}[k] = \mathcal{I}_L(\omega)|_{\omega=(2\pi/L)k} = \mathcal{I}_L\left(\frac{2\pi}{L}k\right) \quad (2.22)$$

where $\mathcal{I}_L(\omega)$ is the DTFT of the periodically extended (with period L) signal. This periodicity is therefore inherent in the DFT and should always be kept in mind. It can sometimes be used as an advantage but sometimes it introduces complications. The next section will show an example of such effects.

Periodic convolution

The DFT shares many properties of the Fourier transform, with some important distinctions. One property for which it is important to understand the effect of discretization is the *circular/periodic* convolution. If $I_x[m]$ denotes a signal (zero-padded or not) of total length L and $\mathcal{I}_x[k]$ its DFT so that:

$$\mathcal{I}_3[k] = \mathcal{I}_1[k] \mathcal{I}_2[k] \quad (2.23)$$

then:

$$I_3[m] = \sum_{n=1}^L I_1[n] I_2[((n - m))_L] \quad (2.24)$$

$$I_3[m] = I_1[m] \otimes^L I_2[m] \quad (2.25)$$

where we defined the $((\))_L$ the modulo operator (i.e. add or subtract L until you are in the signal range) and \otimes^L the circular/periodic convolution operator. This important property means that multiplying two DFT does not convolve them *linearly*. Instead, it convolves the L periodic extension of the signals. One way to visualize the process is to imagine the sequences wrapped around the circumference of a cylinder (figure 2.2b). When shifting the signal to produce the convolution, it is rotated around the cylinder.

It can be shown [64, section 8.7.2] that the circular convolution is equal to an aliased version of the linear one (figure 2.2c). Intuitively, it is easy to understand why there is aliasing, which in this case is referred to as *time-domain aliasing*. Convolution linearly two T length sequences results in a $2T - 1$ signal. Multiplying two T points DFT will result in a T point signal. Therefore, taking the inverse DFT will lead to aliasing since there are not enough points to represent the data. Thus, one should note that choosing a $L \geq 2T$ points Fourier transform (padding our signal with T zeros) will produce a linear convolution.

2.3.3 Estimating the correlation function

Suppose you measure a finite length signal $I[m]$. Consider an estimate of the correlation function:

$$\hat{\phi}_I[m] = \frac{1}{T - |m|} \sum_{n=1}^{T-|m|} I[n] I[n + |m|] = \frac{1}{T - |m|} I[n] \otimes I[-n] \quad (2.26)$$

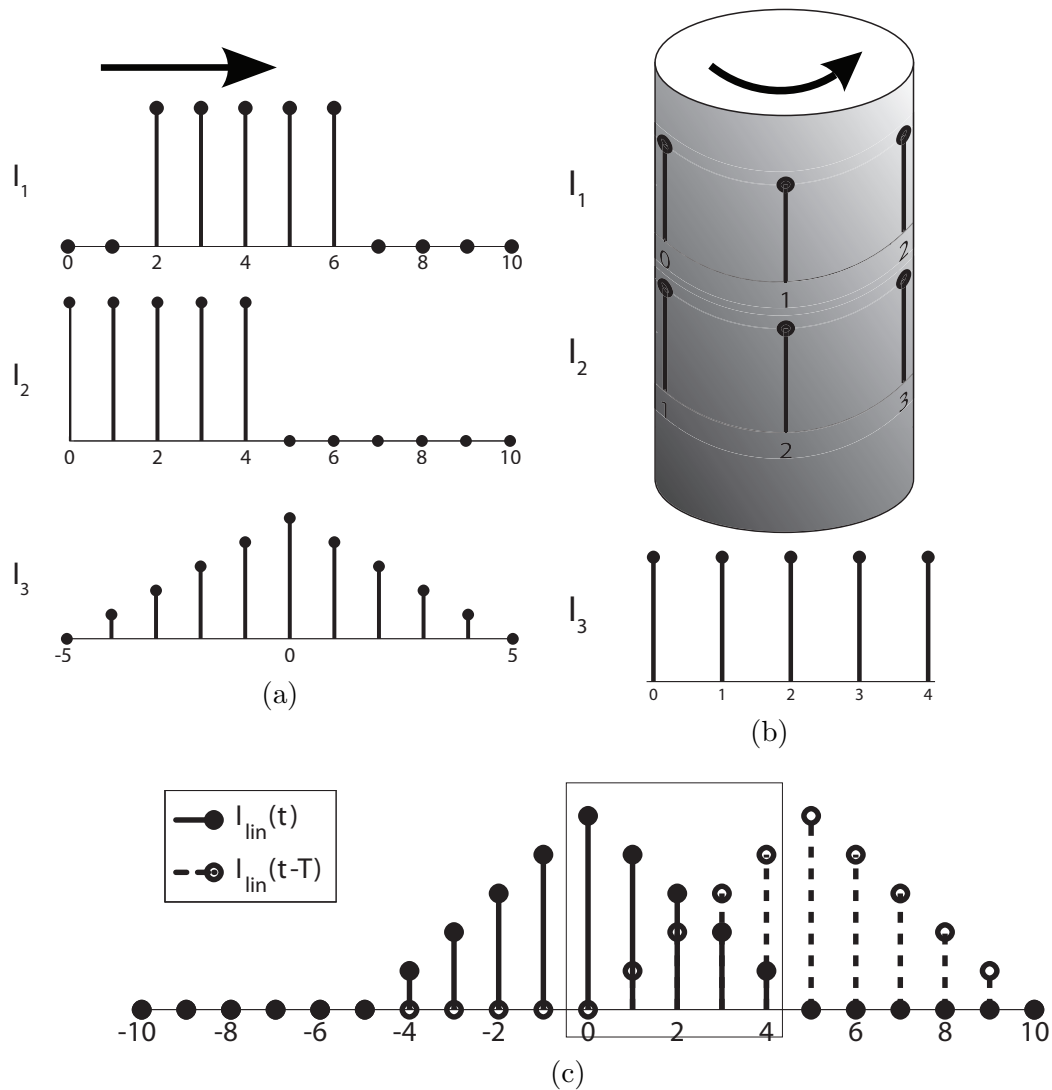


Figure 2.2: Periodic convolution as linear plus aliasing. a) Linear convolution of sequence I_1 and I_2 gives I_3 . b) Circular convolution of I_1 and I_2 gives I_3 . Sequences are wrapped around the circumference of a cylinder and shifted by turning them around the shaft. c) The periodic convolution in (b) equals the sum of linear convolution (a), shifted by the sequence length T .

It can be shown that this estimator is *unbiased* (i.e. converge to the correlation function) and *consistent* (i.e. its variance goes to zero) as T increases. However, as m increases (longer lags), less and less samples are used to estimate the correlation function. This leads to extremely volatile edges that can distort analysis. An interesting way to circumvent the problem is to use a circular correlation estimate:

$$\check{\phi}_I[m] = \frac{1}{T} \sum_{n=1}^T I[n] I[(n + |m|)_T] = \frac{1}{T} I[n] \otimes^L I[-n] \quad (2.27)$$

As the periodic correlation is nothing more than a periodic convolution, $\check{\phi}_I[m]$ is equivalent to the aliased $\hat{\phi}_I[m]$. In other words, long positive lags will be added to the short negative lags and vice versa. In consequence, noise is reduced at the expense of not being able to differentiate long lags in one direction versus short lags in the other. In some situations where there is no need for distinction (or it is obvious, e.g. in STICS), this method can be useful.

A discrete convolution essentially scales as $\mathcal{O}(N^2)$; there are N multiplications for each of the N lags. Advances in efficient FFT algorithms can reduce this to $\mathcal{O}(N \log(N))$ by doing the computation in Fourier space. The efficiency gain is particularly important while analyzing large multidimensional data structures (i.e. for d dimensions $\mathcal{O}(N^{2d})$ vs. $\mathcal{O}(N^d \log(dN))$).

2.3.4 Spectral estimation and windowing

The information conveyed in the correlation function is sometimes more easily interpreted in the power spectrum. If we multiply our signal by a *window function*, $w[m]$, before taking the Fourier transform:

$$V(\omega) = \sum_{n=1}^T w[n] I[n] e^{-i\omega n} \quad (2.28)$$

We can write an estimator for the power spectrum, also known as the *periodogram*:

$$\hat{P}_I(\omega) = \frac{1}{U} |V(\omega)|^2 \quad (2.29)$$

where $U = \sum_{n=1}^T (w[n])^2$ is a normalization constant so that the estimator is unbiased. At this point, the reader might wonder why we decided to multiply our signal by a window function. One should note that we are considering here samples of finite-length signals. We are therefore “peeking” through a finite window, a rectangular or boxcar window of length T , on the infinite signal. Remembering from section 2.2.1 that the power spectrum is the Fourier transform of the correlation function and noting that our sample is a product of the infinite signal and the window, it is straightforward to show that:

$$\mathcal{E}\{\hat{P}_I(\omega)\} = \frac{1}{2\pi U} \int_{-\pi}^{\pi} P_I(\theta) C_{ww}(\omega - \theta) d\theta \quad (2.30)$$

where $C_{ww} = |W(\omega)|^2$ is the Fourier transform of the autocorrelation function of the window and where we used the convolution-modulation theorem. In other words, the estimate of the power spectrum is equal to the real power spectrum convolved with C_{ww} . As the window becomes longer, C_{ww} tends toward a Dirac delta, allowing resolution of sharp peaks. However, as the windows gets shorter, the width of C_{ww} is increased, the spectrum is smoothed and the resolution is degraded.

The rectangular window has the well known sinc squared spectrum. It has the sharpest resolution (central peak) but also the highest sidelobes. This can create artefacts in the spectrum. There are many other window functions that achieve a trade-off between lower sidelobes, at the expense of a loss in resolution. A summary of the properties of different windows can be found in Oppenheim [64, p. 539-544] while a comprehensive review was made by Harris [69].

Another important property of the estimator (2.29) is that it is *not* consistent. That is, its variance does not asymptotically goes to zero as the window size increases

[70]. This particular behavior can be best understood in real space. Effectively, this estimator can be interpreted as the Fourier transform of the correlation function estimator (2.26). However, we saw that this estimator was noisy in the long lags. These long lags will be used to compute every frequency, thereby spreading the noise everywhere in the periodogram. Two main approaches are used to overcome this problem. First, Bartlett [71] and Welch [72] studied extensively the method of averaging periodogram. This method consists in splitting the signal in smaller segments, computing their periodogram according to (2.29) and averaging them. This procedure reduces the variance of the periodogram by the number of segments and is therefore a consistent estimator¹. Welch also showed that the segments can overlap by as much as half their length while still being independent, thus reducing the variance by almost another factor of two.

The second approach is to first compute the correlation function according to (2.26), window it by selecting only region of acceptable noise and then take the Fourier transform. We therefore have:

$$\mathcal{E}\{\check{P}_I(\omega)\} = \frac{1}{2\pi} \int_{-\pi}^{\pi} P_I(\theta) W_c(\omega - \theta) d\theta \quad (2.31)$$

where $W_c(\omega)$ is the Fourier transform of the window. This is an unbiased estimator if the window is normalized so that $w_c[0] = 1$. Note the difference with (2.29); since we are windowing directly in correlation space, the Fourier transform of the window is not squared. This estimator is also consistent [70] and therefore provides an alternative way to estimate the power spectrum. It can provide a more straightforward method to find the amount of averaging necessary for a particular signal in a particular analysis.

¹As T goes to infinity, both the length of the window and the number of windows go to infinity.

2.4 Spatio-temporal image correlation spectroscopy

Let's return to the study of biological processes with biophysical fluctuation analysis. This section was derived with fluorescence microscopy imaging in mind, but it can be used in a different context. Acquiring a series of images via an imaging modality, we want to characterize the dynamics of N point emitters, for example fluorescently tagged proteins. For the following discussion, we suppose that the time to acquire an image is negligible, so that all spatial coordinates are sampled simultaneously. We also neglect molecules with fast dynamics which will not correlate on the time scale of imaging, as they will only produce noise in our correlation function. We can represent the acquired image pixel intensities as:

$$I(\vec{r}, t) = \sum_{i=1}^N B_i(t) B_0 \delta(\vec{r} - \vec{r}_i(t)) \otimes_{\vec{r}} I_p(\vec{r}) \quad (2.32)$$

where B_0 represents the brightness of the probe (including all constant terms related to the acquisition system), $B_i(t)$ the photophysics (0 or 1 depending on the bleaching and/or blinking of the molecule i at time t), $\vec{r}_i(t)$ the position of particle i at time t , $I_p(\vec{r})$ is the PSF of our imaging system and the subscript on the convolution specify on which dimension we are convolving. Note the use of vectors so that the formalism developed may be use in 2D or 3D imaging systems. Since $\vec{r}_i(t)$ is a random variable, $I(\vec{r}, t)$ will also be a random variable. Therefore, it is useful to use the correlation function:

$$R(\vec{\xi}, \tau) = \frac{1}{L_{\vec{r}, t}} I(\vec{r}, t) \otimes_{\vec{r}, t} I(-\vec{r}, -t) \quad (2.33)$$

where $L_{\vec{r}, t}$ total number of samples (e.g. $L_x \times L_y \times L_t$) and $\vec{\xi}$ the spatial lag variable. Since the PSF is only a variable of space, it is useful to consider separately spatial and time variables. By inserting (2.32) into (2.33) and taking the Fourier transform in space, we obtain:

$$\begin{aligned}
R(\vec{\xi}, \tau) &= \frac{B_0^2}{L_{\vec{r},t}} \sum_i \mathcal{F}_{\vec{r}}^{-1} \left\langle \tilde{I}_p e^{2\pi i \vec{k} \cdot \vec{r}_i(t)} \tilde{I}_p^* e^{-2\pi i \vec{k} \cdot \vec{r}_i(t+\tau)} B_i(t) B_i(t+\tau) \right\rangle_t \\
&\quad + \frac{B_0^2}{L_{\vec{r},t}} \sum_{i \neq j} \mathcal{F}_{\vec{r}}^{-1} \left\langle \tilde{I}_p e^{2\pi i \vec{k} \cdot \vec{r}_i(t)} \tilde{I}_p^* e^{-2\pi i \vec{k} \cdot \vec{r}_j(t+\tau)} B_i(t) B_j(t+\tau) \right\rangle_t \quad (2.34)
\end{aligned}$$

where \tilde{I}_p is the Fourier transform of the correlation function, \mathcal{F}^{-1} the inverse Fourier transform operator and where we separated the self and the cross terms. We will now make two simplifying assumptions. First, we will suppose that the particles are independent. Second, we will suppose that the photophysics is only time dependent and hence is independent of the position. We can therefore rewrite the correlation function as a product of averages:

$$R(\vec{\xi}, \tau) = \frac{B_0^2 N}{L_{\vec{r},t}} \mathcal{F}_{\vec{r}}^{-1} \left\langle |\tilde{I}_p|^2 e^{2\pi i \vec{k} \cdot (\vec{r}_i(t) - \vec{r}_i(t+\tau))} \right\rangle_t \Theta(t, \tau) + \langle I \rangle^2 \quad (2.35)$$

where we defined the photophysics correlation function $\Theta(t, \tau) = \langle B(t) B(t+\tau) \rangle$, used ergodicity to get rid of the sum (time average over a single particle equals ensemble average) and where the second term simplified because N is large and the particles are independent. If we now define the autocorrelation of the PSF, $C_{PP}(\vec{r}) = \mathcal{F}_{\vec{r}}^{-1}(|\tilde{I}_p|^2)$, we can write the following:

$$R(\vec{\xi}, \tau) = \frac{B_0^2 N}{L_{\vec{r},t}} \Theta(t, \tau) C_{PP}(\vec{r}) \otimes_{\vec{r}} \langle \delta(\vec{r} - (\vec{r}_i(t) - \vec{r}_i(t+\tau))) \rangle + \langle I \rangle^2 \quad (2.36)$$

Since the molecules are distributed randomly, we will set $\vec{r}_i(t) = 0$ for simplicity. Switching to ensemble averaging:

$$\begin{aligned} \langle \delta(\vec{r} + \vec{r}_i(t + \tau)) \rangle &= \int \delta(\vec{r} + \vec{r}_i(t + \tau)) P_{\vec{r}_\tau | \vec{r}_t}(\vec{r}_i(t + \tau) | \vec{r}_i(t) = 0) \\ &P_{\vec{r}_i}(\vec{r}_i(t) = 0) d\vec{r}_i(t) d\vec{r}_i(t + \tau) \end{aligned} \quad (2.37)$$

$$= P_{\vec{r}_\tau | \vec{r}_t}(-\vec{r} | \vec{r}_i(t) = 0) \quad (2.38)$$

where we used the fact that integrating over all possible states equals 1 and properties of the Dirac delta function. In words, this function represents the probability of finding a particle at some point in space if you know its original position. We can therefore write what we will name the STICS *master equation*:

$$R(\vec{\xi}, \tau) = \frac{B_0^2 N}{L_{\vec{r}, t}} \Theta(t, \tau) C_{PP}(\vec{r}) \otimes_{\vec{r}} P_{\vec{r}_\tau | \vec{r}_t}(-\vec{r} | \vec{r}_i(t) = 0) + \langle I \rangle^2 \quad (2.39)$$

This equation explains the behavior of the correlation function for any type of underlying molecular dynamics. We will now derive the equations for simple dynamics, from which it can easily be generalized.

2.4.1 Image correlation spectroscopy

Let's start by determining the amplitude of the correlation peak. Since convolving the Dirac delta in that case merely shifts the function at the origin:

$$R(0, 0) = \frac{B_0^2 N}{L_{\vec{r}, t}} \Theta(t, 0) C_{PP}(0) + \langle I \rangle^2 \quad (2.40)$$

Two variables are interesting to extract biologically; B_0 and N . Noting that $\langle I \rangle = NB_0 \Theta(t, 0) C_{PP}(0) / L_{\vec{r}, t}$, we define a normalized correlation function:

$$r(\vec{\xi}, \tau) = \frac{R(\vec{\xi}, \tau)}{L_{\vec{r}, t} \langle I \rangle^2} - 1 \quad (2.41)$$

so that

$$r(0, 0) = \frac{1}{N\Theta(t, 0)C_{PP}(0)} \quad (2.42)$$

Remembering our discussion from section 2.2.1, but now applying it in space, $C_{PP}(0)$ is simply a measure of the area/volume of the PSF (its variance, or spread). Moreover, $\Theta(t, 0)$ represents the average fraction of emitting particles during the time window. This is why $1/r(0, 0)$ is often referred to as the number of particles per beam area (BA) or volume. When applied to a single frame, this technique is named image correlation spectroscopy (ICS). The PSF is often approximated by a Gaussian of the form:

$$I_P(r) = e^{-2r^2/w_r^2} \quad (2.43)$$

so that its autocorrelation is simply a Gaussian two times wider:

$$C_{PP}(\vec{\xi}) = \pi w_r^2 \exp\left(-|\vec{\xi}|^2/w_r^2\right) \quad (2.44)$$

and that $C_{PP}(0) = \pi w_r^2$ and w_r is the e^{-2} radius of the Gaussian PSF.

2.4.2 Flow

A uniform flow is essentially a deterministic process. If \vec{v} is the flow velocity, then:

$$P_{\vec{r}_\tau|\vec{r}_t}(-\vec{r}|\vec{r}_i(t) = 0) = \delta(\vec{r} + \vec{v}\tau) \quad (2.45)$$

Thus, equation (2.39) becomes:

$$R_{flow}(\vec{\xi}, \tau) = \frac{B_0^2 N}{L_{\vec{r}, t}} \Theta(t, \tau) C_{PP}(\vec{\xi} + \vec{v}\tau) + \langle I \rangle^2 \quad (2.46)$$

That is, the correlation function is equal to the autocorrelation of the PSF shifted by $-\vec{v}\tau$ and multiplied by the photophysics function.

2.4.3 Diffusion

We shall now consider uniform diffusion in d dimensions. The probability equation (2.38) is equivalent to the Green's function of the heat/diffusion equation:

$$P_{\vec{r}_\tau|\vec{r}_i}(-\vec{r}|\vec{r}_i(t)=0) = \frac{1}{(4\pi D\tau)^{d/2}} e^{-r^2/4D\tau} \quad (2.47)$$

Therefore, convolving with (2.47) has the effect of spreading the correlation function as τ increases. For example considering the Gaussian PSF with 2D diffusion, equation (2.39) becomes:

$$R_{diff}(\vec{\xi}, \tau) = \frac{B_0^2 N}{L_{\vec{r},t}} \Theta(t, \tau) \frac{w_r^2}{(w_r^2 + 4D\tau)} \exp\left(\frac{-|\vec{\xi}|^2}{w_r^2 + 4D\tau}\right) + \langle I \rangle^2 \quad (2.48)$$

2.4.4 Diffusion + flow

One can think of a particle undergoing simultaneous diffusion and flow as a more realistic biological model of molecular transport. In that case, the probability distribution for biased diffusion is:

$$P_{\vec{r}_\tau|\vec{r}_i}(-\vec{r}|\vec{r}_i(t)=0) = \frac{1}{(4\pi D\tau)^{d/2}} e^{-|\vec{r} + \vec{v}\tau|^2/4D\tau} \quad (2.49)$$

which is the same as (2.47) but with an average velocity $-\vec{v}$. Keeping the same assumptions as in last section:

$$R_{diff+flow}(\vec{\xi}, \tau) = \frac{B_0^2 N}{L_{\vec{r},t}} \Theta(t, \tau) \frac{w_r^2}{(w_r^2 + 4D\tau)} \exp\left(\frac{-|\vec{\xi} + \vec{v}\tau|^2}{w_r^2 + 4D\tau}\right) + \langle I \rangle^2 \quad (2.50)$$

2.4.5 Cross-correlation

For the sake of simplicity, this section was derived as the autocorrelation in a single channel. Let's briefly state the important differences while analyzing the cross-correlation. Suppose we are imaging different kind of fluorophores in two distinct

detection channels. We can rewrite 2.34, but summing only over interacting particles:

$$R_{ab}(\vec{\xi}, \tau) = \frac{B_{0a}B_{0b}}{L_{\vec{r},t}} \sum_i \mathcal{F}_{\vec{r}}^{-1} \left\langle \tilde{I}_{Pa} e^{2\pi i \vec{k} \cdot \vec{r}_{ia}(t)} \tilde{I}_{Pb}^* e^{-2\pi i \vec{k} \cdot \vec{r}_{ib}(t+\tau)} B_{ia}(t) B_{ib}(t+\tau) \right\rangle_t + \langle I_a \rangle \langle I_b \rangle \quad (2.51)$$

Since the photophysics is independent between channels:

$$R_{ab}(\vec{\xi}, \tau) = \frac{B_{0a} \langle B_a(t) \rangle B_{0b} \langle B_b(t) \rangle N_{ab}}{L_{\vec{r},t}} C_{ab}(\vec{r}) \otimes_{\vec{r}} P_{\vec{r}_{\tau,b} | \vec{r}_{t,a}}(-\vec{r} | \vec{r}_a(t) = 0) + \langle I_a \rangle \langle I_b \rangle \quad (2.52)$$

where we defined $C_{ab}(\vec{r}) = \mathcal{F}^{-1} \left\{ \tilde{I}_{Pa} \tilde{I}_{Pb}^* \right\}$ the cross-correlation between the two PSFs. This function will not be necessarily centered at zero depending on the alignment of the two channels. Improper alignment will merely shift the correlation function, thereby automatically correcting for the misalignment of the two channels. There is also no lag dependence on the photophysics function. Furthermore, the conditional probability in that case has to be interpreted as: where is particle b likely to be found at a later time, knowing the position of a particle a at some time. Finally, there is a need for a double normalization in order to extract N_{ab} . Indeed, the normalized correlation peak will give:

$$r_{ab}(0, 0) = \frac{\langle B_a(t) \rangle \langle B_b(t) \rangle N_{ab} C_{ab}(0)}{N_a N_b \langle B_a^2(t) \rangle \langle B_b^2(t) \rangle C_{aa}(0) C_{bb}(0)} \quad (2.53)$$

Thus:

$$\frac{r_{ab}(0, 0)}{r_{aa}(0, 0) r_{bb}(0, 0)} = \langle B_a(t) \rangle \langle B_b(t) \rangle N_{ab} C_{ab}(0) \quad (2.54)$$

2.5 Multiple populations

Not all tagged proteins will behave the same way; they often can be grouped in independent *populations*. For example, a significant fraction of the proteins may be

immobilized on the cell surface while another population diffuses and another is being actively transported (i.e. flowing). Assuming no interaction between populations, we can do the same derivation as in section 2.4 but summing over individual subgroup to obtain:

$$R(\vec{\xi}, \tau) = \sum_k N_k R_k(\vec{\xi}, \tau) + \langle I \rangle^2 \quad (2.55)$$

where we assumed for simplicity that they have the same brightness (different brightness would simply add a weighting factor). Defining the fraction of molecules in a population $f_k = N_k/N$:

$$r(\vec{\xi}, \tau) = \sum_k f_k r_k(\vec{\xi}, \tau) \quad (2.56)$$

where

$$r_k(\vec{\xi}, \tau) = \frac{\Theta(t, \tau)}{NC_{PP}(0)^2 \Theta(t, 0)^2} C_{PP}(\vec{r}) \otimes_{\vec{r}} P_{\vec{r}_{\tau, k} | \vec{r}_{t, k}}(-\vec{r} | \vec{r}_k(t) = 0) \quad (2.57)$$

The total correlation function is therefore a sum of the individual functions weighted by their respective fraction. This is why a population representing a vast majority of the molecules can overshadow smaller dynamics. This effect has motivated the developments described in chapter 3. Note that it is possible to extract f_k by normalizing by the total peak amplitude:

$$\frac{r_k(0, 0)}{r(0, 0)} = f_k \quad (2.58)$$

Frequency space techniques

I**N** section 2.4, we developed a theoretical framework for characterizing molecular dynamics using the correlation function of the measured intensity, $I(x, y, t)$, of a fluorescent protein. However, we saw in section 2.2.1 that the correlation function and the power spectrum are two different spaces carrying the same information but presented in different ways. Therefore, this chapter will explore how those different spaces can help us in our analysis. We will start by showing that k-space image correlation spectroscopy (kICS) is the time correlation of the spatial power spectrum of $I(x, y, t)$. After that, two new and previously unpublished spaces of analysis will be introduced. Finally, using the knowledge from digital signal-processing, we will introduce new ways of filtering the time series to aid measurements on complex cellular systems.

3.1 *k-space image correlation spectroscopy*

The kICS technique was recently developed [73, 74] in the Wiseman lab to allow measurement of diffusion and photophysics of fluorescently tagged macromolecules in cells. The reciprocal space correlation function is defined as the correlation function of the spatial Fourier transform of the signal:

$$R(\vec{k}, \tau) = \left\langle \tilde{I}(\vec{k}, t) \tilde{I}(\vec{k}, t + \tau) \right\rangle_t \quad (3.1)$$

However, if we take the spatial Fourier transform of both sides of the definition of

the correlation function (equation 2.33), we see that:

$$R(\vec{k}, \tau) = \mathcal{F}_{\vec{r}}(R(\vec{r}, \tau)) \quad (3.2)$$

In other words, the kICS correlation function is the spatial Fourier transform of the STICS correlation function, or the temporal correlation of the spatial power spectrum. The kICS master equation can then be obtained by Fourier transforming its STICS counterpart (2.39):

$$R(\vec{k}, \tau) = \frac{B_0^2 N}{L_{\vec{r}, t}} \Theta(t, \tau) \tilde{C}_{PP}(\vec{k}) \mathcal{F}_{\vec{r}} \{ P_{\vec{r}_\tau | \vec{r}_t}(-\vec{r} | \vec{r}_i(t) = 0) \} \quad (3.3)$$

where we used the convolution theorem and $\tilde{C}_{PP}(\vec{k}) = |\tilde{I}_p|^2$ is the power spectrum of the PSF. Note that we used a definition of the “mean-corrected” intensity ($\delta I = I - \langle I \rangle$) to simplify notation. Furthermore, it is always good practice to remove the average before taking the Fourier transform to avoid leaking of this strong component into other frequencies. The strengths of kICS lie in the transformation of the convolution of the dynamics with the PSF in a simple product. To find the form of the correlation function for different molecular dynamics, one only has to do the Fourier transform of the conditional probability. Let’s review the simple dynamic cases derived for STICS. For a simple flow, the Fourier transform of a Dirac delta is simply a phase factor. Thus, equation (2.46) becomes:

$$R_{flow}(\vec{k}, \tau) = \frac{B_0^2 N}{L_{\vec{r}, t}} \Theta(t, \tau) \tilde{C}_{PP}(\vec{k}) \exp(-2\pi i \vec{v} \cdot \vec{k}) \quad (3.4)$$

For a biased diffusion in d dimensions, we have:

$$R_{diff+flow}(\vec{k}, \tau) = \frac{B_0^2 N}{L_{\vec{r}, t}} \Theta(t, \tau) \tilde{C}_{PP}(\vec{k}) \exp(-2\pi i \vec{v} \cdot \vec{k} - 4D\tau |\vec{k}|^2) \quad (3.5)$$

since the Fourier transform of a Gaussian is another Gaussian. Note that there is no dependence on d , as long as the imaging is performed over the same number of

dimensions as the diffusion (see [73, 74] for other cases). Also, by approximating the PSF as a Gaussian, its power spectrum will be another Gaussian and will simply add a constant in the exponential term.

3.1.1 *kICS bias*

Equations (3.4-3.5) have a simple yet deceptive form. While working with real (finite) data sets, one must remember our discussion of section 2.3.4 about power spectrum estimation. First, an estimation method must be chosen between periodogram averaging and correlation windowing. Second, the correlation function obtained will be a convolution of equation (3.5) with the Fourier transform of the spatial window function, C_{ww} . Remember here that the spatial window is equal to the region of interest (ROI) size or smaller if averaging was undertaken. We emphasize this effect here because previously data fitting in *kICS* was done directly with equation (3.5). For large windows, C_{ww} converges to a Dirac delta and therefore the convolution has no effect. In that case, equation (3.5) is a valid approximation. However, as the window gets smaller (i.e. smaller ROI), the approximation is no longer valid and (3.5) is deformed. This was previously described as the *kICS bias* for small ROI [75]. In his extensive characterization of the bias, Schwartzentruber described a bias in diffusion coefficients obtained with *kICS* depending only on spatial sampling (number of beam area per region of analysis). Using a window function (i.e. not a rectangular one) led to less deformation of (3.5). We will show in section 4.3.2 that a similar effect can be seen in other correlation spaces and that the accurate correction is to fit the convolution of (3.5) with the window function used to calculate the correlation function with the data. Good numbers to keep in mind are that the bias range from an acceptable 10% to up to 50% for 100 to 10 beam area per ROI, respectively.

3.2 k - ν -space image correlation spectroscopy

kICS provides an interesting space that separates the contribution from the dynamics, the PSF and the fluorophore's photophysics into a simple product. It does not, however, solve the problem of fitting multiple populations. A dominant immobile population will still overshadow small dynamics in k -space. A way to separate populations according to their dynamics is to go in time-frequency space, or ν -space. This section will consider the space-time power spectrum of the fluorescent intensity, what we will name k - ν -space image correlation spectroscopy (knICS). If we take the time Fourier transform of equation (3.3), we obtain the knICS master equation:

$$R(\vec{k}, \tau) = \frac{B_0^2 N}{L_{\vec{r}, t}} \tilde{C}_{PP}(\vec{k}) \mathcal{F}_{\vec{r}, t} \{ P_{\vec{r}_\tau | \vec{r}_t}(-\vec{r} | \vec{r}_i(t) = 0) \} \otimes \tilde{\Theta}(\nu) \quad (3.6)$$

where $\tilde{\Theta}(\nu)$ is the Fourier transform of the photophysics function, $\Theta(\tau)$. On first examination, equation (3.6) seems only to have complicated the problem. The correlation function is now convolved by the reciprocal of the photophysics function. This suggests that knICS will be more sensitive to the photophysics. However, in most cases photobleaching can be “detrended” by adding a random number whose mean is equal to the required number to flatten the image time series [76, 77]. Furthermore, on the time scale of molecular transport, fluorescent protein blinking will appear only as a lower effective quantum yield. This encourages us to pursue our analysis. For a simple flow, taking the time Fourier transform of (3.4) shows how knICS can be useful:

$$R_{flow}(\vec{k}, \nu) = \frac{B_0^2 N}{L_{\vec{r}, t}} \tilde{C}_{PP}(\vec{k}) \delta(\nu + \vec{v} \cdot \vec{k}) \otimes \tilde{\Theta}(\nu) \quad (3.7)$$

For simplicity, we ignore for now the photophysics and see that a flowing population will be folded on the $(\nu + \vec{v} \cdot \vec{k}) = 0$ plane. Therefore, an immobile population will be concentrated around the $\nu = 0$ plane and we will be able to resolve faster but less present dynamics. What about biased diffusion? By straightforward manipulations,

equation (3.5) becomes:

$$R_{diff+flow}(\vec{k}, \nu) = \frac{B_0^2 N}{L_{\vec{r}, t}} \tilde{C}_{PP}(\vec{k}) \frac{8D|\vec{k}|^2}{\left(4D|\vec{k}|^2\right)^2 + 4\pi^2 \left(\nu + \vec{v} \cdot \vec{k}\right)^2} \otimes \tilde{\Theta}(\nu) \quad (3.8)$$

because the Fourier transform of an exponential is a Lorentzian. Let's first consider the $\vec{v} = 0$ case (diffusion only). For each value of $|\vec{k}|^2$, there will be a Lorentzian in ν , with scale parameter $4D|\vec{k}|^2$. For the case of a very slow diffusion, (3.8) will go towards a plane, while at high D , it will go towards a tunnel along ν (no dependence in ν and divergence near $|\vec{k}|^2 = 0$). For a biased diffusion, the same function is simply centered on the $(\nu + \vec{v} \cdot \vec{k}) = 0$ plane. Therefore, as would be expected intuitively, a biased diffusion will have an effect similar to spectral broadening in our power spectrum space. The plane corresponding to the flow will be spread and will decay faster around the edges, leading to a loss of resolution.

As in kICS, \tilde{C}_{PP} is related to the resolution limit. Effectively, the smaller the PSF, the larger \tilde{C}_{PP} will be and higher spatial frequencies will be resolvable. As the PSF grows larger, \tilde{C}_{PP} will become smaller and only a small portion of the correlation function can be seen. Also, the same discussion related to the window function still holds. That is, while working with finite data sets, the computed power spectrum will be a convolution of equation (3.6) and C_{ww} , the space-time Fourier transform of the space-time window function.

3.3 ν -space image correlation spectroscopy

The previous section showed that the time Fourier transform helped to separate the populations according to their dynamics, but the use of k-space was not necessary. In the quest of separating flowing from immobile populations, we now consider ν -space image correlation spectroscopy (nICS), which can be understood as the spatial correlation of the temporal power spectrum. Taking the time Fourier transform of

the mean corrected equation (2.39) gives the master nICS equation:

$$R(\vec{\xi}, \nu) = \frac{B_0^2 N}{L_{\vec{r}, t}} (C_{PP}(\vec{r}) \otimes_{\vec{r}} \mathcal{F}_t \{P_{\vec{r}_r | \vec{r}_t}(-\vec{r} | \vec{r}_i(t) = 0)\}) \otimes \tilde{\Theta}(\nu) \quad (3.9)$$

Equation (3.9) is not very telling on first examination. Indeed, the time Fourier transform of the conditional probability is not trivial. Consequently, we computed the equation for a flow with a Gaussian PSF (by convoluting separately different dimensions), and obtained:

$$R_{flow}(\vec{\xi}, \nu) = \frac{B_0^2 N}{L_{\vec{r}, t}} \frac{\sqrt{\pi} w_r}{|v|} \exp\left(-\left(\frac{\pi \nu}{v/w_r}\right)^2\right) \exp\left(-\left(\frac{v_x \eta - v_y \xi}{v w_r}\right)^2\right) \exp\left(-2\pi i \nu \frac{\vec{v} \cdot \vec{\xi}}{v^2}\right) \quad (3.10)$$

By taking the limit of $v \rightarrow 0$, we obtain a Dirac delta for the plane $\nu = 0$. As in the case of knICS, the immobile population will be concentrated in a single plane. Similarly to kICS, the velocity can be extracted with the phase. However, it is difficult to find an analytical expression for diffusion due to the shape of the probability distribution. While it can be interesting to see how this technique holds up in the fitting procedures, we leave further investigation of nICS for future work.

3.4 Immobile filtering

Since different populations are concentrated in different parts of the frequency spectrum, another approach to separating them is to filter them out before computing the correlation function. This approach has the advantage that a dominant population like the immobile one will be removed before computation of the correlation function, therefore minimizing leakage of this component. However, it will affect and, to some extent, distort all the other populations. Previously, the immobile fraction was removed by *Fourier filtering* [55]. The suggested procedure was to take the time Fourier

transform of an image series and remove the zero frequency component. Therefore, the filtered intensity is:

$$I_f(x, y, t) = \mathcal{F}_t^{-1} \left\{ \mathcal{F}_t \{ I(x, y, t) \} H_{1/T}(\nu) \right\} \quad (3.11)$$

where $H_{1/T}(\nu)$ is the Heaviside function and T the length of the time series. However, this method has multiple problems. First, we saw in section 2.3.2 that the DFT simply samples the DTFT of the periodically extended signal at definite interval. Moreover, this spectrum is convolved by the Fourier transform of the window function, a sinc if there was no windowing. All this can lead to severe artifacts in the filtered data. Finally, this filter depends on the total length of the time series we are interested in (i.e. $H_{1/T}(\nu)$). We will show in section 4.2.1 that this can drastically affect the results when we vary the sample length (number of images). Decomposing our sample in smaller subsets can be very useful, for example to look at the time evolution of particular dynamics in cells. Therefore, the behavior of this filter is sample dependent and unacceptable. In the next section, we will develop a filter that does not depend on the length of the time series analyzed, that introduces few artifacts in the analysis and can be tuned to filter specific dynamics.

3.4.1 Linear filtering

The study of discrete-time linear time-invariant systems (LTI) is outside the scope of this thesis. Detailed references such as [64] are recommended to the interested reader. The general idea is to convolve the signal with an *impulse response*, $h[m]$, to filter our data. The impulse response is so-called because it is defined as the response of a LTI system to a impulse function. Therefore, knowing $H(\omega)$, the DTFT of $h[m]$, tells us the frequency response of the system. $H(\omega)$ is appropriately named the *frequency response* of the system. Because the convolution is a linear operator, this type of filtering will also be linear. In other words, filtering a sum of signals will give the sum of the filtered signals. There exist two main types of filters: those that have a *finite*

impulse response (FIR) and those that have an *infinite impulse response* (IIR).

FIR filters can be computed directly by evaluating the convolution sum. They are normally designed by *windowing*. One chooses a desired frequency response and take its inverse DTFT. This will normally give an impulse response of infinite length; limiting this impulse response to a reasonable number of points (much smaller than the length of the signal to be filtered) creates the FIR filter. The number of points will represent the filter order. The exact frequency response of the filter can be found by taking the DTFT of the windowed impulse function. A window function is often used as the sinc function has very high sidelobes and creates ripples in the frequency response. This type of filter generally has a linear phase response (phase shift grows linearly with frequency).

On the other hand, the IIR filter can be computed for example by recursion. The filtered intensity at some point will be a convolution of the previous intensity with the filter, summed with the convolution of the previously filtered signal. Such filters are similar to analog ones (e.g. RC circuit) and multiple methods exist to convert them in the digital form. They are generally more efficient than FIR filters but do not have a linear phase response.

For our application, we chose to design a first-order highpass Butterworth (IIR) filter to remove the immobile component. This type of filter was designed in 1930 by Stephen Butterworth [78] to have a maximally flat response in the passband. Thus, this filter will minimally affect the data we are interested in. Furthermore, we will show that we can find a simple analytical expression for the resulting filtered intensity and that, for correlation analysis, the phase response of the filter will cancel out.

For simplicity, we will derive the effects of the filter on the zero spatial lag correlation function for a single flow with a Gaussian PSF. In that case, the immobile component will be equivalent to a zero velocity. Also, in the case of a simple flow, the spatial lags correspond to a particular time lag. Therefore, knowing the effect on the zero spatial lag will give us the effect on the complete STICS correlation function.

For a flowing population with a Gaussian PSF, the intensity in one pixel is:

$$I(t) = \sum_{i=1}^N B_0 \exp(-2(x_i(t))^2/\sigma^2) \quad (3.12)$$

where w_r is the e^{-2} radius of the PSF and $x_i(t) = x_0 + vt$ is the position of particle i at time t . Therefore, the (mean-corrected) correlation function is:

$$\phi_I(\tau) = B_0^2 N^2 \exp(-(v\tau)^2/w_r^2) \quad (3.13)$$

In general, if we filter the intensity beforehand, denoting $F(t)$ the output of the filter $h(t)$:

$$\begin{aligned} \mathcal{E}\{\phi_F(\tau)\} &= \mathcal{E}\{F(t)F(t+\tau)\} \\ &= \mathcal{E}\left\{\int_k \int_l h(k)h(l)I(t-k)I(t+\tau-l)dkdl\right\} \\ &= \int_m \phi_I(\tau-m)dm \int_n h(n)h(n+m)dn \end{aligned} \quad (3.14)$$

In other words, the correlation function of the output of the filter, $\phi_F(\tau)$, is convolved with the autocorrelation of the filter impulse response. The power spectrum of $F(t)$ is then:

$$P_F(\omega) = |H(\omega)|^2 P_I(\omega) \quad (3.15)$$

The correlation function is filtered by the absolute value squared of the frequency response of the filter. This is why we do not need to care about the phase response of the filter. We will consider here the lowpass first-order Butterworth filter to find the shape of the filtered intensity. In that case, the frequency response has the shape of a Lorentzian function:

$$|H(\nu)|^2 = \frac{1}{1 + (\nu/\nu_c)^2} \quad (3.16)$$

where ν_c is the cutoff frequency of the filter. The filtered correlation function will be

convolved by the Fourier transform of (3.16), which is the double-sided exponential decay. Computing the convolution integral, we have:

$$\begin{aligned} \phi_F(\tau) &= \phi_I(\tau) - \\ &e^{\nu_c \pi \left(-2t + \frac{\nu_c \pi w_r^2}{v^2}\right)} \frac{\nu_c w_r}{2v} \pi^{3/2} w_r \cdot \\ &\left((1 + e^{4\nu_c \pi t}) - \text{Erf} \left[\frac{\nu_c \pi w_r}{v} - \frac{tv}{w_r} \right] - e^{4\nu_c \pi t} v \text{Erf} \left[\frac{\nu_c \pi w_r}{v} + \frac{tv}{w_r} \right] \right) \end{aligned} \quad (3.17)$$

Introducing two dimensionless variables, a $R = \pi w_r \nu_c / v$ ratio and a normalized time $T = tv / w_r$, this simplifies to:

$$\phi_F(\tau) = e^{-T^2} - \frac{1}{2} e^{R(R-2T)} \sqrt{\pi} R (1 - \text{Erf}[R - T] + e^{4RT} (1 - \text{Erf}[R + T])) \quad (3.18)$$

Equation (3.18) still looks rather daunting. This function is plotted for different values of R and T in figure 3.1a. We first see that the amplitude of the correlation function decays rapidly as R increases. In practice we are interested in two things: how does the amplitude of the correlation function is affected and how the shape is affected. Let's start by looking at the amplitude, or $\phi_F(0)$:

$$\phi_F(0) = 1 - \sqrt{\pi} e^{R^2} R (1 - \text{Erf}(R)) \quad (3.19)$$

Therefore, when considering a filter, one only has to consider the $R = \pi w_r \nu_c / v$ ratio. The velocity is normalized by the width of the PSF to give a *fluctuation frequency*; a fast particle with a large PSF will fluctuate similarly to a slow one with a small PSF. The removed intensity will only depend on the ratio of the cutoff frequency to this normalized velocity. Therefore, for specific conditions, it is straightforward to find a suitable cutoff frequency. As a rule of thumb, when $R = 1$ and 2 , the maximum value of the correlation function is equal to ~ 0.25 and 0.1 , respectively. What about the shape of the correlation function? By plotting the filtered correlation function

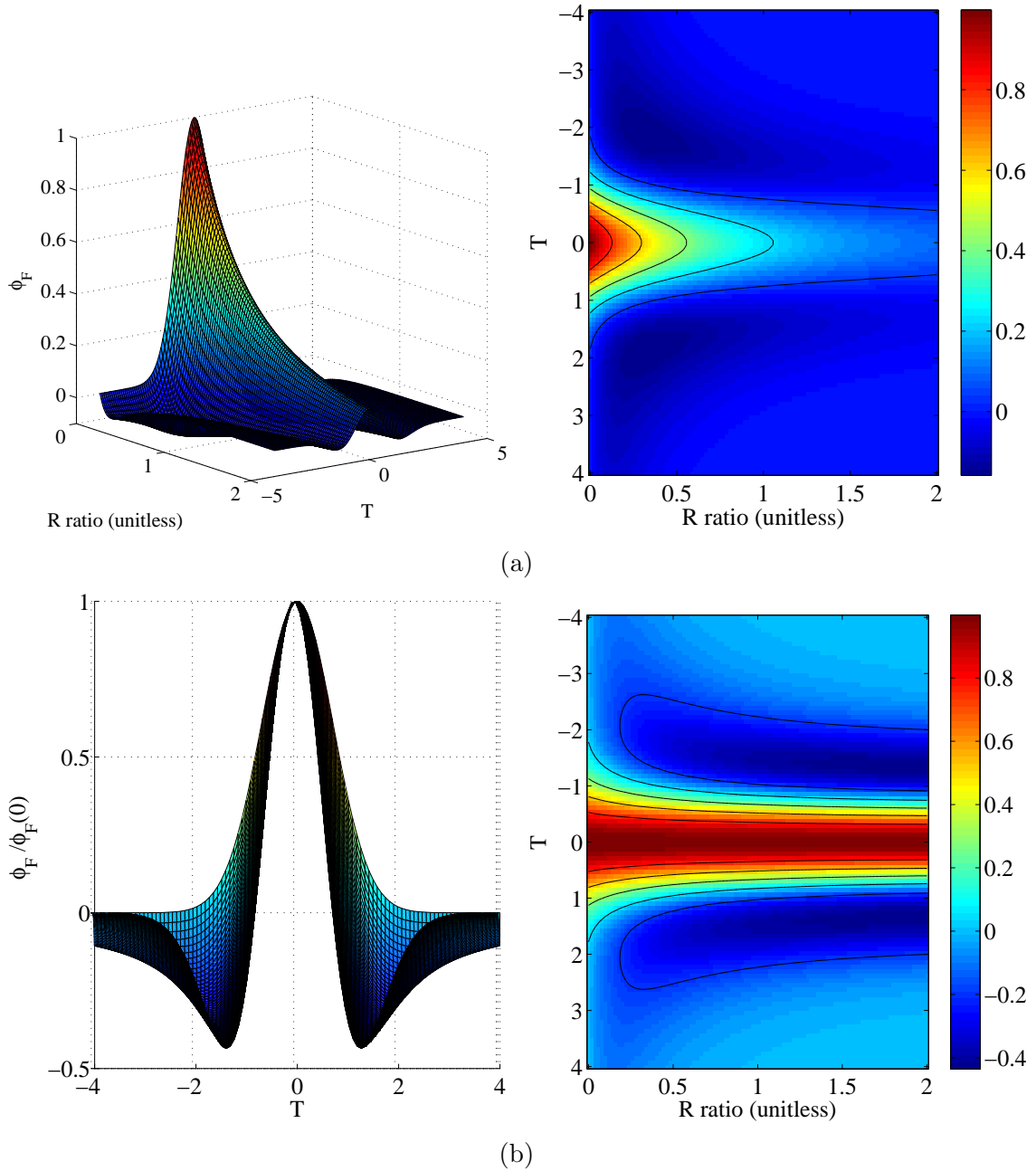


Figure 3.1: The effects of frequency filtering a simple flow on the correlation function. (a) The amplitude of the correlation function decays rapidly as R increases. (b) The change in shape is seen more clearly by normalizing the correlation function to the $T = 0$ amplitude.

(3.18) normalized by the $T = 0$ amplitude, equation (3.19), we can see clearly the effects on the shape of the correlation function, as shown in figure 3.1b. The effects are quite minimal and the correlation function can still be roughly approximated by a Gaussian. The error on the fitted width is not very important in STICS as we are interested in finding the center of mass at each time lags. This filter will be characterized in specific imaging situations in section 4.5.

Until now, we omitted diffusion from the discussion. The same development still holds for a diffusing population, but the calculations are more complicated due to the shape of equation (2.47). Also, we cannot simply suppose that the spatial lags will be equal to the zero one at different time lags as we did for the simple flow. For the sake of brevity, we will simply state the result for the amplitude of the filtered 2D diffusion correlation function, $\phi_{F,d}(0)$.

$$\phi_{F,d}(0) = 1 - Se^S E_1(S) \quad (3.20)$$

where we used a definition of the *exponential integral*, $E_1(x) = \int_x^\infty e^{-t}/t dt$ and defined another dimensionless ratio, $S = 2\pi\nu_c w_r^2/4D$. This variable has a striking similarity with R . The difference is that the fluctuation frequency is now $4D/w_r^2$ (instead of v/w_r). To illustrate this, we plotted the amplitude of the correlation function of filtered diffusion and flowing population sharing a similar time scale ($4Dw_r^2 = v/w_r$) with the same filter in figure 3.2. We observe that both populations are filtered similarly as we increase the cutoff frequency (increasing R and S). This suggests that frequency filtering would not be a good approach to separate flowing and diffusing population on similar time scales. This result was found empirically by Hebert in the development of the original Fourier filter [55, 79]. We conclude the section by noting that our filter satisfies the initial goals: it does not depend on the length of the time series to be analyzed, it can be tuned to select specific dynamics (by changing the cutoff frequency) and minimally alters our data.

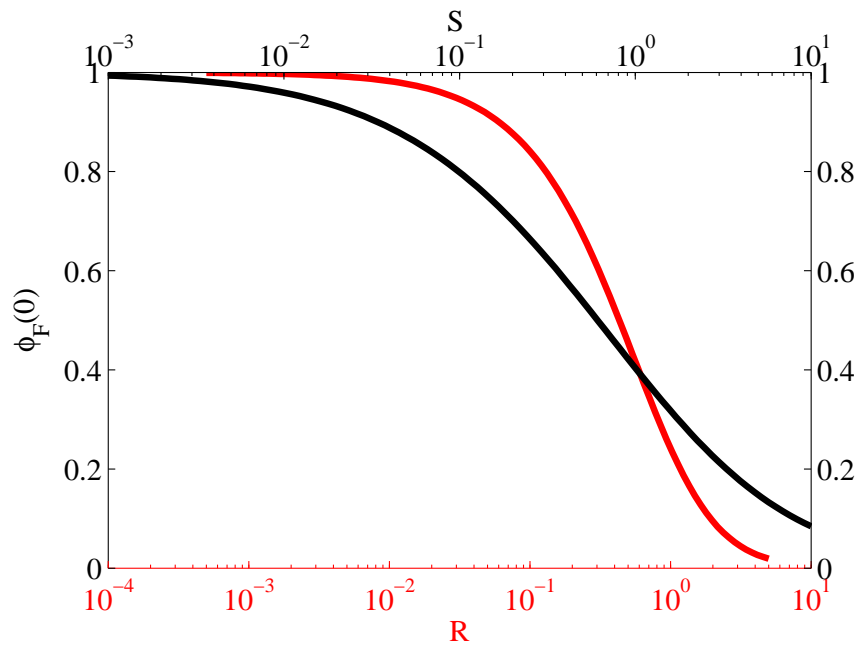


Figure 3.2: The filtered amplitude of the correlation function for flowing (red) and diffusing (black) population. The x axes were scaled so that the population fluctuated on the same time scale ($4D/w_r^2 = v/w_r$). The two populations are filtered similarly as the cutoff frequency of the filter is increased (R and S increases).

3.5 Symmetry filtering

A simple alternative to filtering is to use the fact that the only time asymmetric component in the correlation function is the flow. Effectively, a diffusing and/or immobile population behaves the same way backwards in time, as opposed to the flow that will move in the opposite direction. Therefore, one could define an asymmetric correlation function:

$$R_{asym}(\vec{\xi}, \tau) = R(\vec{\xi}, \tau) - R(\vec{\xi}, -\tau) \quad (3.21)$$

This can be seen as removing the correlation of the time reversed intensity. It is a simple way to isolate the flow without disturbing it. However, the correlation function is still computed with all the other populations, which can give a noisy asymmetric correlation if the other populations are very dominant. Furthermore, photobleaching and other non-stationary effects will be enhanced and should be corrected by “detrending”.

3.6 Cross-correlation

For the sake of simplicity, all the techniques developed in this chapter were shown for the autocorrelation of a single channel. We conclude this chapter by noting that generalization to cross-correlation is straightforward. For frequency-space analysis, we simply have to take the Fourier transform of the (mean-corrected) intensity of each channel and multiply them together. The discussion about cross-correlation analysis in STICS (section 2.4.5) still holds. The developments done for filtering still hold if we apply the same filter to both channels, as we have:

$$P_{ab,f}(\omega) = |H(\omega)|^2 P_{ab}(\omega) \quad (3.22)$$

However, caution must be maintained when applying the symmetry filter. For more complex dynamics, the cross-correlation may be inherently asymmetric in time (e.g. a time-delayed interaction). In that case, other methods should be considered.

Characterization *in silico*

4.1 *Materials and methods*

4.1.1 *Computer simulations*

IN order to test the techniques developed in chapter 3, computer simulations were undertaken using custom Matlab (The MathWorks, Natick, MA) routine previously described [80]. These simulations model as closely as possible fluorescence microscopy image time series acquisition. Briefly, one or more populations of particles were assigned random positions in a 2D matrix. For each time step, they were moved according to their pre-set population transport dynamics:

$$\vec{r}_i[t] = \vec{r}_i[t - 1] + \vec{v}\Delta t + \text{randn}\sqrt{2D\Delta t} \hat{x} + \text{randn}\sqrt{2D\Delta t} \hat{y} \quad (4.1)$$

where $\vec{r}_i[t]$ is the position of particle i at time step t , \vec{v} is the population's velocity, Δt the time between two frames, randn is a random number from the normal distribution and D is the population's diffusion coefficient. To simulate microscopy images, these positions were convolved with a 2D Gaussian of e^{-2} radius w_r as an approximation of a confocal optical PSF. Two types of white noise were added to the pixels:

$$I_{noisy}[x, y] = I[x, y] + |\text{randn}| \sigma + \text{randn} \sqrt{I[x, y]} \text{WF} \quad (4.2)$$

where σ is the standard deviation of the *background noise* and WF is the width

factor of the *counting noise*, or *shot noise* of the detection device. For simplicity, we decided to include only the shot noise in our analysis, as they are both white noise sources. The background noise adds an average intensity, which in practice, for real images, is removed by subtracting the mean of an imaged region outside of the cell. To simulate photobleaching, we randomly turned off particles to follow a mono-exponential decay. A list of typical simulation parameters is found in table 4.1.

Symbol	Description	Typical value
Δx	pixel size	0.2 μm
w_r	e^{-2} beam radius	0.4 μm
Δt	time between images	2 s
T	number of images in the time series	120 frames
ρ	particle density	20 part/ μm^2
v	particle velocity	2 $\mu\text{m}/\text{min}$
D	particle diffusion coefficient	0.01 $\mu\text{m}^2/\text{s}$
L	image size	32x32 px ²
WF	width factor of the shot noise	10

Table 4.1: List of variable parameters in the simulator along with their typical values. Parameters that were kept constant for data in this chapter are indicated in bold.

Unless otherwise noted, those parameters were used for the simulations. Those that were kept constant for all simulations presented in this thesis are indicated in bold. Note that we chose the parameters to closely match what we usually have in real cellular image data. For example, we previously imaged and analyzed retrograde flows of adhesion proteins during cell migration with TIRFm using the previous parameters [16]. The velocities recovered were between 1 and 6 $\mu\text{m}/\text{min}$ with median values around 2 $\mu\text{m}/\text{min}$. For each data point shown in this chapter, 32 simulations were run and the results are indicated either as mean \pm standard deviation or as boxplots.

4.1.2 Data analysis

For the IIR filtering, a highpass Butterworth filter was converted numerically through bilinear transformation. The data were then filtered pixel by pixel. The correlation function was computed and we rejected long time lags where the maximum of the

function was of similar amplitude to random fluctuations. A Gaussian was fit for each time lag, and the slope of a linear fit of their positions was used to determine the velocity. To extract the flow density, we used a linear regression on the fitted volume (height times beam area) to obtain the zero lag peak height (as the correlation at $\tau = 0$ can contain other components). This amplitude was normalized by the total amplitude obtained with ICS, to obtain a flow fraction. For biased diffusion, we did a nonlinear fit of the peak amplitudes with equation (2.50).

For the asymmetric analysis, we subtracted the space-time correlation function of the time-reversed data to the normal one. This created a negative peak in the direction of the flow. We then fitted two Gaussians of equal but opposite positions and amplitudes for each time lag. We rejected the first lags where the two peaks were too close to be distinguished and used the same criterion as in IIR filtering to reject the long lags. We then proceeded similarly to the IIR filter to obtain the flow velocity and density. For the diffusion coefficient, we used the slope on the linear fit of the peak width according to equation (2.50).

For the nICS analysis, we use an Hamming window half the time length of the signal. We then averaged the nICS correlation function obtained for three half-overlapping time windows. Two methods were used to obtain the velocity. The default method was to do a nonlinear regression of the whole correlation function with equation (3.10). This equation was convolved in frequencies, according to (2.30), with the Fourier transform of the autocorrelation of the window. The peak amplitude was normalized to the total ICS peak amplitude to extract the flow fraction. An alternative method was used for demonstration purposes. By doing a linear fit on the gradient of the phase angle for each frequency, we could obtain the flow velocity. Since the definition of the complex argument is multivalued (i.e. add or subtract multiples of 2π), the phase had to be “unwrapped” prior to analysis, similar to the procedure done in kICS [74].

Simulations including photobleaching were “detrended” according to the following

references [76, 77]. Briefly, the mean intensity of the images in the time series was fit to a mono-exponential decay. Random numbers were added in each pixel so that the average intensity would stay constant over time.

4.1.3 Tolerances

We decided to set an acceptable relative error of 20 %; what was under 10 % was qualified good. The focus was on accuracy rather than precision since we analyzed small regions and typically many of these can be drawn inside a single cell. Dashed lines were included in the graphs to indicate the acceptable region where the relative error is less than 20 %. Note that this threshold depends mainly on the application and could have been chosen differently.

4.1.4 Boxplots

To compare the different techniques, we expressed the results as side-by-side boxplots [81]. The median is indicated as a target and the edges of the boxes represent the 25th and 75th percentiles. The whiskers extend to the minimum and maximum values obtained excluding outliers, which are indicated as circles if they are more far than 1.5 times the width of the box starting from its end. Side-by-side boxes of different colors represent different analysis of the same condition indicated on the x-axis.

4.2 Butterworth filter

4.2.1 Motivation

In section 3.4, we discussed why the previously developed Fourier filter was flawed; mainly because the cutoff frequency changed with the total sample length. To verify that our Butterworth filter solved this problem, we simulated a configuration of density dominant immobile population along with two flows at low densities ($\{80,10,10\} / \mu m^2$ at $\{0,2,4\} \mu m/min$) while varying the total time series length. The results are shown without filtering, with the standard Fourier filter and for the Butterworth with

$f_c=25$ mHz ($1 \text{ mHz} = 1 \times 10^{-3} \text{ Hz}$) in figure 4.1. As expected, STICS was unable to detect any flow without filtering. The Fourier filter cutoff frequency increases as the total time is decreased, thereby filtering higher frequency component. With this filter, STICS picks up a slow flow for long time series (indicating an incomplete filtering) and something between the two sets values for short time series (indicating immobile filtering and some of the slow mobile). Finally, the IIR filter was set at a value to select only the fast population. It consistently reported the correct velocity for all time series lengths. Two other things are interesting to note here. First, the standard deviation on the velocities obtained with the IIR filter is much smaller as we are not fitting a mixture of populations. Secondly, the Fourier filter tends toward the fast velocity at the shortest time series length. This value is close to the cutoff of the IIR filter ($1/50 \text{ s} = 20 \text{ mHz}$).

4.2.2 Influence of the R ratio

In order to verify our dimensionless analysis of section 3.4 about our IIR filter, we simulated a single population with no noise while changing the R and S ratio. With a baseline of $f_c = 2.5 \text{ mHz}$, $v = 2 \text{ } \mu\text{m}/\text{min}$ and $w_r = 0.4 \text{ } \mu\text{m}$, we changed one of these parameters and plotted the fraction of particles remaining after filtering as a function of R in figure 4.2. Here, we used large $128 \times 128 \text{ px}^2$ regions to obtain accurate ICS measurements. As predicted, the effects of filtering depend only on the $R = \pi f_c w_r / v$ ratio. The values agree well with the theoretical equation (3.19). The experimental values are biased higher than the theoretical curve since we fit a simple Gaussian to this correlation function. Therefore, the two negative sidelobes (as seen in figure 3.1) create an apparent greater ‘‘Gaussian amplitude’’. Note also that the values for large R with different PSF size have high standard deviations because at this point the PSF is on the order of the image size.

The same procedure was repeated for filtering a diffusing population (figure 4.3). The $S = 2\pi\nu_c w_r^2 / 4D$ ratio was changed around the base values ($D = 0.01 \text{ } \mu\text{m}^2/\text{s}$,

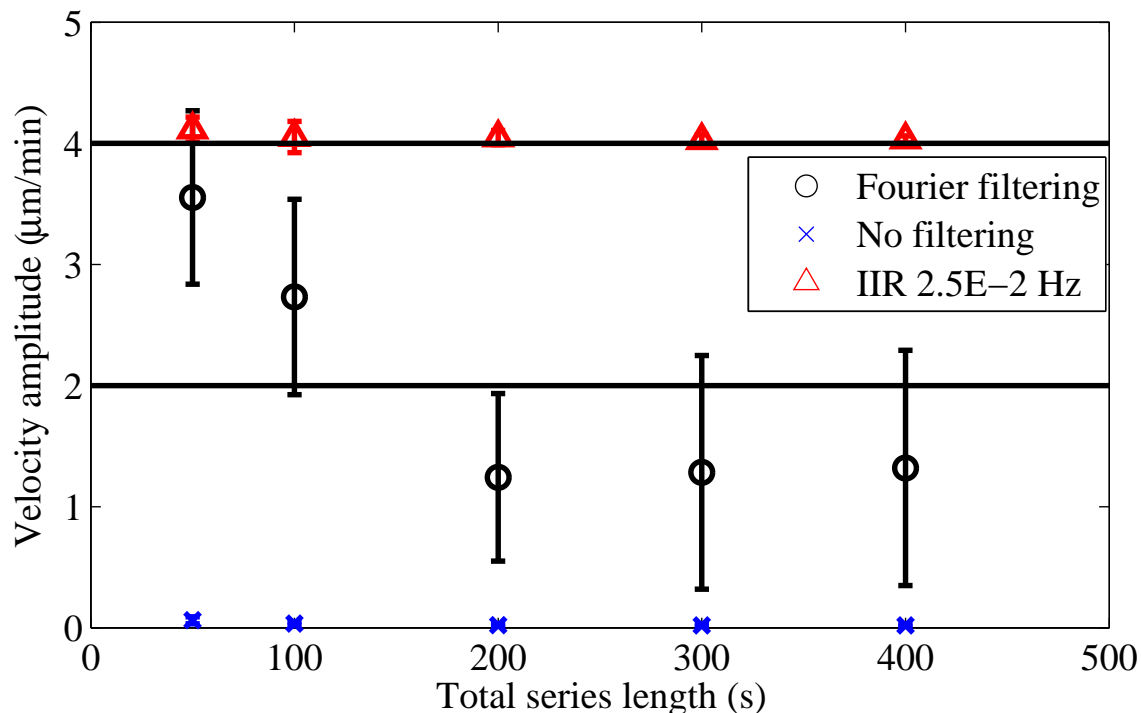


Figure 4.1: Comparison of velocities obtained with STICS without filtering, with Fourier and IIR filter for a mixture of immobile, slow and fast flow particle populations ($\{80,10,10\} / \mu m^2$ at $\{0,2,4\} \mu m/min$). No flow is detectable without filtering (blue cross). The Fourier filter cutoff frequency changes with variation in the time series length. The velocity recovered using the Fourier filter (black circles) is a mixture of the immobile and slow component for long time series, while at short time series it is a mixture of the fast and slow. The IIR filter was set to isolate the fast component at any series length (red triangles).

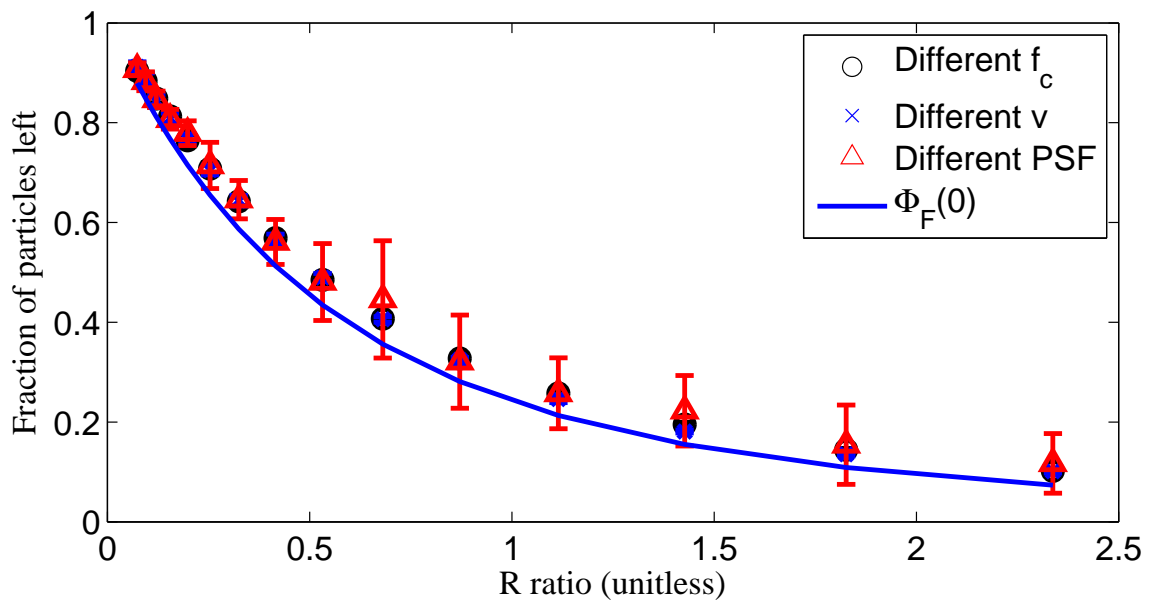


Figure 4.2: Fraction of particles left after applying a Butterworth filter on a flowing population as a function of R . This ratio was changed by varying one of the three parameters ($f_c = 2.5$ mHz, $v = 2 \mu\text{m}/\text{min}$ and $w_r = 0.4 \mu\text{m}$). The effects of filtering a flowing population depends only on R and agrees well with the theoretical equation. The higher bias for the experimental values is caused by the Gaussian fitting, where the negative sidelobes create an higher apparent “Gaussian amplitude”.

$f_c = 2.5$ mHz and $w_r = 0.4$ μm). Again, the experimental values agree well with the theoretical equation (3.20), but show a constant higher bias. This bias is probably due to the negative sidelobes as described previously.

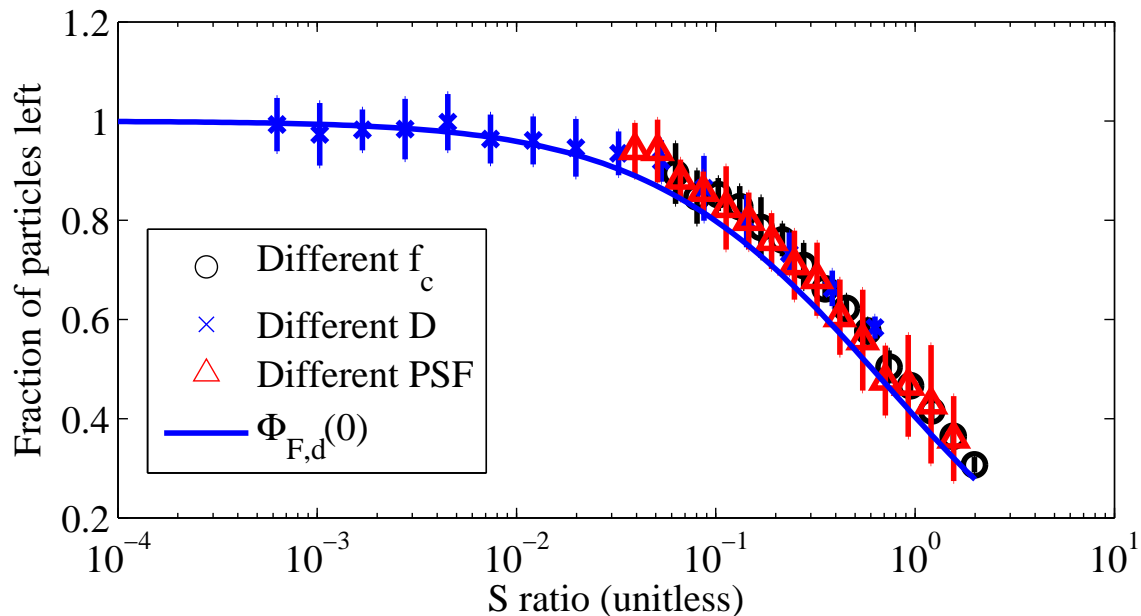


Figure 4.3: Fraction of particles left after applying a Butterworth filter on a diffusing population as a function of S . This ratio was changed by varying one of the three parameters ($D = 0.01 \mu\text{m}^2/\text{s}$, $f_c = 2.5$ mHz and $w_r = 0.4$ μm). The effects of filtering a diffusing population depend only on S and agrees well with the theoretical equation. The higher bias for the experimental values is probably again caused by the Gaussian fitting as in figure 4.3

4.2.3 Distortion of the velocity recovered

The previous simulations verified our dimensionless analysis for the correlation peak amplitude, but did not say much about the shape of the peak. In section 3.4.1, we hypothesized that those changes would not affect the velocity recovered using STICS, as the changes were minimal and in STICS we are interested mainly in the centroid position of the correlation function. To verify this, we simulated an IIR filtered flow for different R ratios without noise to extract the component intrinsic to the filter. As previously, the ratio was changed by varying one of the three parameters ($f_c = 2.5$

mHz, $v = 2 \mu\text{m}/\text{min}$ and $w_r = 0.4 \mu\text{m}$). The results in figure 4.4 show that the filter did not distort the velocity recovered except for two extreme conditions. First, when the PSF was of similar size as the window of analysis (high R), the velocities had a lower bias. This is probably due to effects external to the filter, such as edge effects. Second, as the velocity got very small (around one pixel displacement during the whole time series), the velocities recovered had a higher bias. This is also probably due to an external effect, such as rounding error on the particle's position.

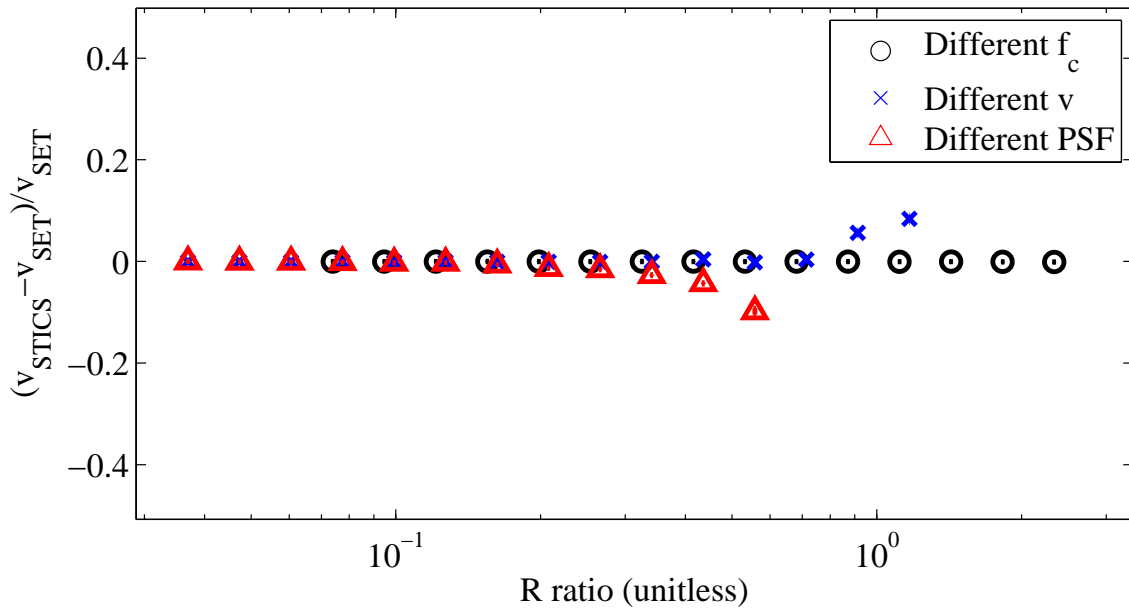


Figure 4.4: Plot of the relative error on the velocity recovered using STICS after IIR filtering as a function of R . This ratio was changed by varying one of the three parameters ($f_c = 2.5 \text{ mHz}$, $v = 2 \mu\text{m}/\text{min}$ and $w_r = 0.4 \mu\text{m}$). There is no bias on the velocity recovered, except when the PSF is of similar size as the region of analysis or when the velocity is very small (around 1 px displacement during the whole time series).

4.3 *nICS*

4.3.1 *Analysis example*

Equation (3.10), which describes a flow in *nICS*, is not very telling. To show the potential strengths of the technique, we simulated a 64×64 px² region with high noise (WF=10), 50 % immobile and slow flow ($v = 2 \mu\text{m}/\text{min}$) populations and analyzed the resulting image series with *nICS* as described in 4.1.2. Two slices of the imaginary part of the correlation function are shown in figure 4.5. Let's take a moment to understand how equation (3.10) modulates the correlation function. The first exponential term is a Gaussian in ν depending on the particle's velocity. The faster the particles, the farther they will extend in the high frequencies. Moreover, as the immobile fraction is concentrated in the $\nu = 0$ plane, the decay of the flow will be visible. The second exponential is a 2D coupled Gaussian which limits the decay along the axis of the flow. Finally, the third term modulates the decay as a sine wave, with a period depending on the ν/v ratio. The imaginary part (sin) is asymmetric and, therefore, indicates the direction of the flow. This can all be nicely seen in figure 4.5, even for these difficult analysis conditions. A nonlinear fit can extract the particles velocity, direction and density. This fitting procedure will be characterized in detail in section 4.5.

4.3.2 *Windowing bias*

In section 3.1.1, we explained that the bias in *kICS* was probably due to the fact that the convolution with the Fourier transform of the window was neglected in the analysis. We will show here that a similar effect is present in *nICS* for this exact reason. In figure 4.6, we extracted the velocity of a flow both by nonlinear regression and by using the phase angle (similarly to *kICS*) for different window lengths. The nonlinear fit included the convolution but this effect was neglected in the phase angle procedure. A positive bias is clearly visible for the latter, starting from around 10 % at 60 frames up to almost 250 % at a window size of 10 frames. However, the

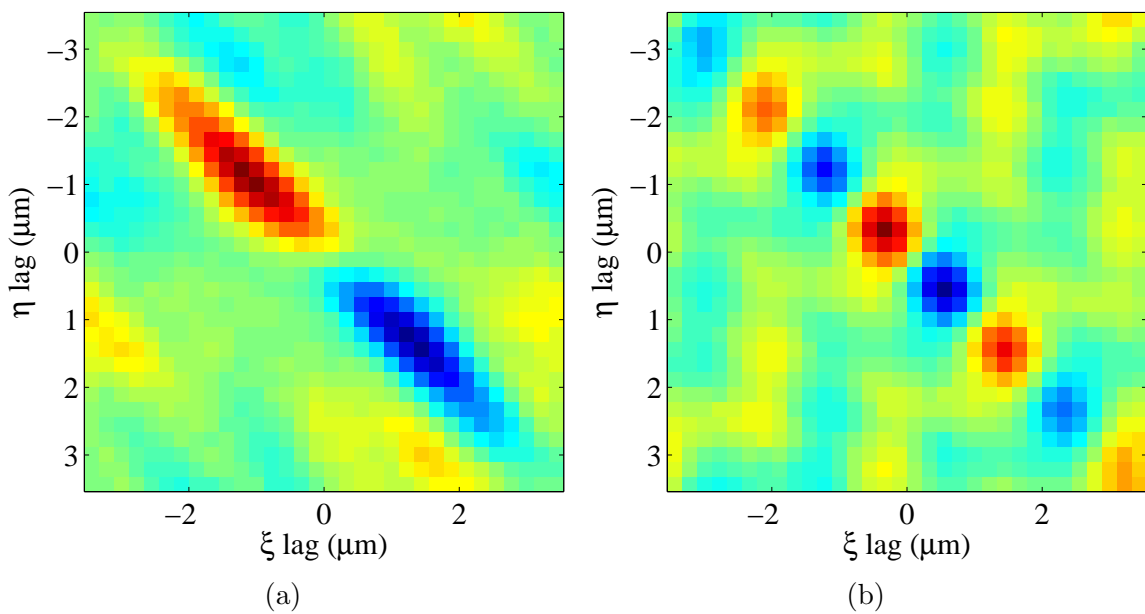


Figure 4.5: Two slices of the nICS correlation function are shown for different frequencies ($\nu = 10$ and 39 mHz for a) and b) respectively). The correlation function decays as ν increases and as the spatial lags increase. The slow decay axis corresponds to the flow and the first positive peak (red) indicates the direction. The simulation parameters can be found in the text.

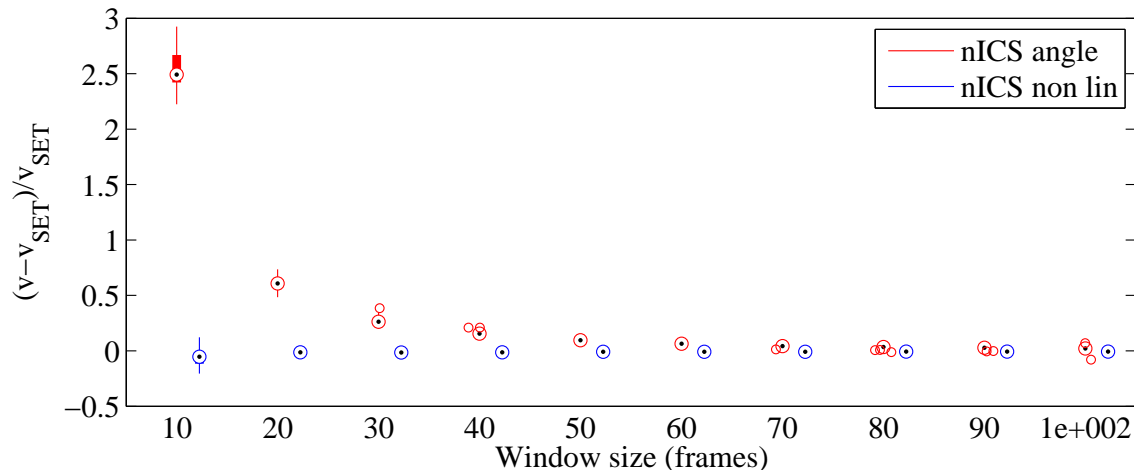


Figure 4.6: Relative error in flow velocity recovered using nICS as a function of the time window length with the angle of the phase (no convolution) and with a full nonlinear fit (including the convolution with the window). As the window gets shorter than 60 frames, the approximation of no convolution is no longer valid and a significant bias appears. The nonlinear fit is less precise at a window length of 10, but still accurate.

nonlinear fit remains accurate for all of the window sizes tested, but starts to be a little less precise around 10 frames. The exact methodology is described in more detail in the Materials and Methods section (4.1).

We see that for nICS, neglecting the convolution results in a biased higher velocity. In kICS, the same approximation resulted in a lower diffusion. We can explain those differences by looking at the effect of the convolution. As a first approximation, the convolution results in a spreading of the correlation function over the dimension of convolution. In nICS, the window is in the temporal frequency space, thereby producing a correlation function that decays more slowly over ν . This results in an apparent higher velocity (faster velocities decay more slowly in ν -space). On the other hand, the windowing and convolution is over space in kICS. This creates an bigger apparent PSF, resulting in a slower apparent diffusion. We conclude the section by noting that the nonlinear regression has proven to be robust, accurate, precise and relatively fast (a few seconds). Consequently, we decided to include only this method

in the comparison of new techniques.

4.4 *knICS*

4.4.1 *Analysis example*

A particularly interesting feature of *knICS* is its ability to separate different dynamics in different planes. To illustrate this, we simulated a $\{10,10,20,80\}$ particles/ μm^2 with $\{2,6,0,0\}$ $\mu\text{m}/\text{min}$ flow and $\{0,0,0.01,0\}$ $\mu\text{m}^2/\text{s}$ diffusion. The diffusion coefficient was chosen to be on the same scale as the slow flow. The region was 64×64 px² and the window $32 \times 32 \times 60$ (x,y,t) points. The result is shown in figure 4.7, where an 3D isosurface demonstrates all the different components. The immobile component is concentrated on the $\nu = 0$ axis along with the slow diffusion, which thickens a little bit the plane. The two flows are represented by planes, where the normal vectors indicate the direction of the flow. The fastest population is the one that extends farther in the high temporal frequencies. While this technique can be very useful to identify different components visually, in practice the equations developed in section 3.2 have proven very difficult to fit. This is probably due, at least in part, to the convolution with the window function both in space and time. Therefore, this technique will not be included in the techniques comparison.

4.5 *Comparison of new techniques*

In this thesis, we have developed multiple correlation techniques with the goal of obtaining greater insight about the dynamics of fluorescently labeled proteins in cells. To see how far these techniques can bring us, we characterized them in simulations. We chose to compare the IIR filter, the asymmetric analysis and *nICS* which can extract the flow density, velocity and angle. To discover their strengths and limitations, we simulated different fractions of immobile particles and signal-to-noise ratios. Also, since correlation techniques in general are not affected by white noise (except in the

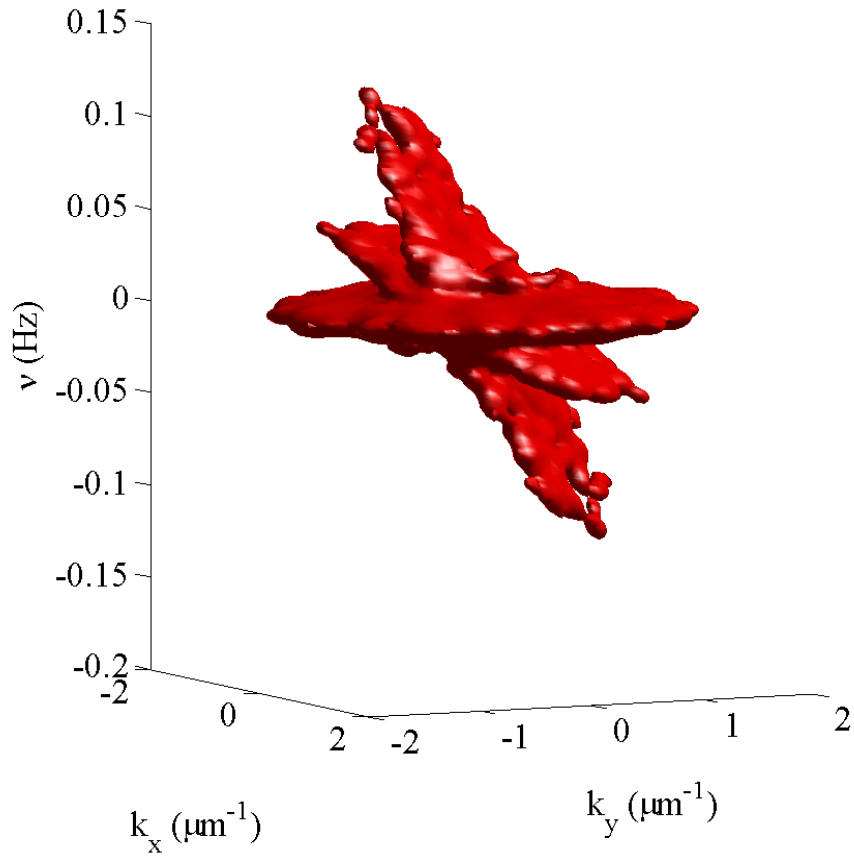


Figure 4.7: 3D isosurface of a knICS correlation function for multiple populations. The immobile component is concentrated on the $\nu = 0$ axis along with the slow diffusion, which thickens a little bit the plane. The two flows are represented by planes, where vectors normal to their surfaces indicate the direction of the flow. The fastest population is the one that extends farther in the high temporal frequencies. Simulation parameters are described in the text.

zero lags values), we simulated correlated noise as a very fast diffusing population ($1 \mu\text{m}^2/\text{s}$). This diffusion is too fast to be resolved at our image frame time scale, but add spurious noise in the correlation function. Finally, we chose simulation parameters that represent the challenging conditions of real data. The region size was $32 \times 32 \text{ px}^2$ for 120 frames and a slow flow of $2 \mu\text{m}/\text{min}$. The basic set parameters were a high noise of $\text{WF}=10$ and an immobile population of 50 %. This gives a signal-to-noise ratio (SNR), as traditionally defined as the average intensity over the standard deviation of the noise, of around 2. A typical region of analysis is shown in figure 4.8. For the analysis parameters, the cutoff frequency of the IIR filter was set to 2.5 mHz ($R=0.1$).

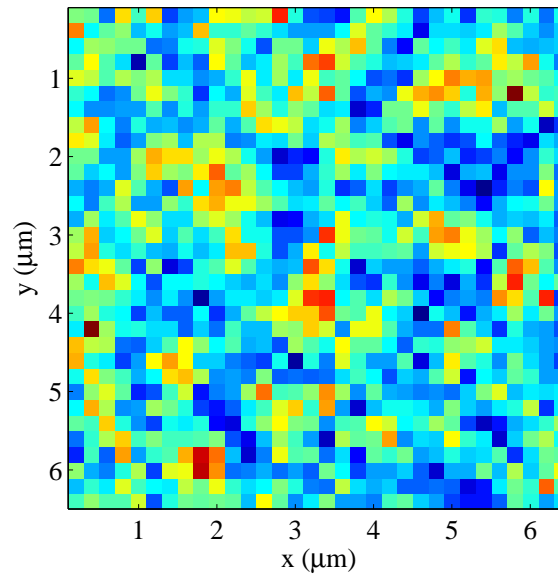


Figure 4.8: A typical simulated region of fluorescent particles. The region size is $32 \times 32 \text{ px}^2$ and the width factor of the noise is set at 10, making a signal-to-noise ratio of around 2. The total density was set at $20 \text{ part}/\mu\text{m}^2$

4.5.1 Immobile density

We first compared the techniques for simulations with an immobile fraction between 10 and 90 %, as shown in the boxplots of figure 4.9. Under these conditions, the techniques behave quite similarly. First, the flowing population density (f) recovered

for all techniques was rather imprecise. Effectively, the density recovered is essentially two ICS measurements, one for the correlation peak height and one for the normalization. Moreover, ICS is very imprecise under these conditions (small region size and high noise). However, we can still recover more or less accurately the flowing population density for all conditions with all techniques. At more than 50 % immobile, the recovered density start to be less precise. nICS is accurate over the complete range, as the two other techniques are biased higher, probably due to leaking of the immobile component. In general, the IIR was the most precise and nICS the most accurate.

As for the velocities recovered, they were very accurate for all the conditions. This shows that the immobile population concentration did not significantly perturb these analysis methods. For example, one could simply take a higher filter frequency for the IIR analysis to remove more immobile. The question is: how much of your signal are you ready to lose to filter the immobile fraction? This depends on the amount of noise present in the data, and the next sections will investigate this question.

4.5.2 *Signal-to-noise*

We investigated the effects of white noise on our analysis in figure 4.10. We increased the amount of the shot noise width factor (WF) from one (Poisson distribution) to up to 20. At this level, the SNR was around 1. The results were similar to those described in the previous section, where the densities recovered were rather accurate and the velocities very accurate and precise. As expected, the effects of white noise on correlation analysis are minimal.

4.5.3 *Diffusing population*

In real data, there may frequently exist particle dynamics faster than the image frame acquisition timescale typically employed (such as cytoplasmic proteins diffusing in the cell). This fast diffusion will not be seen in the correlation, but will produce spurious peaks and add a “background” noise in the function. To simulate this effect, we

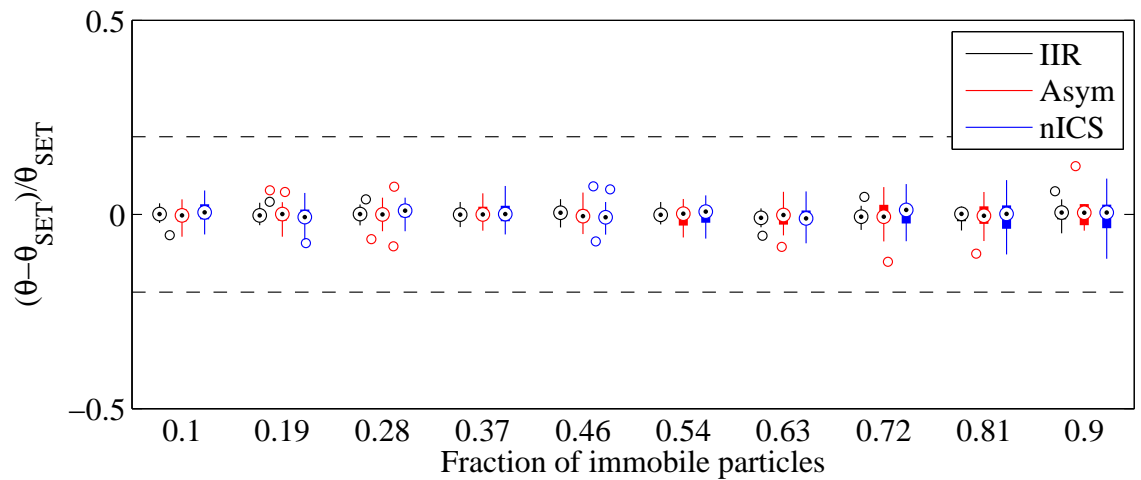
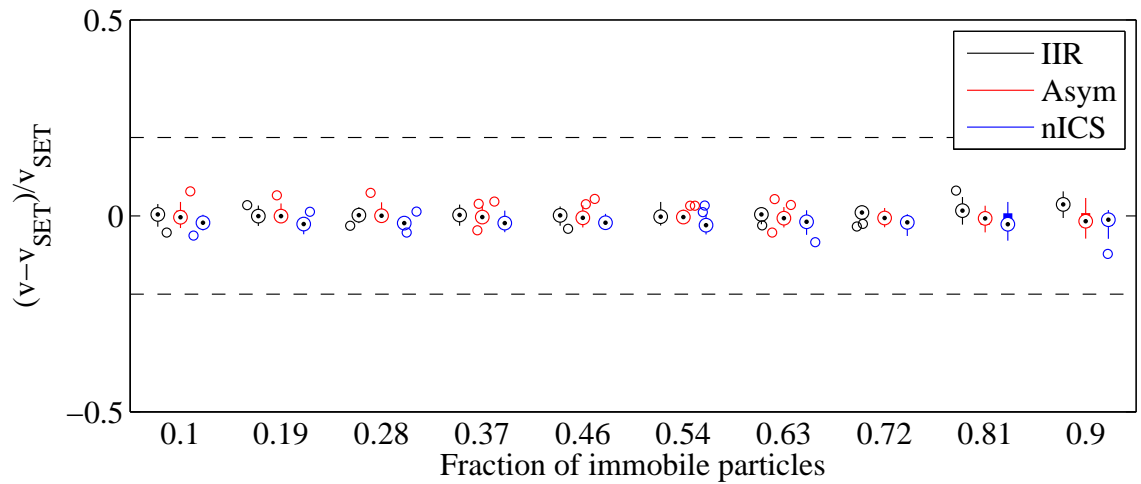
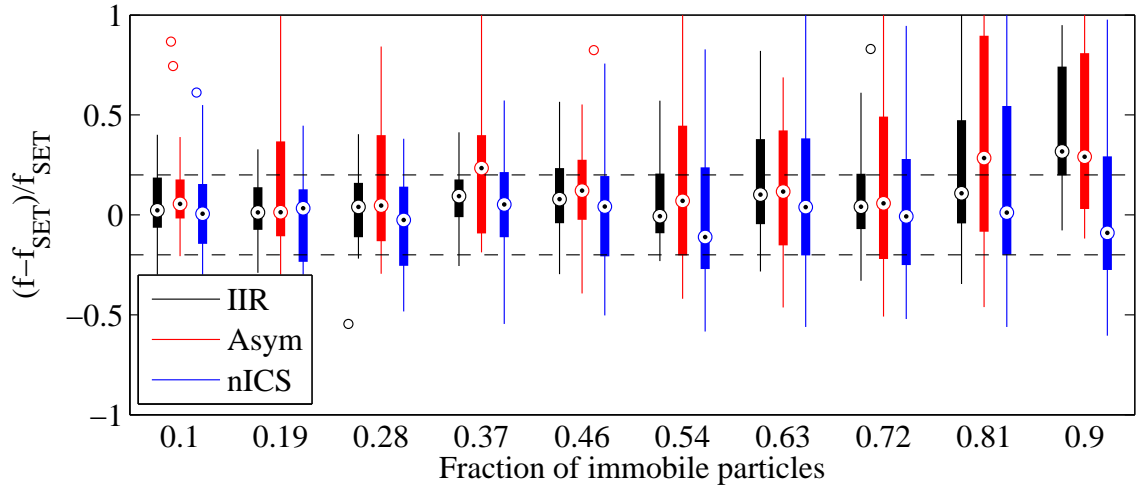


Figure 4.9: Accuracy and precision comparison of new techniques for different densities of immobile particles.

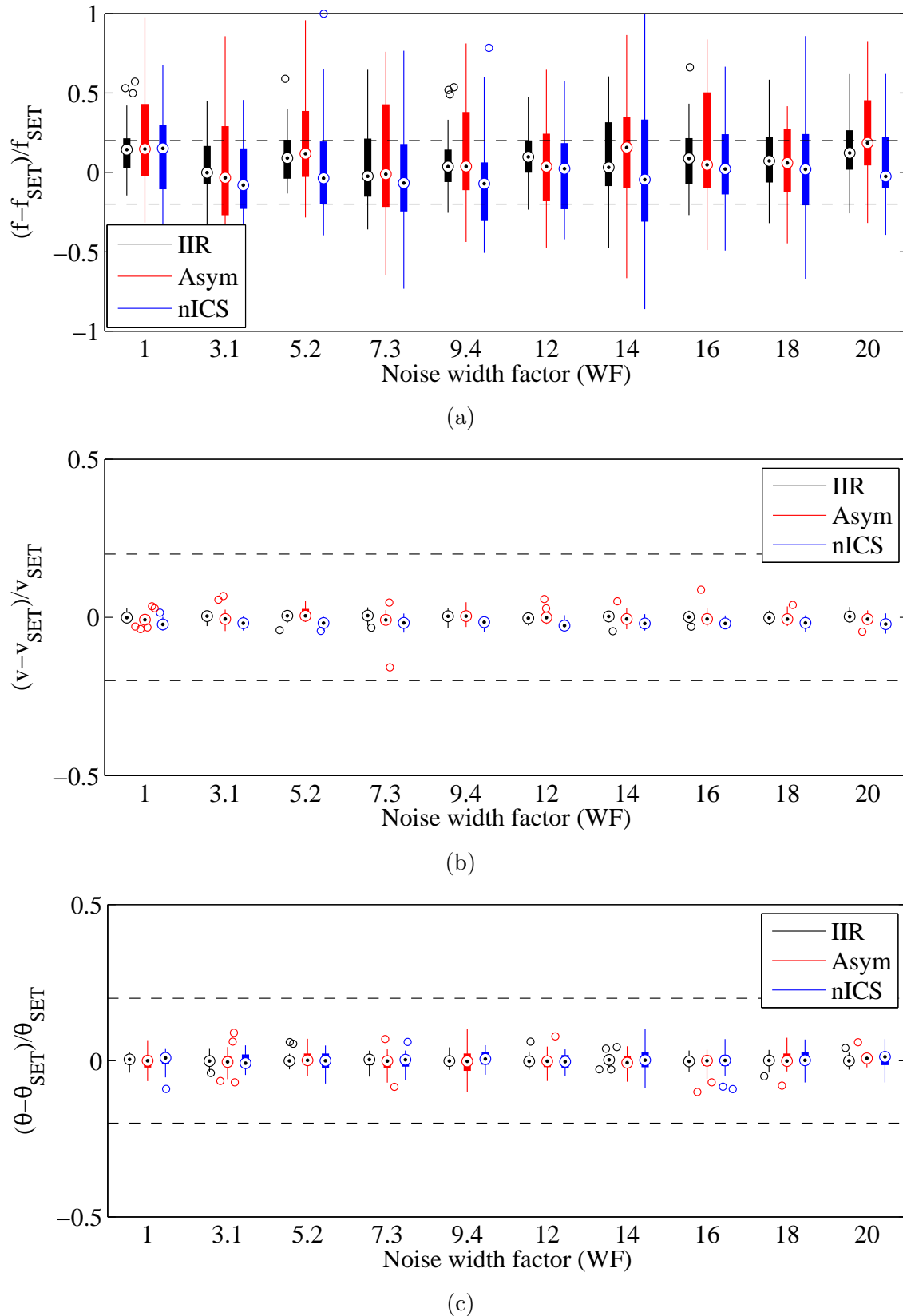


Figure 4.10: Accuracy and precision comparison of new techniques for different amounts of noise.

separated the background population in two groups: 50% were immobile and 50% had a very fast diffusion relative to the timescale of analysis ($1 \mu\text{m}^2/\text{s}$). The results are shown in figure 4.11. Note that we used the fraction of mobile particles as the x axis to distinguish the graphs from the previous ones. For the IIR filter and the nICS analysis, the results are similar to the previous sections. However, for the asymmetric analysis, as the mobile fraction is lower than 50 %, the nonlinear fit starts failing sporadically. As the fraction reaches 10 %, it never fits successfully. The effects of spurious peaks are probably amplified by the asymmetry analysis. However, it is interesting to note that even as a large fraction of the fits fail, those that converge are still accurate and precise. This suggests that there might be a way to tweak the fit to achieve better performance.

4.6 Biased diffusion

Section 4.5 explored the limits of the newly developed techniques tested under different challenging conditions. However, the accuracy and precision of the extracted velocities still seems artificially good. Meanwhile, one could think that a simple flow is an unrealistic biological model. Effectively, due to the stochastic nature at the molecular level in the low Reynolds number sub-cellular environment, biological transports are probably never perfect or pure. They can be more reasonably modeled as biased diffusion. This section will explore how this biased diffusion influences the analysis.

4.6.1 Bias coefficient

It is important to recall the dimensionless analysis of section 3.4.1 for this problem. We saw that a diffusion and a flow were of comparable time scale if $4D/w_r^2 = v/w_r$. Therefore, we define here a *bias coefficient*, $B = vw_r/4D$, so that it is close to one when the two processes are similar. As this coefficient gets larger, the biased diffusion will become a pure flow. Similarly, if B is close to zero, the particle will behave as if

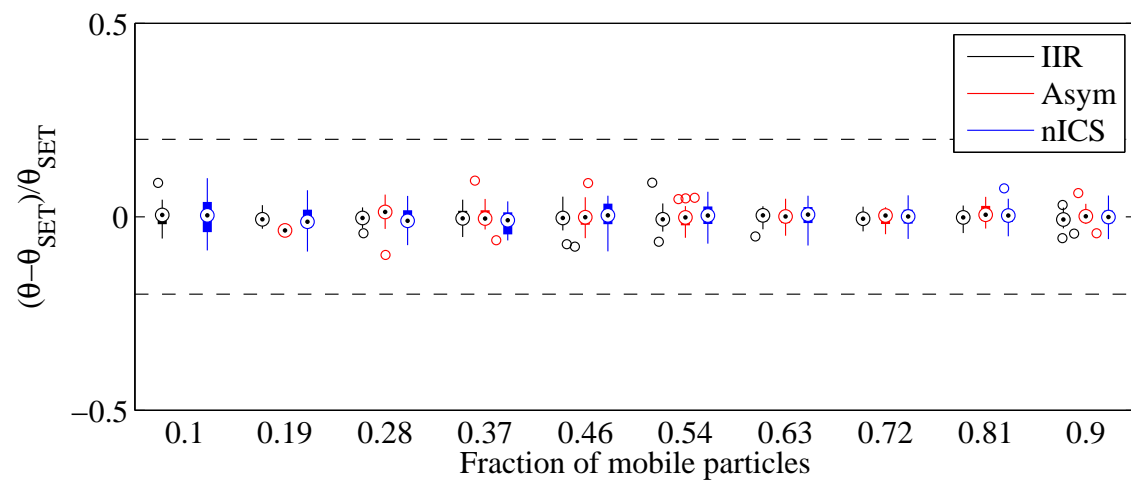
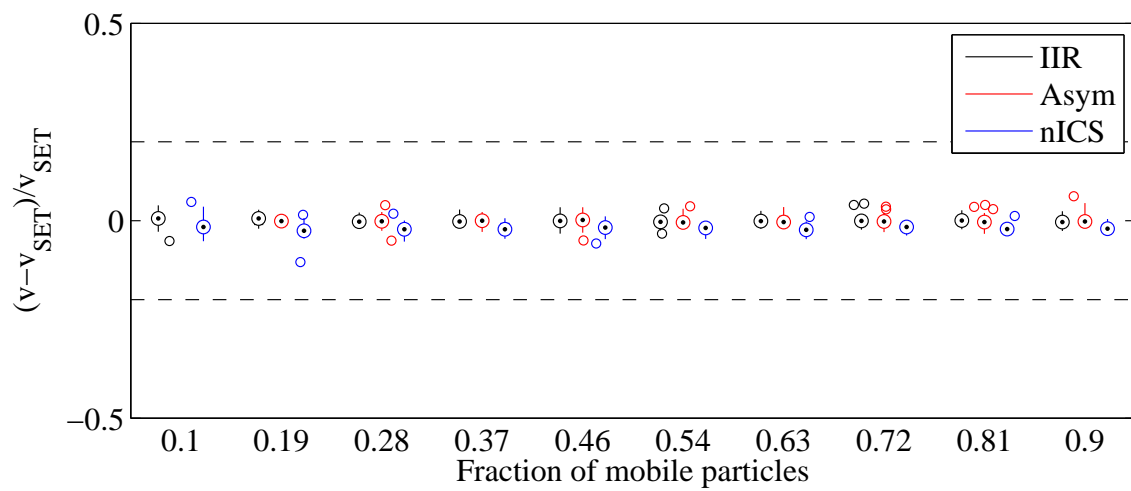
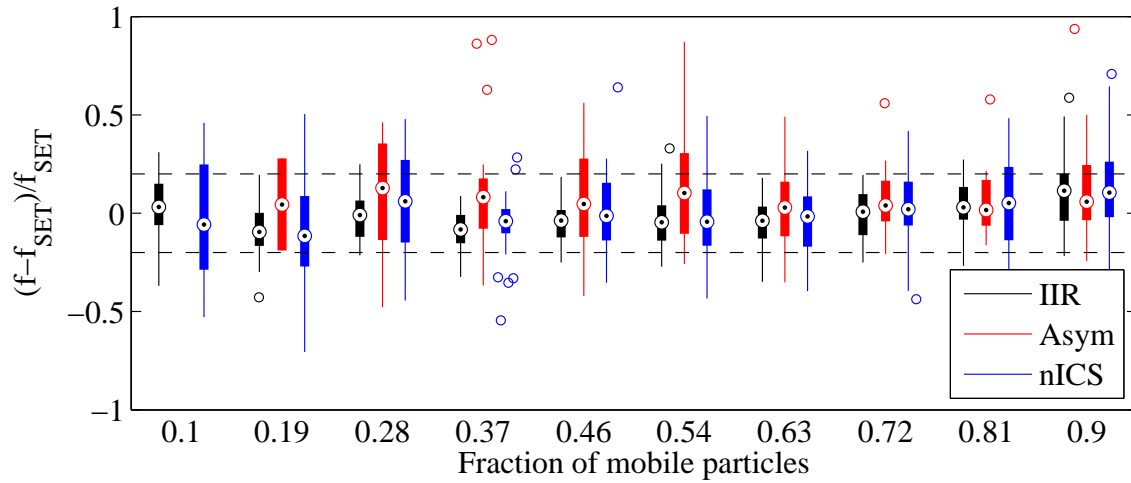


Figure 4.11: Accuracy and precision comparison of new techniques for different densities of immobile and diffusing particles.

it were pure diffusion.

We compared the new techniques against the bias coefficient and the results can be seen in figure 4.12. A lot of information can be found in these graphs. First, we see that the generally all techniques start failing when the coefficient is close to 0.2. For the fitted density, it is interesting to see that the IIR is accurate almost all the way down to $B = 0.01$. As for the two other techniques, they both get slowly biased towards zero. For nICS, this is probably because we are fitting a simple flow and the shape of the correlation function is different for a biased diffusion. For the velocities, all of the techniques start diverging around 0.6. Note that the x-axis scale is logarithmic.

For the asymmetric and IIR analysis, we were also able to fit a diffusion coefficient, potentially yielding more information about the biological process. These results are shown in figure 4.13. Generally, the fit is very approximate and only the order of magnitude of the diffusion coefficient could be obtained for a B between 0.2 and 5. Lower than that, the techniques failed as discussed previously. Higher than that, the diffusion coefficient was simply too low to be evaluated with the techniques. It is interesting to see that the two techniques have an opposite bias. Effectively, we used different techniques in IIR and asymmetric analysis to extract the diffusion coefficient. With the IIR filter, the shape of the correlation function is distorted. We therefore used the peak decay to obtain the diffusion coefficient. With the asymmetric analysis, the amplitude of the correlation function is very unreliable as in the low lags, the positive and negative flow cancel themselves. For that technique, we used the widening of the correlation peak to extract the diffusion coefficient. Those two methods seem to produce more or less equal but opposite bias. This is why we created a third category which averages the two. The combined values were accurate and generally more precise in the interesting range (0.2-5).

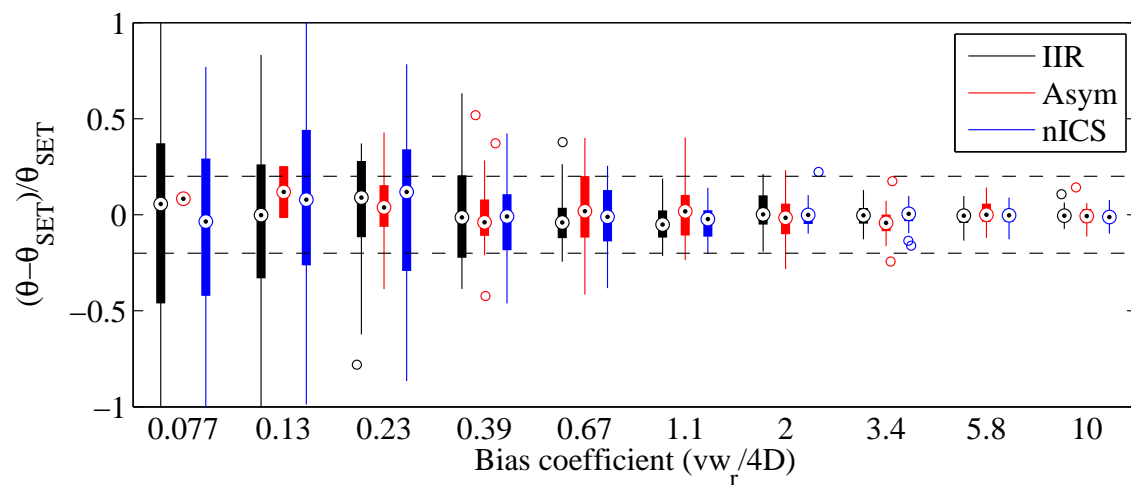
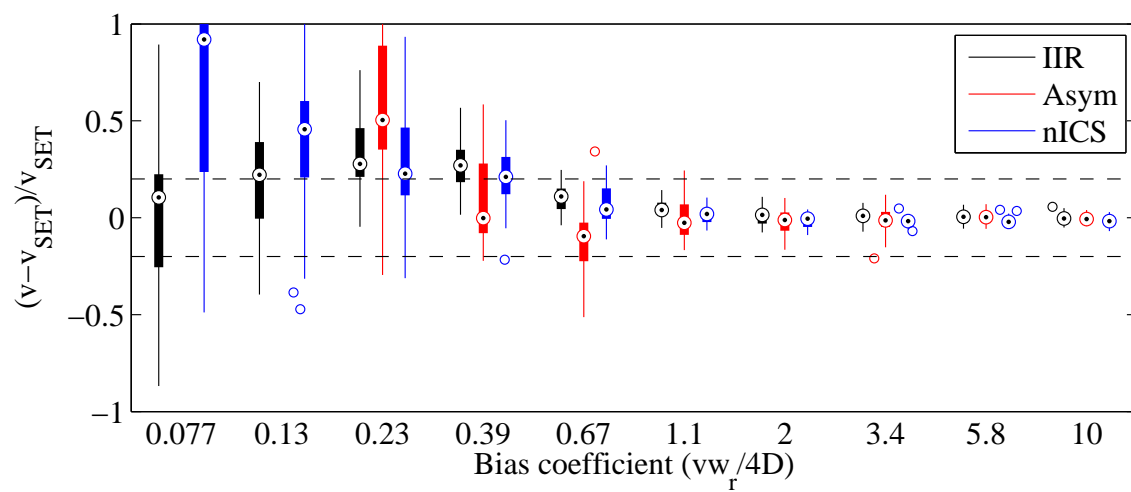
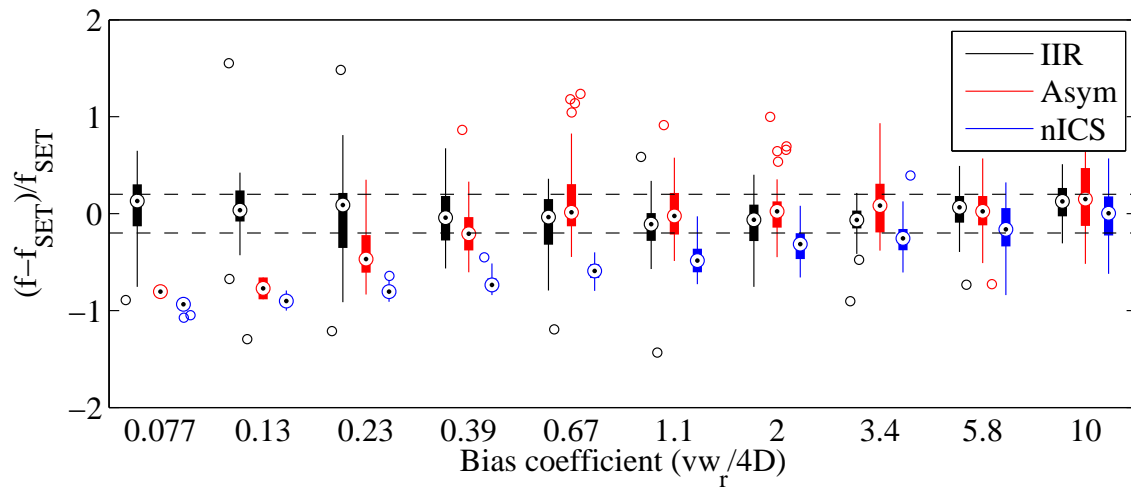


Figure 4.12: Accuracy and precision comparison of new techniques for measuring biased diffusion

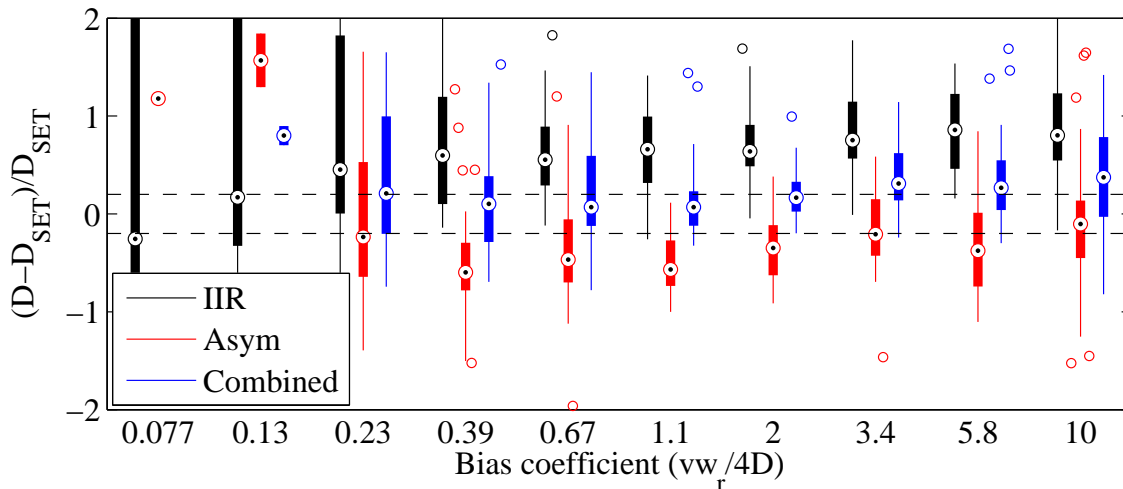


Figure 4.13: Accuracy and precision comparison of new techniques for measuring biased diffusion

4.6.2 Limits

Biased diffusion seems to be a challenging limit for extracting molecular transport. Effectively, the correlation function decays much more quickly and is prone to spurious movements. However, it is a more realistic biological model and the correlation functions obtained more closely resemble real data. Therefore, we repeated all the simulation of section 4.5 for a biased diffusion. We set the diffusion coefficient to $0.005 \mu\text{m}^2/\text{s}$, to obtain a B close to one. The results are shown in figures 4.14-4.17. Let's briefly summarize the important results. For an increasing fraction of immobile particles, most techniques work up to a fraction of 0.7, but the results start to be less precise around 0.5. Measurement of the flow density is more precise with nICS, but it also very biased as we discussed earlier. The asymmetric fit is the least precise, but generally accurate. The IIR filter is somewhere between the two, but starts diverging earlier than was the case for a simple flow (comparing to figure 4.9). This is probably due to the fact that a particle undergoing biased diffusion will be filtered as a flow and as a diffusion (i.e. doubly filtered). Therefore, this population will be more filtered compared to the immobile fraction. The immobile population will thus have a greater

influence on the analysis than in the case of simple flow. For this reason, it would be necessary to use a higher cutoff frequency for large fraction of immobile particles. The filtering limits will depend on the SNR and on another effect discussed in the following paragraph.

Measurement of the velocity is generally limited in the same conditions than the density. All techniques start diverging at a immobile fraction of around 0.7. However, there is an interesting effect worth discussing. The IIR filter shows a higher bias until the immobile fraction gets mixed with the flow. This is due to the fact that for a biased diffusion, the correlation function will spread as well as move for increasing time lags. This creates an apparent spread in velocities in the direction of the flow. Effectively, a Gaussian distribution of flow speeds would spread the correlation function in the direction of the flow similarly (without the widening in the perpendicular direction). Therefore, the filter will remove more the low “apparent velocity” than the fast ones. This distorts the correlation function, pushing the centroid of the peak in the direction of the flow and creating a higher velocity. Biased diffusion therefore puts another, and potentially more important limit on how much filtering can be undertaken. Not only are we losing signal as we filter more, but we are distorting the shape of the correlation function. This was often seen in real cellular data, where filtering more results in higher measured velocities (Potvin-Trottier, L. and Guillet, D., unpublished observation). This effect is not present in the asymmetric analysis, since without frequency filtering the centroid of the correlation peak still reports the right velocity. Note also that the angle fitting is also much less precise than for the pure flow.

The effects of noise were again shown to be very limited. It is interesting to note that increasing the noise until the SNR was around one did not significantly change the precision of the techniques. This reinforces our conclusion from the previous analysis that noise is not a very important factor in correlation analysis. Simulating a background diffusing population produced similar results for the IIR and nICS analysis than only an immobile one. However, the asymmetric analysis started failing

earlier, with a fraction of mobile particles around 20 %.

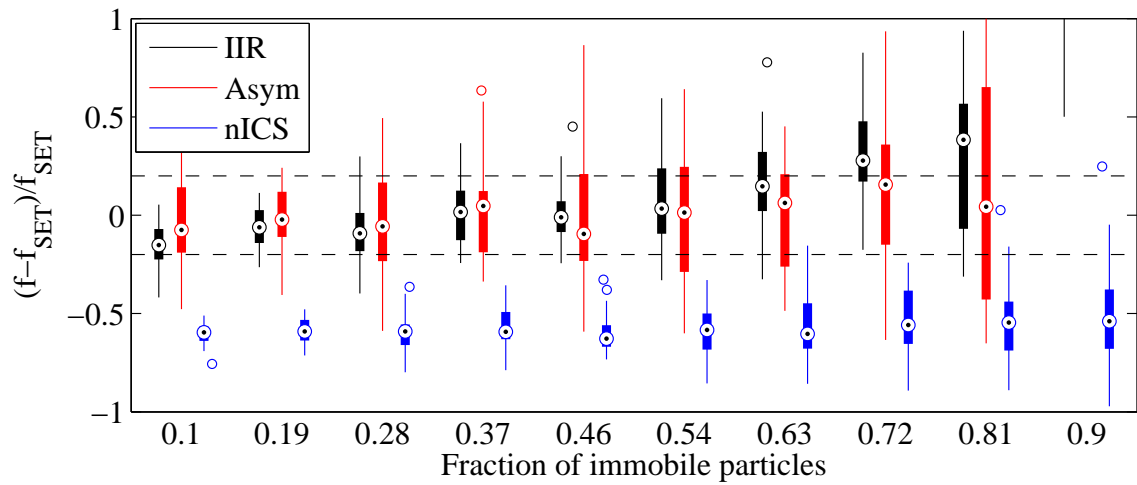
Finally, the diffusion coefficients measured which are shown in figure 4.17, were rather precise and quite accurate when combining asymmetric and IIR analysis, due to the interesting equal but opposite bias. Thus, this methodology is limited by the convergence of the asymmetric analysis, which is less robust for the simulation conditions described previously. These results suggests that a biased diffusion coefficient could be measured as long as the asymmetric analysis converges.

4.6.3 Photobleaching

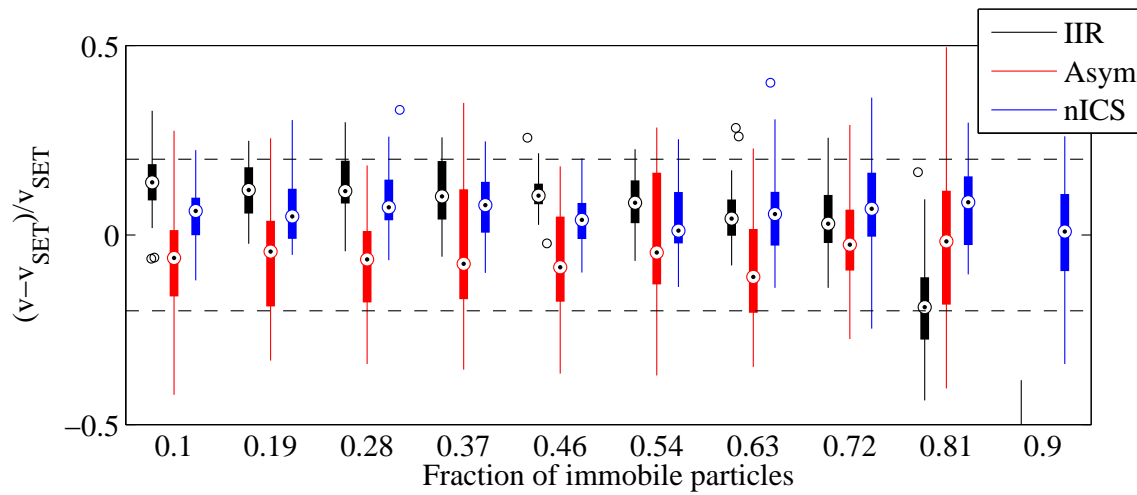
As in live-cell imaging some degree of photobleaching is often inevitable, we sought to verify how it affected our analysis. We simulated and corrected photobleaching as described in section 4.1. The results, shown in figures 4.18-4.19, demonstrate that the correction was successful at all of the levels tested. The precision of the techniques gets lower as the fraction of bleached molecules increases, however, the accuracy is still acceptable even at 90% of molecules bleached during the time series, which would be unacceptable for most live-cell imaging. It is not very surprising that the techniques are not sensible to photobleaching, as the correction involves adding uncorrelated random number (i.e. noise), and we already saw that white noise does not affect significantly correlation techniques.

4.7 Summary

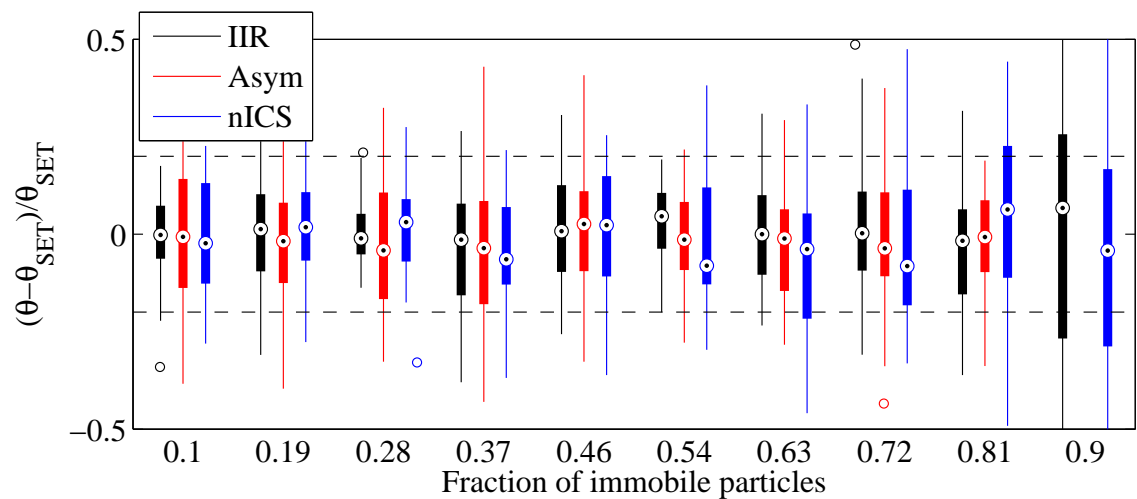
The newly developed techniques were characterized for accuracy and precision using simulations with challenging conditions. We can draw multiple conclusions from this characterization and testing. First of all, white noise does not affect significantly those correlation techniques. Second, the precision on the measured density depends largely on the precision of ICS. Since we analyzed small regions, the precision was not very good due to limited spatial sampling. Since ICS was already characterized in detail elsewhere [80], we did not investigate this further. Thirdly, the immobile fraction



(a)

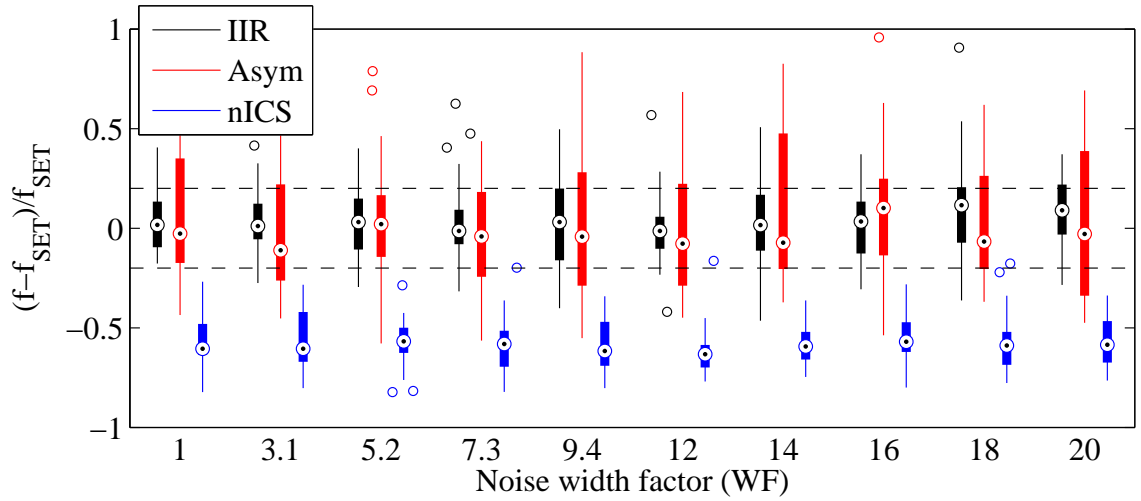


(b)

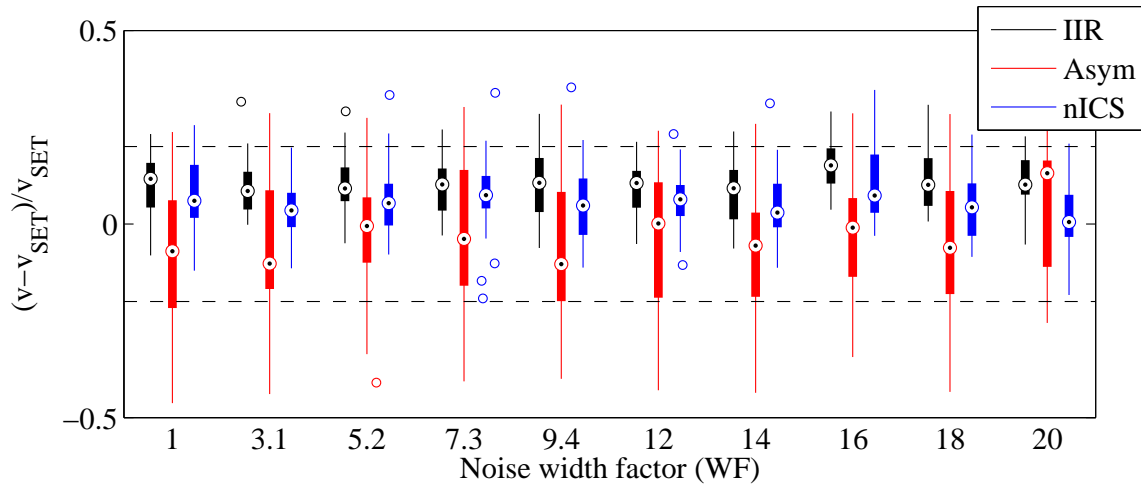


(c)

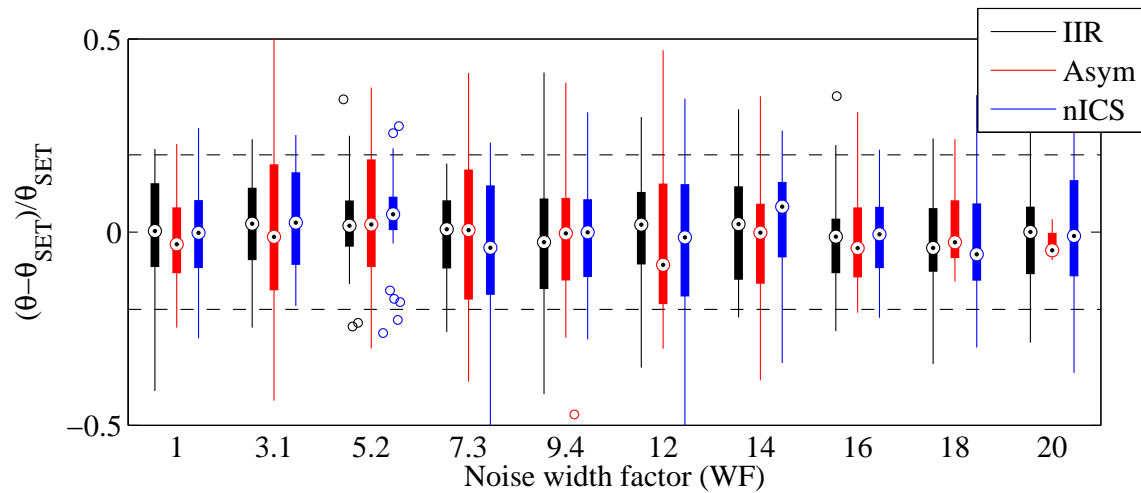
Figure 4.14: Accuracy and precision comparison of new techniques for different densities of immobile particles for a biased diffusion.



(a)



(b)



(c)

Figure 4.15: Accuracy and precision comparison of new techniques for different amounts of noise for a biased diffusion.

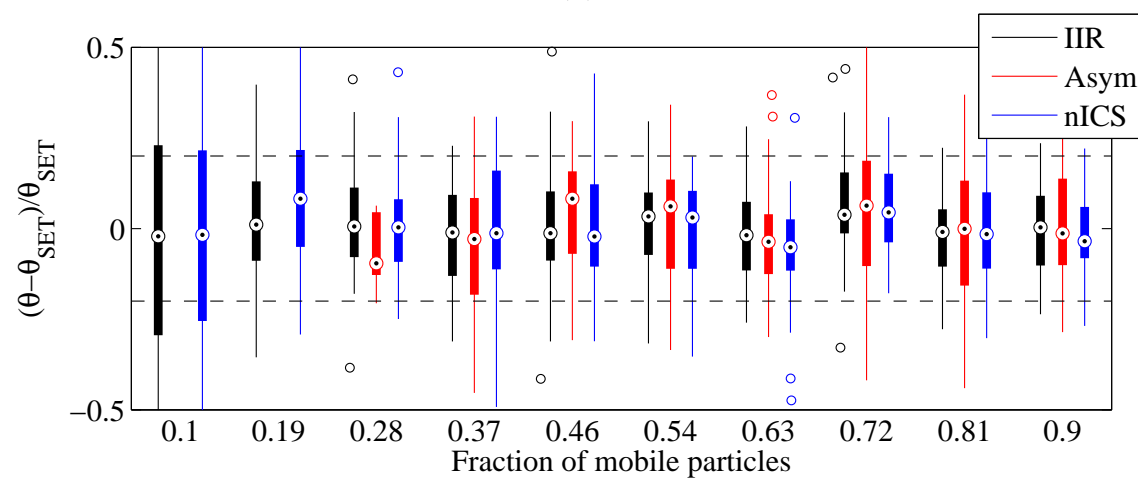
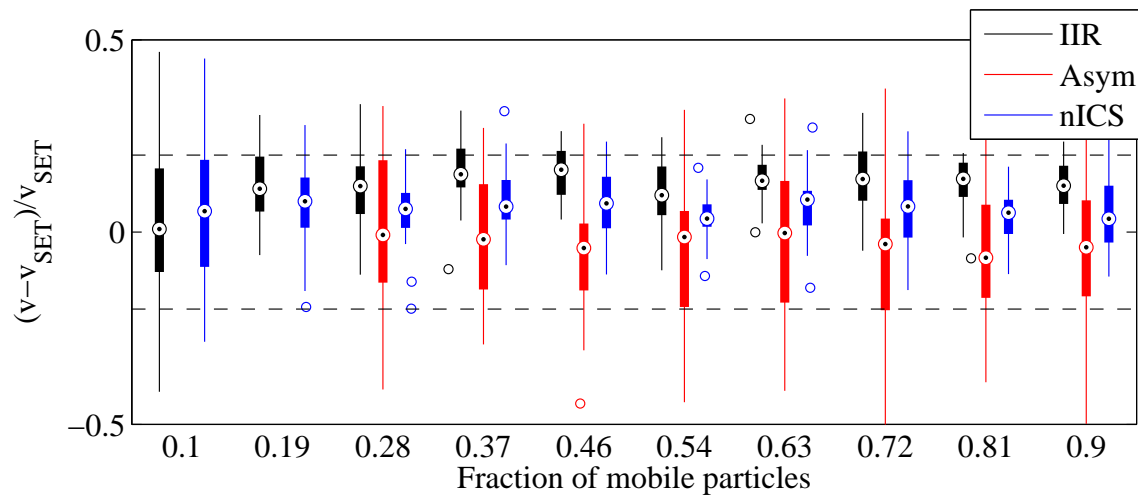
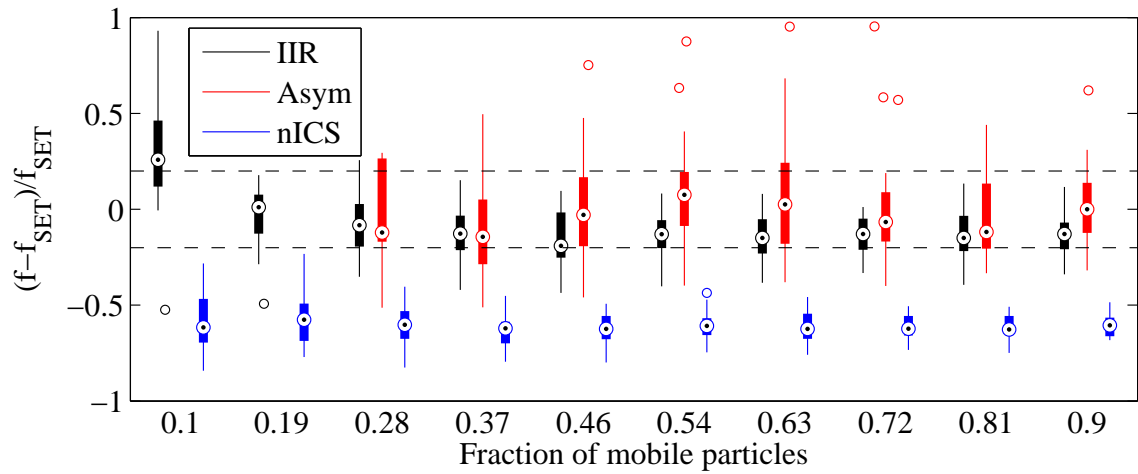
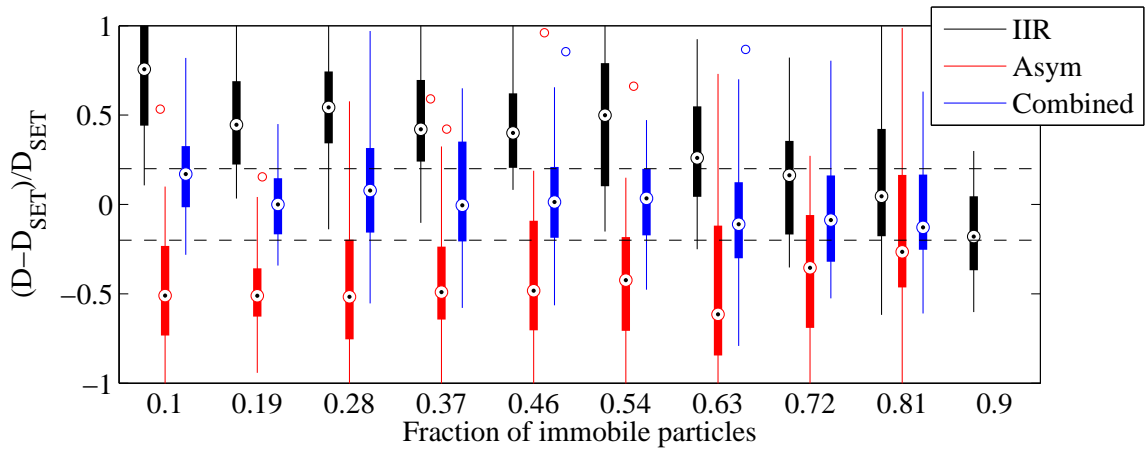
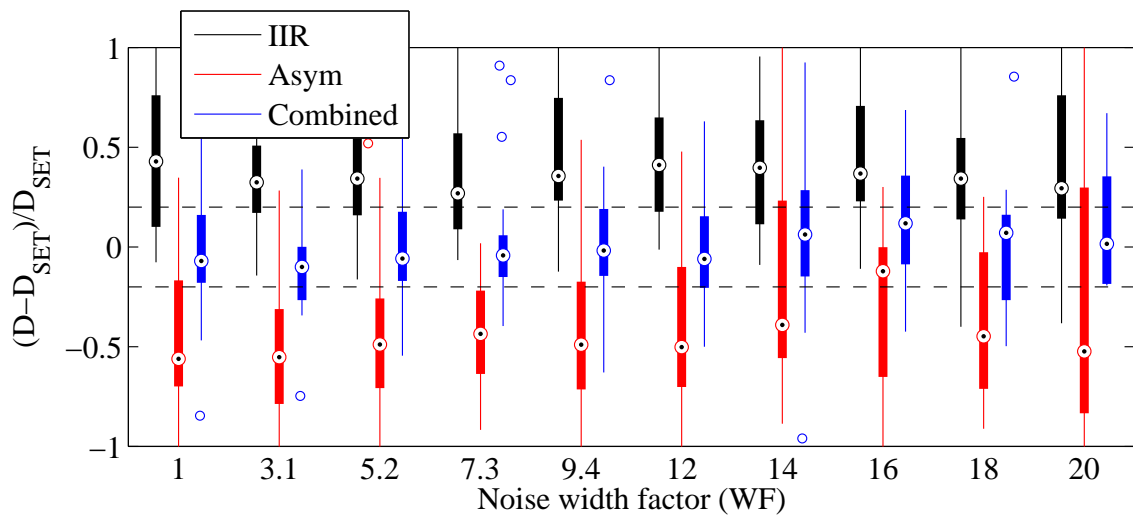


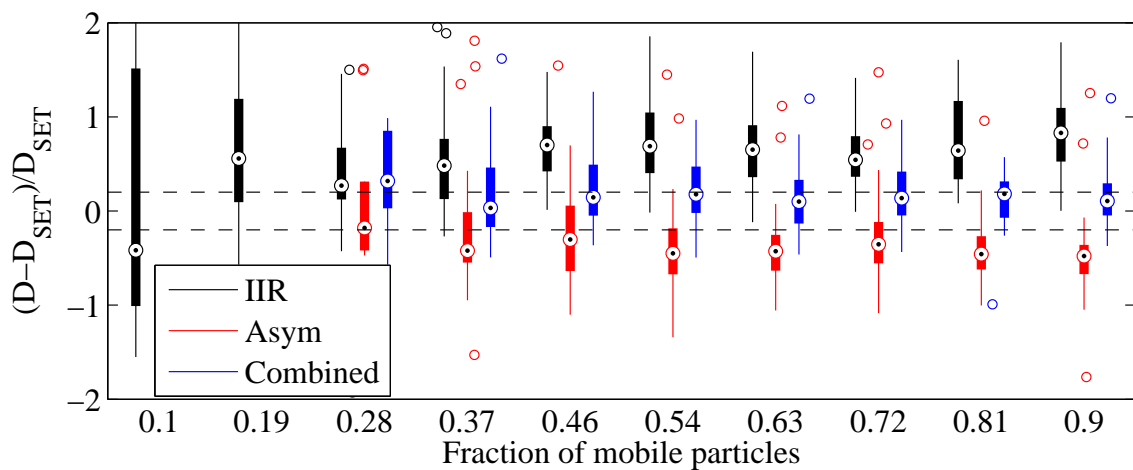
Figure 4.16: Accuracy and precision comparison of new techniques for different densities of immobile and diffusing particles for a biased diffusion.



(a)



(b)



(c)

Figure 4.17: Accuracy and precision comparison of new techniques for measuring the diffusion coefficient of a biased diffusion.

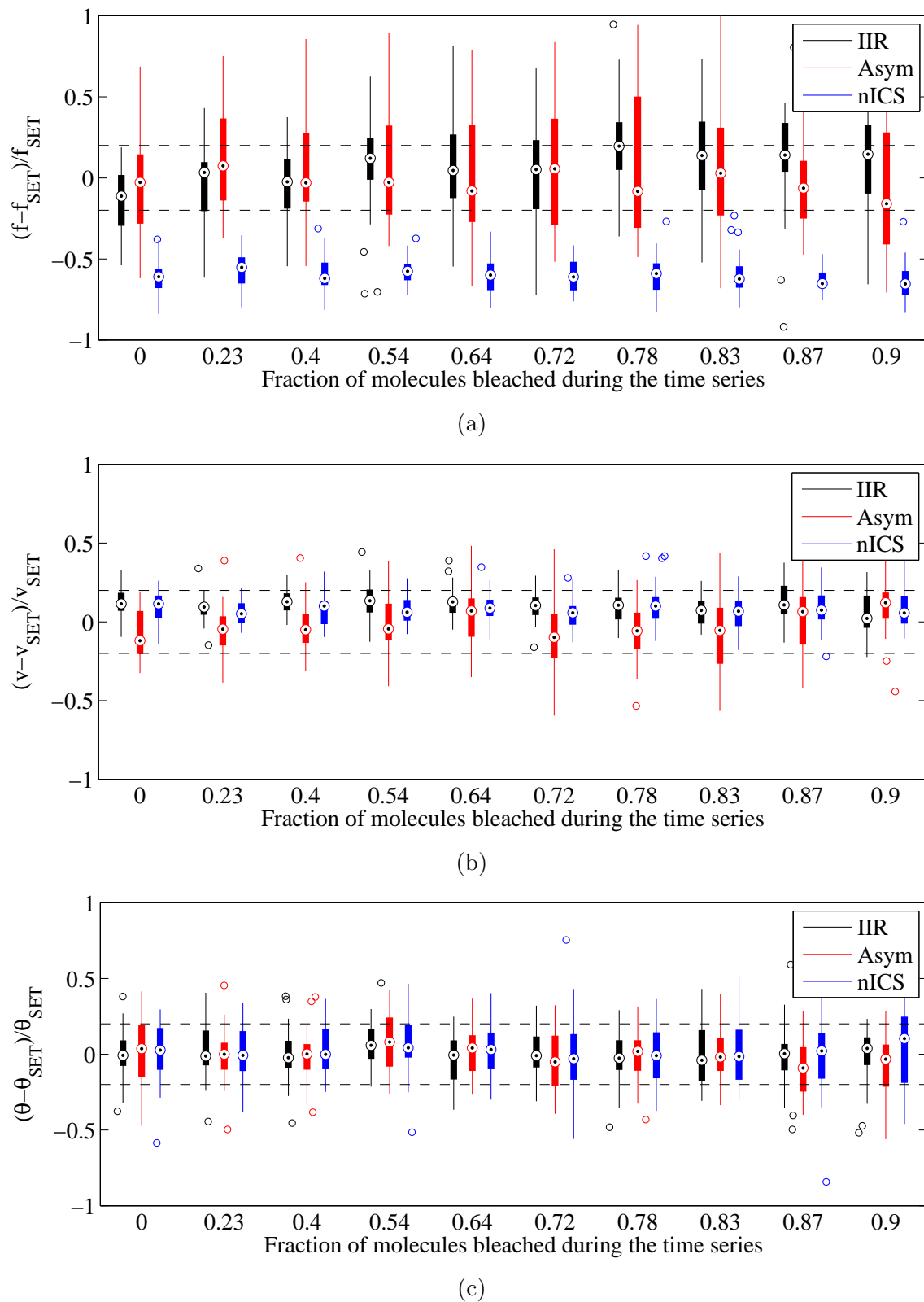


Figure 4.18: Accuracy and precision comparison of new techniques for measuring biased diffusion

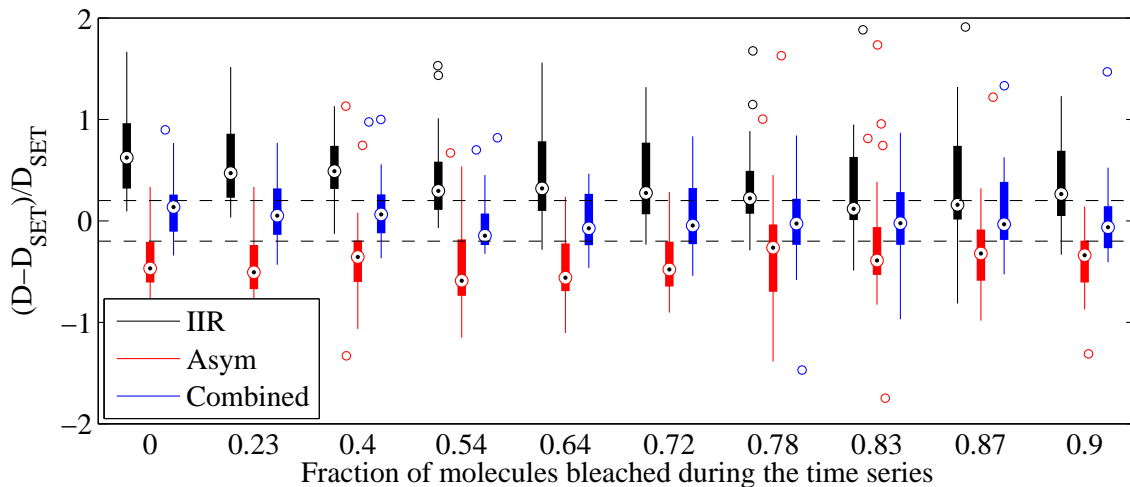


Figure 4.19: Accuracy and precision comparison of new techniques for measuring biased diffusion

and background population diffusion do limit more significantly the analysis for a biased diffusion than in the case of a pure flow. Therefore, biased diffusion emerges as the main limiting factor in extracting molecular transport with these methods. For this reason, we summarized the strengths and limitations of different techniques for measuring biased diffusion in table 4.2. Briefly, IIR filtering provides a generally good analysis, but the recovered velocity is biased due to deformation of the correlation function. The asymmetric analysis is often the most accurate, but generally exhibits low precision and is more sensitive to an immobile component and particularly a background diffusion. Finally, nICS is somewhere in between, with good precision but small bias for the velocity and strong bias for the recovered density. It is affected to a smaller degree by the density of the background components.

As for the diffusion coefficient, IIR and asymmetric analysis show equal but opposite bias with low precision. Hence, an unbiased diffusion coefficient fit depends on the convergence of the asymmetric analysis. We conclude this section by noting that we could extend the theory developed with nICS to account for biased diffusion. The results would probably be non-analytic, but we could still numerically fit the function and extract the diffusion coefficient. This would also probably remove the biases on

the extracted density and velocity.

		Density	Velocity	Diffusion
IIR	Accuracy	Good	Higher bias due to flow deformation	Higher bias
	Precision	Good	Good	Poor
	Limitations	Flow deformation, $B > 0.1$		Limited by asym. fit, $B \approx 0.1-10$
Asymmetry	Accuracy	Best	Best	Lower bias
	Precision	Fair	Fair	Poor
	Limitations	Mobile fraction density (10% for immo only, 30 % for immo. and diff.), $B > 0.2$		Same as for density and velocity, $B \approx 0.1-10$
nICS	Accuracy	Lower bias	Small higher bias	Not developed
	Precision	Best	Good	
	Limitations	Mobile fraction density (10 %), $B > 0.15$		

Table 4.2: Summary of strengths and limitations of IIR filtering, asymmetric analysis and nICS while analyzing biased diffusion.

4.8 Towards velocity distribution fitting

This chapter described the characterization *in silico* of the techniques we developed. We saw that, in certain limits, we could recover the velocity vector, along with two new parameters, the bias coefficient and the flow density. These parameters could not be extracted with previous correlation techniques. However, the ultimate goal would be to extract flow from multiple populations or from a distribution of velocities. We believe that the new techniques presented constitute a first step towards that goal. To demonstrate this, we simulated an exponential distribution of flow as shown in figure 4.20a. The total particle density was set to 20 particles/ μm^2 . We then analyzed this simulation with multiple cutoff frequencies between 1 and 10 mHz. Therefore,

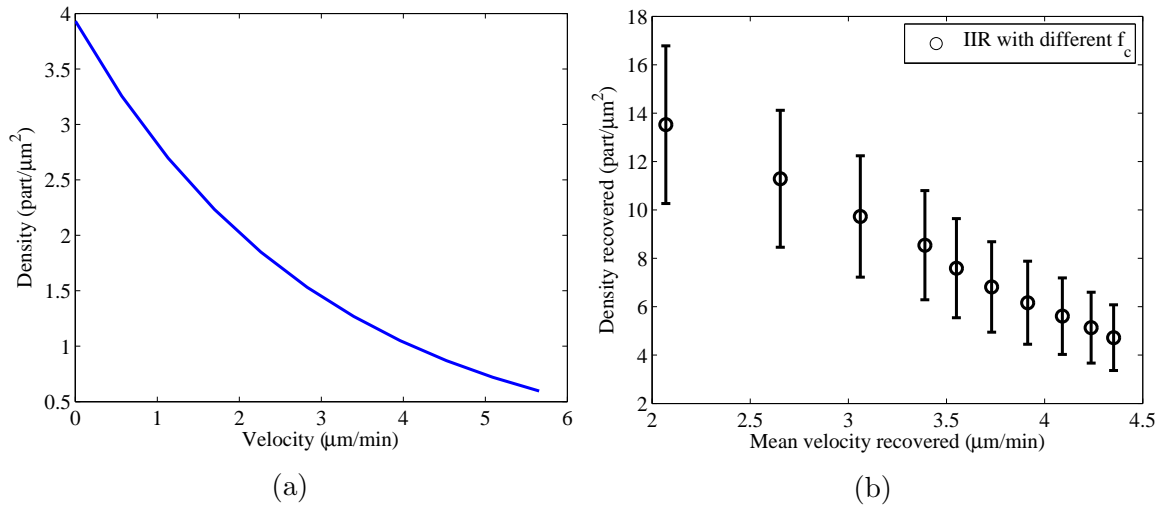


Figure 4.20: a) An exponential velocity-density distribution of $20 \text{ part}/\mu\text{m}^2$ total density was simulated. b) By varying the IIR filter from 1 and 10 mHz, different velocity-density couples were extracted. This curve could be use to extract information on the velocity distribution.

for each analysis, the distribution was filtered by a different part of the R velocity response curve (figure 4.2). This produced a different “apparent” average flow for each analysis. We plotted the results on a velocity-density graph, which shows the velocity recovered along with the density obtained with the IIR analysis, in figure 4.20b. This curve is characteristic of the flow distribution and could be used to build models of molecular transport (Gaussian distribution, exponential, etc.). Following this, the most likely models could be incorporated in the filterless analysis. This workflow could allow fitting of the distribution without *a priori* knowledge of the distribution.

Conclusion

IN this thesis, we have developed and characterized new tools that rely on the temporal frequency domain (ν -space) of the correlation function, or power spectrum, of images of fluorescently tagged molecules. These methods can provide new insights about the dynamics of proteins inside living cells and complement existing techniques.

In chapter 2, we developed a general formalism for spatio-temporal image correlation functions based on the theories of random signals and discrete-time signal processing. This allows easy extension of image correlation techniques to more complicated dynamics. We saw that different populations are summed in the correlation function, and that a dominant population can overshadow dynamics of a minority population. Furthermore, this knowledge allowed us to understand a bias in kICS, and provided the foundations for chapter 3.

Chapter 3 provided the theoretical basis for two new variations of image correlation spectroscopy, ν -space image correlation spectroscopy (nICS) and k - ν -space image correlation spectroscopy (knICS). The ν -space is an interesting domain to consider since it separates populations according to their dynamics. Immobile or slow dynamics are concentrated in the low frequencies, allowing extraction of smaller population with faster dynamics in the high frequencies. In nICS, the correlation function is complex and velocities can be extracted from the phase, similarly to kICS. However, there is no analytic form for diffusion and biased diffusion. In knICS, different populations are regrouped on different planes according to their dynamics. Finally, we developed two new methods of filtering. First, based on the expertise of discrete-time signal

processing, we devised a infinite-impulse response (IIR) frequency filter that is tunable to allow selection of specific dynamics. We also did a dimensionless analysis to see how filtering would affect our data. The second method enabling the extraction of flow is based on the fact that only the flow will provide an asymmetric contribution to the correlation function.

In chapter 4, we characterized all of these developments in numerical simulations. We benchmarked them under challenging conditions often found in real cellular data. We started by showing that the results for the previously developed Fourier immobile filter changed as the total window length varied, but our IIR did not. We also demonstrated the validity of the dimensionless analysis. We then compared nICS, the IIR filter and the asymmetric analysis for different densities of immobile particles, signal-to-noise ratio and concentration of background population. We found that the techniques were more limited by the bias coefficient than anything else, but allowed extraction of densities of flow, velocity vectors and bias coefficient over a wide range of conditions. The focus was on accuracy rather than precision since we simulated small region of analysis and multiples of those can be drawn inside a single cell.

In conclusion, we developed and characterized new techniques that complement the current toolbox of image correlation spectroscopy. Time frequency space methods are particularly useful when a dominant immobile population is present, as unfortunately is often the case in cells. They also allow extraction of a bias coefficient and flow density, two parameters that were previously inaccessible with image correlation techniques.

Finally, these techniques can be extended in many ways. Filtering could be extended in the k - ν space to select populations. Correlation function for different dynamics could be derived in nICS and more efficient fitting methods devised for knICS. Combining multiple techniques could allow reconstruction of a distribution of velocities if present. More importantly, it will be interesting to see what sort of insight about biological systems these tools will provide. We have shown that differences in

retrograde flow of adhesion proteins play a role in cell migration. Characterization of the flow density and bias coefficient could allow deeper understanding of these processes and of molecular transport and trafficking. We hope that the developments of this thesis will provide useful and accessible tools for biologists and biophysicists in the quest of understanding life at the molecular and cellular level.

BIBLIOGRAPHY

- [1] T. Dobzhansky. Nothing in biology makes sense except in the light of evolution. *American Biology Teacher*, 35(3):125–129, 1973.
- [2] G. Danuser and C.M. Waterman-Storer. Quantitative fluorescent speckle microscopy of cytoskeleton dynamics. *Annu. Rev. Biophys. Biomol. Struct.*, 35:361–387, 2006.
- [3] R.J. Petrie, A.D. Doyle, and K.M. Yamada. Random versus directionally persistent cell migration. *Nature Reviews Molecular Cell Biology*, 10(8):538–549, 2009.
- [4] M.S. Bretscher. On the shape of migrating cells a front-to-back model. *Journal of Cell Science*, 121(16):2625–2628, 2008.
- [5] C. Janetopoulos and R.A. Firtel. Directional sensing during chemotaxis. *FEBS letters*, 582(14):2075–2085, 2008.
- [6] P.J.M. Van Haastert and P.N. Devreotes. Chemotaxis: signalling the way forward. *Nature Reviews Molecular Cell Biology*, 5(8):626–634, 2004.
- [7] R. Horwitz and D. Webb. Cell migration. *Current Biology*, 13(19):30–40, 2003.
- [8] A.R. Horwitz and J.T. Parsons. Cell migration—movin’ on. *Science*, 286(5442):1102–1103, 1999.
- [9] A.J. Ridley, M.A. Schwartz, K. Burridge, R.A. Firtel, M.H. Ginsberg, G. Borisy, J.T. Parsons, and A.R. Horwitz. Cell migration: integrating signals from front to back. *Science*, 302(5651):1704–1709, 2003.
- [10] A.J. Ridley. Rho gtpases and actin dynamics in membrane protrusions and vesicle trafficking. *Trends in cell biology*, 16(10):522–529, 2006.
- [11] D.A. Lauffenburger and A.F. Horwitz. Cell migration: Review a physically integrated molecular process. *Cell*, 84:359–369, 1996.
- [12] M. Vicente-Manzanares, C.K. Choi, and A.R. Horwitz. Integrins in cell migration—the actin connection. *Journal of cell science*, 122(2):199–206, 2009.
- [13] W. Guo and Y. Wang. Retrograde fluxes of focal adhesion proteins in response to cell migration and mechanical signals. *Molecular biology of the cell*, 18(11):4519–4527, 2007.
- [14] C.M. Brown, B. Hebert, D.L. Kolin, J. Zareno, L. Whitmore, A.R. Horwitz, and P.W. Wiseman. Probing the integrin-actin linkage using high-resolution protein velocity mapping. *Journal of cell science*, 119(24):5204–5214, 2006.

- [15] K. Hu, L. Ji, K.T. Applegate, G. Danuser, and C.M. Waterman-Storer. Differential transmission of actin motion within focal adhesions. *Science's STKE*, 315(5808):111, 2007.
- [16] L. Chen, M. Vicente-Manzanares, L. Potvin-Trottier, P.W. Wiseman, and A. R. Horwitz. The integrin-ligand interaction regulates adhesion and migration through a molecular clutch. *PLoS ONE*, 7(7):e40202, 07 2012.
- [17] A. Einstein. Über die von der molekularkinetischen theorie der wärme geforderte bewegung von in ruhenden flüssigkeiten suspendierten teilchen. *Annalen der physik*, 322(8):549–560, 1905.
- [18] Joseph R. Lakowicz. *Principles of Fluorescence Spectroscopy*. Springer, 3rd edition, 2006.
- [19] G.G. Stokes. On the change of refrangibility of light. *Philosophical Transactions of the Royal Society of London*, 142:463–562, 1852.
- [20] X. Michalet, FF Pinaud, LA Bentolila, JM Tsay, S. Doose, JJ Li, G. Sundaresan, AM Wu, SS Gambhir, and S. Weiss. Quantum dots for live cells, in vivo imaging, and diagnostics. *Science*, 307(5709):538–544, 2005.
- [21] W.C.W. Chan and S. Nie. Quantum dot bioconjugates for ultrasensitive nonisotopic detection. *Science*, 281(5385):2016–2018, 1998.
- [22] A.I. Bachir, N. Durisic, B. Hebert, P. Grütter, and P.W. Wiseman. Characterization of blinking dynamics in quantum dot ensembles using image correlation spectroscopy. *Journal of applied physics*, 99:064503, 2006.
- [23] B.C. Lagerholm, G.E. Weinreb, K. Jacobson, and N.L. Thompson. Detecting microdomains in intact cell membranes. *Annu. Rev. Phys. Chem.*, 56:309–336, 2005.
- [24] U. Resch-Genger, M. Grabolle, S. Cavaliere-Jaricot, R. Nitschke, and T. Nann. Quantum dots versus organic dyes as fluorescent labels. *Nature Methods*, 5(9):763–775, 2008.
- [25] O. Shimomura, F.H. Johnson, and Y. Saiga. Extraction, purification and properties of aequorin, a bioluminescent protein from the luminous hydromedusan, aequorea. *Journal of cellular and comparative physiology*, 59(3):223–239, 1962.
- [26] R.Y. Tsien. The green fluorescent protein. *Annual review of biochemistry*, 67(1):509–544, 1998.
- [27] L. Bonetta. The inside scoop-evaluating gene delivery methods. *Nature Methods*, 2(11):875, 2005.
- [28] R. Heim, D.C. Prasher, and R.Y. Tsien. Wavelength mutations and posttranslational autoxidation of green fluorescent protein. *Proceedings of the National Academy of Sciences*, 91(26):12501, 1994.

- [29] R.E. Campbell, O. Tour, A.E. Palmer, P.A. Steinbach, G.S. Baird, D.A. Zacharias, and R.Y. Tsien. A monomeric red fluorescent protein. *Proceedings of the National Academy of Sciences*, 99(12):7877, 2002.
- [30] F.D. Urnov, J.C. Miller, Y.L. Lee, C.M. Beausejour, J.M. Rock, S. Augustus, A.C. Jamieson, M.H. Porteus, P.D. Gregory, and M.C. Holmes. Highly efficient endogenous human gene correction using designed zinc-finger nucleases. *Nature*, 435(7042):646–651, 2005.
- [31] M.H. Porteus and D. Carroll. Gene targeting using zinc finger nucleases. *Nature biotechnology*, 23(8):967–973, 2005.
- [32] B.A. Wilt, L.D. Burns, E.T.W. Ho, K.K. Ghosh, E.A. Mukamel, and M.J. Schnitzer. Advances in light microscopy for neuroscience. *Annual review of neuroscience*, 32:435, 2009.
- [33] N. Ji, H. Shroff, H. Zhong, and E. Betzig. Advances in the speed and resolution of light microscopy. *Current opinion in neurobiology*, 18(6):605–616, 2008.
- [34] D.J. Stephens and V.J. Allan. Light microscopy techniques for live cell imaging. *Science's STKE*, 300(5616):82, 2003.
- [35] M. Minsky. Microscopy apparatus, December 19 1961. US Patent 3,013,467.
- [36] W. Denk, J.H. Strickler, and W.W. Webb. Two-photon laser scanning fluorescence microscopy. *Science*, 248(4951):73–76, 1990.
- [37] W. Denk and K. Svoboda. Photon upmanship: Techreview why multiphoton imaging is more than a gimmick. *Neuron*, 18:351–357, 1997.
- [38] F. Helmchen and W. Denk. Deep tissue two-photon microscopy. *Nature methods*, 2(12):932–940, 2005.
- [39] EJ Ambrose. A surface contact microscope for the study of cell movements. *Nature*, 178:1194, 1956.
- [40] D. Axelrod. Cell-substrate contacts illuminated by total internal reflection fluorescence. *The Journal of cell biology*, 89(1):141–145, 1981.
- [41] P. Seitz and A.J.P. Theuwissen, editors. *Single-Photon Imaging*. Springer, 2011.
- [42] A.G. Godin. *Deciphering synaptic receptor distributions, clustering and stoichiometry using Spatial Intensity Distribution Analysis (SpIDA)*. PhD thesis, McGill University, 2010.
- [43] D. Magde, E.L. Elson, and W.W. Webb. Fluorescence correlation spectroscopy. ii. an experimental realization. *Biopolymers*, 13(1):29–61, 1974.
- [44] E. Haustein and P. Schwille. Fluorescence correlation spectroscopy: novel variations of an established technique. *Annu. Rev. Biophys. Biomol. Struct.*, 36:151–169, 2007.

- [45] T. Dertinger, V. Pacheco, I. von der Hocht, R. Hartmann, I. Gregor, and J. Enderlein. Two-focus fluorescence correlation spectroscopy: A new tool for accurate and absolute diffusion measurements. *ChemPhysChem*, 8(3):433–443, 2007.
- [46] E. Gielen, A. Benda, V. Fagulova, J. Vercammen, M. vandeVen, M. Hof, M. Ameloot, Y. Engelborghs, et al. Probing diffusion laws within cellular membranes by z-scan fluorescence correlation spectroscopy. *Biophysical journal*, 91(3):L23–L25, 2006.
- [47] Q. Ruan, M.A. Cheng, M. Levi, E. Gratton, and W.W. Mantulin. Spatial-temporal studies of membrane dynamics: scanning fluorescence correlation spectroscopy (sfcs). *Biophysical journal*, 87(2):1260–1267, 2004.
- [48] H. Qian, M.P. Sheetz, and E.L. Elson. Single particle tracking. analysis of diffusion and flow in two-dimensional systems. *Biophysical journal*, 60(4):910–921, 1991.
- [49] N.O. Petersen, P.L. Höddelius, PW Wiseman, O. Seger, and KE Magnusson. Quantitation of membrane receptor distributions by image correlation spectroscopy: concept and application. *Biophysical journal*, 65(3):1135–1146, 1993.
- [50] P.W. Wiseman and N.O. Petersen. Image correlation spectroscopy. ii. optimization for ultrasensitive detection of preexisting platelet-derived growth factor-[beta] receptor oligomers on intact cells. *Biophysical journal*, 76(2):963–977, 1999.
- [51] D.L. Kolin and P.W. Wiseman. Advances in image correlation spectroscopy: measuring number densities, aggregation states, and dynamics of fluorescently labeled macromolecules in cells. *Cell biochemistry and biophysics*, 49(3):141–164, 2007.
- [52] I.R. Bates, B. Hébert, Y. Luo, J. Liao, A.I. Bachir, D.L. Kolin, P.W. Wiseman, and J.W. Hanrahan. Membrane lateral diffusion and capture of cfr within transient confinement zones. *Biophysical journal*, 91(3):1046–1058, 2006.
- [53] P.W. Wiseman, C.M. Brown, D.J. Webb, B. Hebert, N.L. Johnson, J.A. Squier, M.H. Ellisman, and AF Horwitz. Spatial mapping of integrin interactions and dynamics during cell migration by image correlation microscopy. *Journal of cell science*, 117(23):5521–5534, 2004.
- [54] D.L. Kolin, S. Costantino, and P.W. Wiseman. Sampling effects, noise, and photobleaching in temporal image correlation spectroscopy. *Biophysical journal*, 90(2):628–639, 2006.
- [55] B. Hebert, S. Costantino, and P.W. Wiseman. Spatiotemporal image correlation spectroscopy (stics) theory, verification, and application to protein velocity mapping in living cho cells. *Biophysical journal*, 88(5):3601–3614, 2005.
- [56] M. Zhou and Y.L. Wang. Distinct pathways for the early recruitment of myosin ii and actin to the cytokinetic furrow. *Molecular biology of the cell*, 19(1):318–326, 2008.
- [57] J. Bove, B. Vaillancourt, J. Kroeger, P.K. Hepler, P.W. Wiseman, and A. Geitmann. Magnitude and direction of vesicle dynamics in growing pollen tubes using spatiotemporal image correlation spectroscopy and fluorescence recovery after photobleaching. *Plant physiology*, 147(4):1646–1658, 2008.

- [58] K. Tanner, D.R. Ferris, L. Lanzano, B. Mandefro, W.W. Mantulin, D.M. Gardiner, E.L. Rugg, and E. Gratton. Coherent movement of cell layers during wound healing by image correlation spectroscopy. *Biophysical journal*, 97(7):2098–2106, 2009.
- [59] C.M. Waterman-Storer and G. Danuser. New directions for fluorescent speckle microscopy. *Current biology*, 12(18):R633–R640, 2002.
- [60] A.V. Mikhailov and G.G. Gundersen. Centripetal transport of microtubules in motile cells. *Cell motility and the cytoskeleton*, 32(3):173–186, 1995.
- [61] C.M. Waterman-Storer, A. Desai, J. Chloe Bulinski, and ED Salmon. Fluorescent speckle microscopy, a method to visualize the dynamics of protein assemblies in living cells. *Current biology*, 8(22):1227–1230, 1998.
- [62] C.M. Waterman-Storer, J.W. Sanger, and J.M. Sanger. Dynamics of organelles in the mitotic spindles of living cells: membrane and microtubule interactions. *Cell motility and the cytoskeleton*, 26(1):19–39, 1993.
- [63] M.J. Lighthill. *Introduction to Fourier Analysis and Generalized Functions*. Cambridge University Press, 1958.
- [64] A.V. Oppenheim and R.W. Schaffer. *Discrete-time signal processing*. Pearson, 3rd edition, 2010.
- [65] H. Nyquist. Certain topics in telegraph transmission theory. *American Institute of Electrical Engineers, Transactions of the*, 47(2):617–644, 1928.
- [66] C.E. Shannon. Communication in the presence of noise. *Proceedings of the IRE*, 37(1):10–21, 1949.
- [67] J.W. Cooley, P.A.W. Lewis, and P.D. Welch. Historical notes on the fast fourier transform. *Proceedings of the IEEE*, 55(10):1675–1677, 1967.
- [68] M. Heideman, D. Johnson, and C. Burrus. Gauss and the history of the fast fourier transform. *ASSP Magazine, IEEE*, 1(4):14–21, 1984.
- [69] F.J. Harris. On the use of windows for harmonic analysis with the discrete fourier transform. *Proceedings of the IEEE*, 66(1):51–83, 1978.
- [70] G.M. Jenkins and D.G. Watts. *Spectral analysis and its applications*. San Francisco: Holden-Day, 1969.
- [71] M.S. Bartlett. *An Introduction to Stochastic Processes with Special Reference to Methods and Applications*. Cambridge University Press, 1953.
- [72] P. Welch. The use of fast fourier transform for the estimation of power spectra: a method based on time averaging over short, modified periodograms. *Audio and Electroacoustics, IEEE Transactions on*, 15(2):70–73, 1967.

-
- [73] D.L. Kolin, D. Ronis, and P.W. Wiseman. k-space image correlation spectroscopy: a method for accurate transport measurements independent of fluorophore photophysics. *Biophysical journal*, 91(8):3061–3075, 2006.
- [74] David L. Kolin. *k-Space Image Correlation Spectroscopy: Theory, Verification and Applications*. PhD thesis, McGill University, 2008.
- [75] Jeremy A. Schwartzentruher. k-space image correlation spectroscopy (kics): Accuracy and precision, capabilities and limitations. Master’s thesis, McGill University, 2010.
- [76] R.B. Dalal, M.A. Digman, A.F. Horwitz, V. Vetri, and E. Gratton. Determination of particle number and brightness using a laser scanning confocal microscope operating in the analog mode. *Microscopy research and technique*, 71(1):69–81, 2008.
- [77] M.A. Digman, C.M. Brown, A.R. Horwitz, W.W. Mantulin, and E. Gratton. Paxillin dynamics measured during adhesion assembly and disassembly by correlation spectroscopy. *Biophysical journal*, 94(7):2819–2831, 2008.
- [78] S. Butterworth. On the theory of filter amplifiers. *Wireless Engineer*, 7:536–541, 1930.
- [79] Benedict Hebert. *Spatio-Temporal Image Correlation Spectroscopy: Development and Implementation in Living Cells*. PhD thesis, McGill University, 2006.
- [80] S. Costantino, J.W.D. Comeau, D.L. Kolin, and P.W. Wiseman. Accuracy and dynamic range of spatial image correlation and cross-correlation spectroscopy. *Biophysical journal*, 89(2):1251–1260, 2005.
- [81] R. McGill, J.W. Tukey, and W.A. Larsen. Variations of box plots. *American Statistician*, pages 12–16, 1978.

A

BIOHAZARDOUS MATERIALS CERTIFICATE
